SANDIA REPORT

SAND2016-0167
Unlimited Release
Printed January 2016

Permafrost Active Layer Seismic Interferometry Experiment (PALSIE)

Robert E. Abbott
Hunter A. Knox
Stephanie James
Rebekah Lee
Chris Cole

Prepared by
Sandia National Laboratories
Albuquerque, New Mexico 87185 and Livermore, California 94550

Sandia National Laboratories is a multi-program laboratory managed and operated by Sandia Corporation, a wholly owned subsidiary of Lockheed Martin Corporation, for the U.S. Department of Energy's National Nuclear Security Administration under contract DE-AC04-94AL85000.

Issued by Sandia National Laboratories, operated for the United States Department of Energy by Sandia Corporation.

Available to DOE and DOE contractors from
U.S. Department of Energy
Office of Scientific and Technical Information
P.O. Box 62
Oak Ridge, TN 37831

Telephone: (865) 576-8401
Facsimile: (865) 576-5728
E-Mail: reports@osti.gov
Online ordering: http://www.osti.gov/scitech

Available to the public from
U.S. Department of Commerce
National Technical Information Service
5301 Shawnee Rd
Alexandria, VA 22312

Telephone: (800) 553-6847
Facsimile: (703) 605-6900
E-Mail: orders@ntis.gov
Online order: http://www.ntis.gov/search

SAND2016-0167
Unlimited Release
Printed January 2016

Permafrost Active Layer Seismic Interferometry Experiment (PALSIE)

Robert Abbott[1], Hunter Knox[1], Stephanie James[2], Rebekah Lee[3], and Chris Cole[4]
1: Geophysics and Atmospheric Sciences
Sandia National Laboratories
P.O. Box 5800
Albuquerque, New Mexico 87185-MS0750
2:Now at The University of Florida, Gainesville, FL
3: Now at Boise State University, Boise, ID
4: Bureau of Land Management, Lakewood, CO

Abstract

We present findings from a novel field experiment conducted at Poker Flat Research Range in Fairbanks, Alaska that was designed to monitor changes in active layer thickness in real time. Results are derived primarily from seismic data streaming from seven Nanometric Trillium Posthole seismometers directly buried in the upper section of the permafrost. The data were evaluated using two analysis methods: Horizontal to Vertical Spectral Ratio (HVSR) and ambient noise seismic interferometry. Results from the HVSR conclusively illustrated the method's effectiveness at determining the active layer's thickness with a single station. Investigations with the multi-station method (ambient noise seismic interferometry) are continuing at the University of Florida and have not yet conclusively determined active layer thickness changes. Further work continues with the Bureau of Land Management (BLM) to determine if the ground based measurements can constrain satellite imagery, which provide measurements on a much larger spatial scale.

ACKNOWLEDGMENTS

This work would not have been possible without assistance from the University of Alaska Fairbanks and Poker Flat Research Range personnel. We would like to thank all of the PFRR staff with a special thanks to Kathe Rich, Bob Valdez, and Kevin Abnett. We appreciate all of your efforts to keep the array alive and functioning.

This work was also greatly aided by the Incorporated Research Institutions for Seismology (IRIS) PASSCAL Instrument Center (PIC) staff. IRIS PIC staff along with the Darrin Hart provided guidance in building the instrumentation housing so that the equipment would operate year round. The PIC staff provided equipment, field support, and data archival for the Refraction Microtremor (ReMi) survey described here. IRIS also supported a summer intern, Rebekah Lee, who worked diligently on the Horizontal to Vertical Spectral Ratio (HVSR) measurements and travelled to Alaska to conduct the ReMi survey. The difficult ReMi data processing and interpretation was greatly aided by Aasha Pancha, who performed analysis in real time while the data were collected in July of 2014.

Jose Pina and Francisco Sanchez-Sesma of the National Autonomous University of Mexico constructed inversion results from the HVSR data, which are presented here. Their expert opinions and valuable input greatly helped in understanding the HVSR measurements and their seasonal trends. We would like to thank Thomas Lecocq of the Royal Observatory of Belgium and Florent Brenguier of Institut des Sciences de la Terra who provided valuable support for the multi-station method through a short course taught at the AGU Fall Meeting 2014 and continued correspondence.

We would also like to thank the Bureau of Land Management (BLM) and the United States Geologic Survey (USGS) for providing support to link the ground based measurements to satellite observations. Finally, we would like to thank Olson Engineering and Shannon & Wilson who installed boreholes and conducted a detailed crosshole seismic survey, which is presented here, that helped verify the results derived from the passive seismic measurements.

CONTENTS

FIGURES

TABLES

NOMENCLATURE

PFRR	Poker Flat Research Range
DOE	Department of Energy
SNL	Sandia National Laboratories
HVSR	Horizontal to Vertical Spectral Ratio
ReMi	Refraction Microtremor
IRIS	Incorporated Institutes for Seismology
PIC	PASSCAL Instrument Center
BLM	Bureau of Land Management
USGS	United States Geologic Survey
SNR	Signal to Noise Ratio
PoE	Power over Ethernet
TOC	Top of Casing

1. INTRODUCTION

Comment [HK]: Odd page required

The Arctic is important to Earth's climate system (Assessment, 2004). In September 2012, Arctic sea ice retreated the furthest in recorded history, opening the Arctic to commerce, resource exploration, and national security threats (National Snow and Ice Data Center, 2015). The melting of Arctic ice also increases sea-surface temperatures, which may lead to increased storm severity around the globe [Evans, 1993]. The melting of permafrost releases methane, which has been locked in the frozen layers, potentially causing further increases in Earth's temperature. Microbial action on previously frozen carbon (in the form of roots, plant matter, animal carcasses, etc.) in the permafrost releases CO_2 into the air. This creates another positive feedback loop as increased melting leads to increased greenhouse gasses which leads to increased temperatures, which in turn leads to increased melting.

Clearly, the health of the permafrost system is of great importance, given its behavior. Current climate models do not have sufficient data to accurately predict the impact permafrost degradation will have on climate. One of the key observables in the permafrost system is the thickness of the so-called "active layer". The active layer is shallowest layer of soil and rock. This layer freezes and thaws annually with the seasons. At higher latitude stations, the thickness is less than at lower latitude stations. This is largely due to the amount of solar radiation at those latitudes. Another factor, however, is the time history of temperatures experienced at the site. Determining remotely the thickness of this active layer is the goal of this research project.

There are a few methods of determining active layer thickness in common use. The most widely used of these is the physical probe (tile probe). In this technique, a sharp metal probe is inserted into the Earth until it bottoms out at a frozen layer. This distance is noted and further measurements are made in a grid-like pattern. These measurements are then taken again and different times of the year, so that temporal evolution of the thawing or freezing is captured. These measurements are often supplemented by another common technique: borehole temperature measurements, or, alternatively, frost tubes (Iwata, et al., 2011).

The existing ways of measuring active layer thickness have some drawbacks. The physical probing measurements and frost tubes require expensive and time consuming site visits. This is expense is exacerbated for remote areas. These methods (including borehole temperature measurements) are also point measurements. Since active-layer thickness can vary dramatically over a small area, multiple distributed measurements are required to create an average layer thickness in the study area. In the case of physical probing, this can be accomplished readily enough, but it is not practical to have dozens of boreholes or tubes.

Ideally, active layer measurements would have the following characteristics: 1) Able to be conducted remotely; 2) Able to be conducted continuously, in real-time; and 3) Able to sample wide areas, rather than individual point locations. This report details the investigation of one such potential technique. Namely, using ambient seismic noise recorded on seismometers buried in the shallow subsurface.

2. ARRAY SITING

Measuring changes in permafrost required that an appropriate site location be chosen and a ruggedized autonomous seismic network be designed. Constraints on the site location, as discussed below, were primarily logistical in nature, whereas the requirements for continuous monitoring in the harsh Arctic environment were mostly concentrated on array engineering, which is discussed in Section 4. Array Design and Installation. This type of continuous monitoring, especially in a remote polar environment, necessitates even more considerations than one deployed locally in a relatively temperate environment.

1. The primary goal for the project was to measure permafrost changes with a remote seismic network, meaning that the array had to be physically sited on permafrost. Since a United States deployment was desired for logistical reasons, this limited our choice of locations to the state of Alaska.
2. Within the state of Alaska, permafrost conditions (thickness, continuity, active layer thickness, etc.) vary greatly (See Figure 1) and special consideration had to be taken in site selection. Because this pilot study was designed to test whether ambient noise seismic methods could resolve the active layer and its associated changes, we desired a location with a significant active-layer thickness. Active layer thickness is generally correlated with insolation. Therefore, far northern sites, like the Atmospheric Radiation Measuring (ARM) Site at Barrow, were expected to have thinner maximum active layer thicknesses than a site at a more southern latitude, and thus eliminated.
3. The project goals required several trips each year to the site/array for station maintenance and ground truth surveys and therefore restricted site locations to those with easy access. This meant that the site needed to be on a maintained road accessible by car during the late spring to early fall months.
4. We desired a location where communications (i.e. data transfer to SNL) were available at a reasonably low cost. For much of the state, cell phone access for telemetering the data is non-existent, leaving satellite communications as the only method for real-time telemetry. For our bandwidth (7 stations at 250 samples a second), satellite telemetry was deemed to be too

expensive. We, therefore, were restricted to a site that had an established Internet connection or cellphone access.

5. We required a secure site, meaning that the stations would be inaccessible to the general public. This constraint on site location was important to avoid issues of vandalism and theft.
6. We desired a site that had access to local labor for simple array maintenance. Although at least two trips to the array from Albuquerque per year were assumed, local help was desired for small tasks that ideally would not require expensive mobilization.

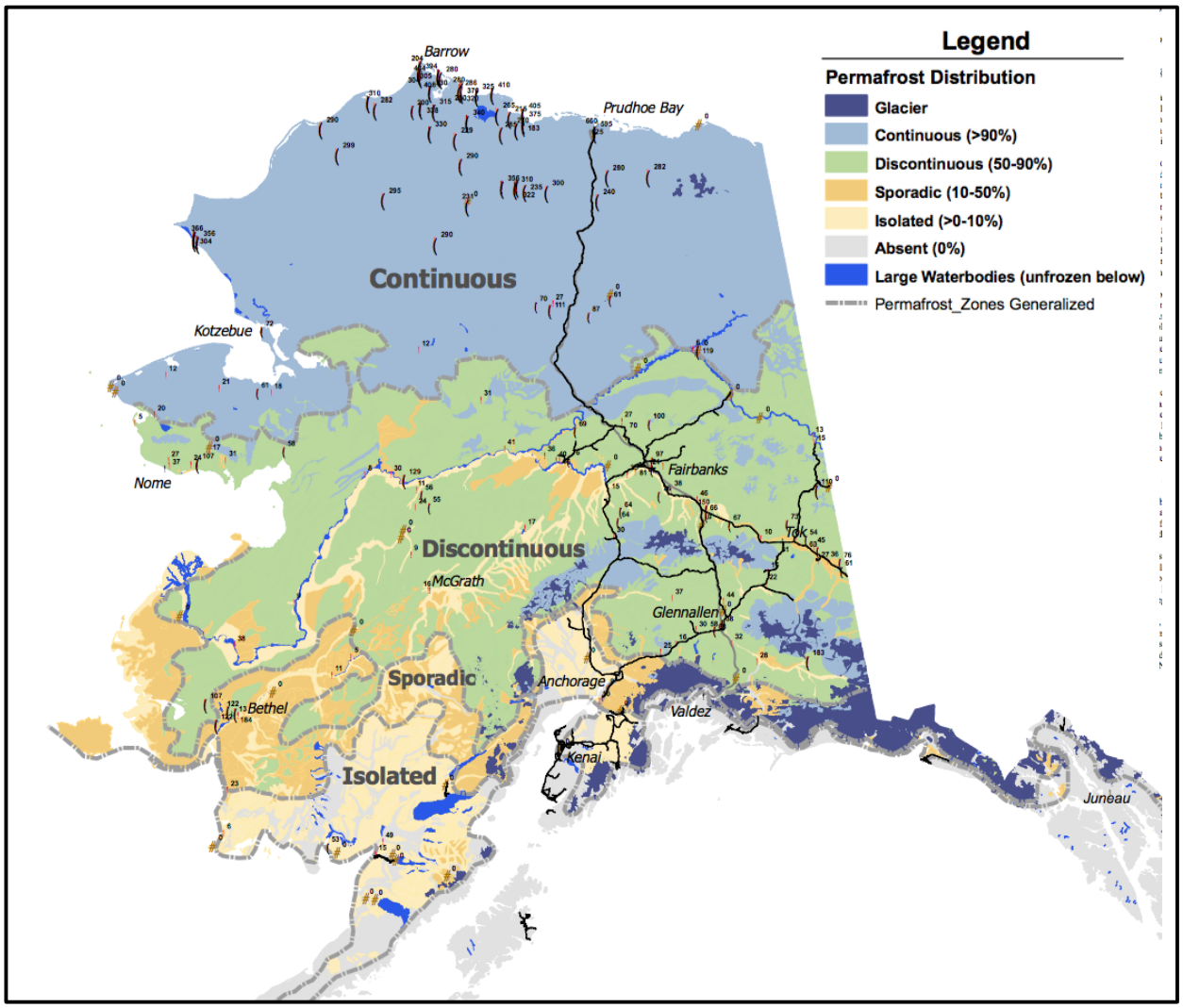

Figure 1: From Yoshikawa et al. (2008) this map illustrates the spatial variability in permafrost distribution for the state of Alaska. These general trends were considered when selecting an appropriate site for this study. Specifically the team desired a location that was either classified as discontinuous or continuous permafrost.

Balancing these constraints, we decided to deploy at the Poker Flat Research Range (PFRR), near Fairbanks, Alaska. The site, which is located in central Alaska (See Figure 2), was known to have a moderate active-layer thickness (~ 30 cm to 1 m) and discontinuous permafrost (Personal Comm. with PFFR Personnel). The site is accessible by a short drive from Fairbanks and is controlled by the University of Alaska, Fairbanks (UAF).

Figure 2: Map of Alaska showing the study site's location in relation to major landmarks in Alaska.

The benefits of UAF control were three-fold. Firstly, year-round onsite personnel, with technical backgrounds, are stationed there to help with array maintenance. Secondly, the site is in a controlled area where vandalism and theft were not a concern. Thirdly, and perhaps most importantly, communication and power for the array were provided by PFRR. These details will be discussed in the next section.

3. POKER FLAT RESEARCH RANGE (PFRR)

3.1 Site Description

The site location for this study was contained within a ~0.01 km^2 area at Poker Flat Research Range (PFRR), approximately 30 miles north of Fairbanks, Alaska (See Figure 2). PFRR is a scientific research facility owned and operated by the Geophysical Institute of the University of Alaska. PFRR lies within the northern portion of what is known as the Fairbanks mining district of Alaska. This mining district was one of the most important gold producing areas in Alaska (Robinson et al., 1990). The site is situated along the northwest side of a slope that descends gradually to the Chatanika River located approximately 1 km to the northwest from the site. Permafrost in the study region is discontinuous, meaning permafrost is typically no more than 50 m thick and talik zones are common (Schuur et al., 2008; Yershov, 1998) (See Figure 1). The study area is within the boreal forest ecoregion of interior Alaska as classified by Nowacki and others (2001). More specifically, PFRR lies in the Yukon-Tanana Uplands of the Intermontane Boreal ecoregion (Nowacki et al., 2001) (See Figure 3).

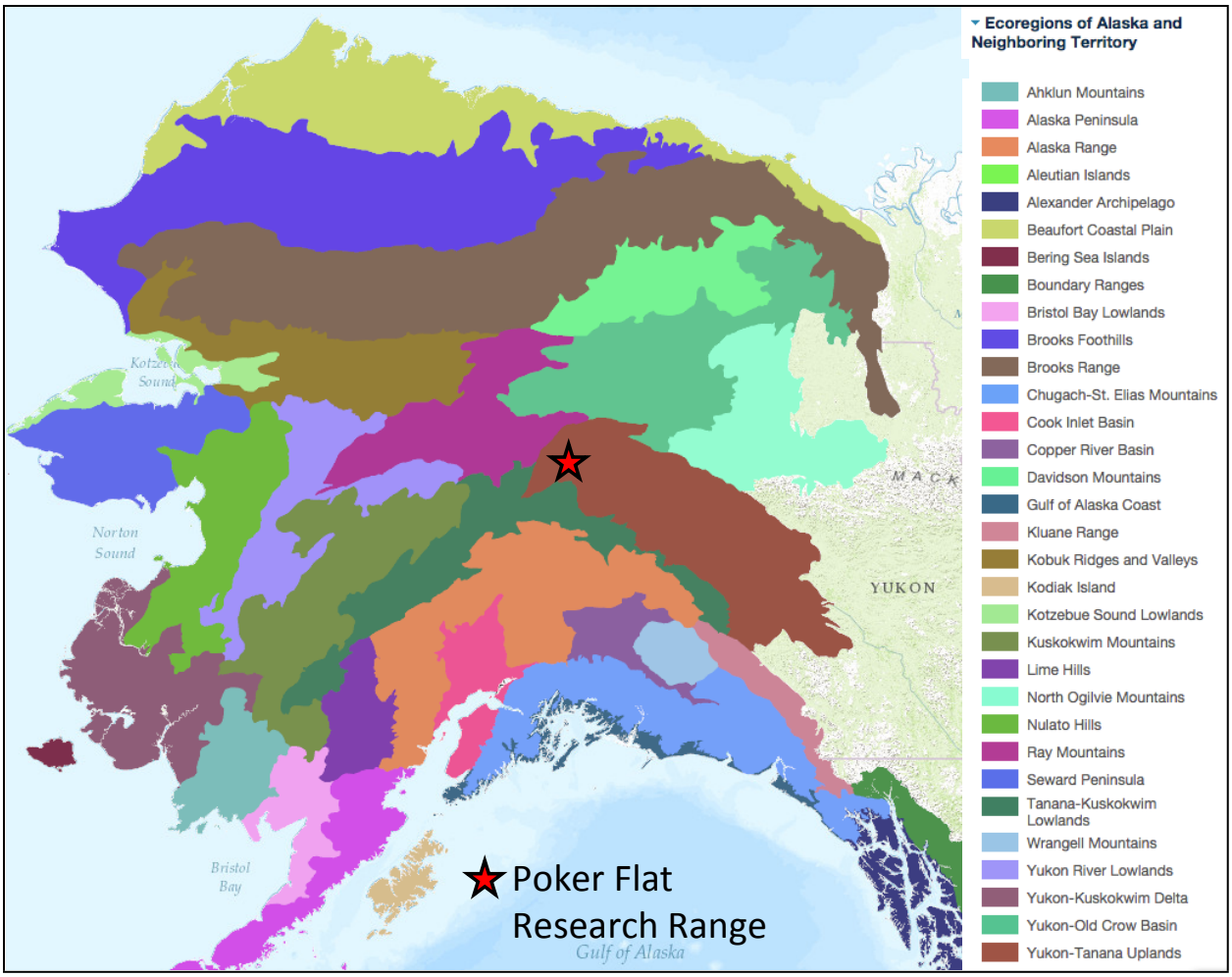

Figure 3: Map showing site location (red star) and ecoregion classification for Alaska.

A suite of factors such as topography, vegetation, snow, and soil properties mediates the presence of permafrost in interior Alaska. For example, in the discontinuous permafrost zone that comprises our study site, permafrost generally occurs on north-facing slopes since they receive less direct radiation compared to south-facing slopes (Jorgenson et al., 2010). Also, the boreal forests of the study region can have an insulating effect on the soil, thereby contributing to factors controlling permafrost (Jorgenson et al., 2010). In turn, the presence and type of vegetation can be influenced by permafrost characteristics, and can sometimes be used as permafrost and active layer thickness/presence indicators. For example, the northwest portion of the site contains black spruce trees, which generally occur in poorly drained organic soils that are underlain by permafrost (Dyrness et al., 1992). We would expect that active layer thicknesses

and permafrost extents in the northwest portion are different than those in locations without black spruce trees on the study site.

A satellite image of the seismic array, with 5 of the 7 stations visible, is shown in Figure 4. The northwest-most station is not visible as it lies within the black spruce forest. The approximate location of the cross-well seismic survey is depicted with an orange circle.

Figure 4: Satellite image of the seven sensor seismic array, five of which are visible as white dots. The orange circle indicates the approximate location of the cross-well seismic survey conducted in June 2015.

3.2 Geologic Background

Yukon-Tanana Terrane (YTT), an assemblage of Upper Paleozoic and older metasedimentary, metavolcanic, and metaplutonic rocks, underlies the study region. YTT is one of the largest terranes that comprise the northern cordillera and lies between in-place and displaced strata of the North American continental margin (Mortensen, 1992; Newberry et al., 1996). The basal rock type of the research area is Mid- to Late Paleozoic quartzite, schistose quartzite, and quartz-mica schist of the Yukon-Tanana Upland assemblage (Wilson et al., 1998). Overlying the quartz-mica schist are rocks of similar lithologic properties that contain thin interlayers of eclogite-bearing schist. These rocks occur at depths of approximately 20-40 m in the study area (Olson Engineering Crosshole Seismic Report; "Chatanika River Mine").

Valleys and rounded ridges characterize the study region. Unconsolidated alluvial deposits of sand, silt, and gravel fill the lowlands and valley bottoms. These undifferentiated Quaternary deposits overlie the basement metamorphic rocks. Eolian loess (windblown silt) lay on the hilltops and upper-to-mid slopes of the ridges. Along the lower hillsides, loess has been reworked by slope processes and mixed with organic matter and silt of the valley bottoms (Robinson et al., 1990; Newberry et al., 1996). These mixtures of silt, peat, and organic matter are the most surficial deposits in the study area. Figure 5 shows a geologic map of the Fairbanks Mining District and the local geology of PFRR. The specific geologic unit descriptions of the PFRR area are included in Figure 5.

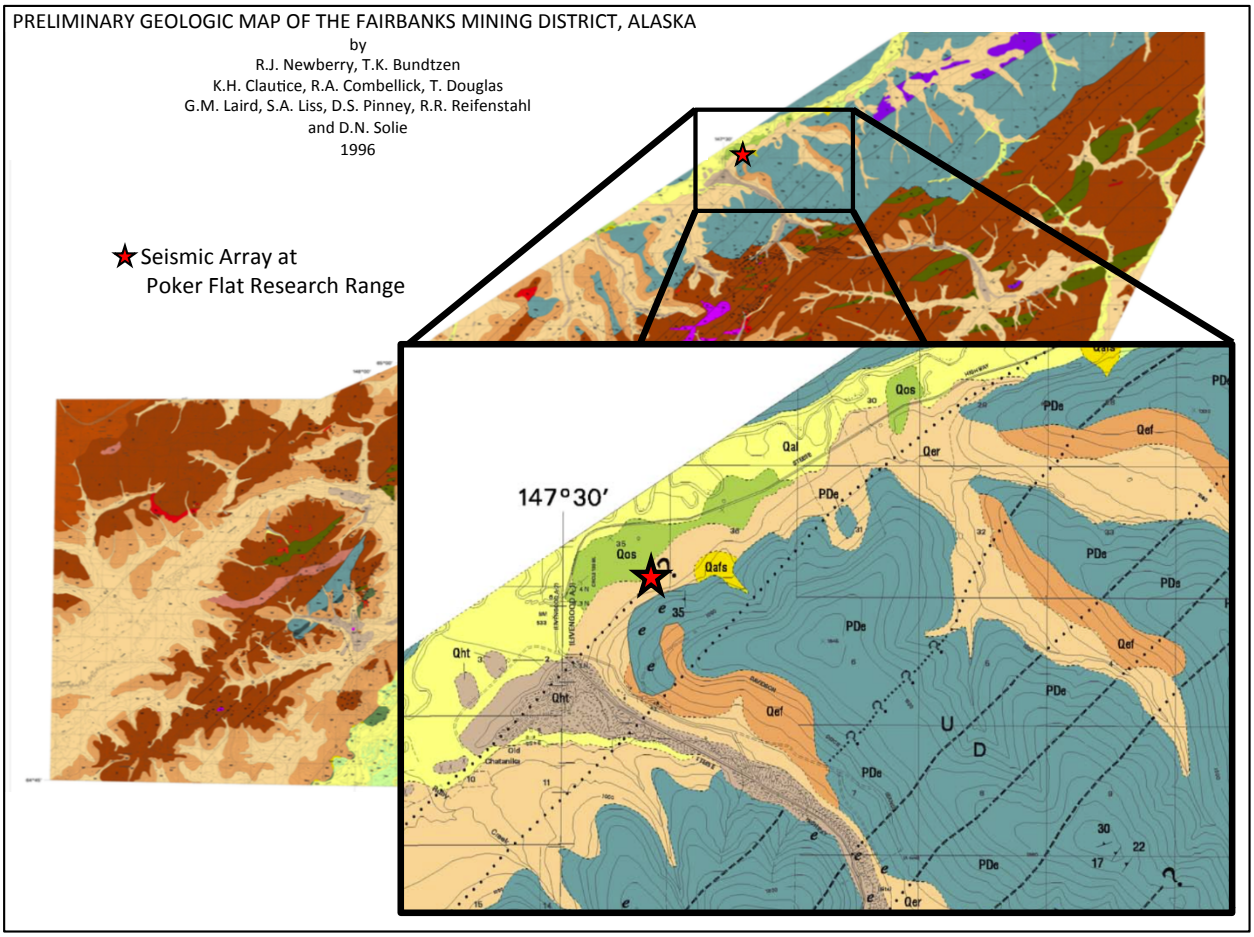

Figure 5: Geologic map of the Fairbanks Mining District. Scale 1:63,360. Inset shows the local geology at PFRR. In this image the red star shows the approximate location of the seismic array within PFRR. From the surface moving stratigraphically downwards the geologic units of the immediate area surrounding PFRR are as follows: Qal, flood-plain alluvium consisting of unconsolidated silt, sand, and gravel; Qht, reworked Placer-mine dredge tailings from the Old Chatanika mine activities; Qafs, alluvial-fan deposits composed largely of silt overlying flood-plain alluvium; Qef, Fairbanks Loess; Qer, eolian silt retransported from hills to lower slopes and valley bottoms; Qos, organic-rich silt deposits of lowland bogs; Pde, eclogite bearing schist amphibolite, and quartzite (Newberry et al, 1996). The dashed lines indicate inferred locations of faults, dotted where questionable.

Soil/rock cuttings from drilling adjacent to the seismic array revealed schist bedrock at a depth of ~21 meters overlain by unconsolidated sand, gravel and silt (Table 1). The upper meter contains predominantly silt and organic matter. Drilling was done during the summer (June 2015) and found the top 0.3 m to be thawed. Ice was reported from 0.3 m to the full extent drilled (~21 m). No groundwater was observed during the placement of the two boreholes (Olson Engineering Crosshole Seismic Report).

Table 1: Stratigraphy of study area within Poker Flat Research Range from Olson Engineering Crosshole Seismic Report.

Top Depth (Meters below ground surface)	Lithology
0.0	Peat and organic silt
0.9	Silt and sandy silt
1.8	Sand and gravelly sand
3.3	Gravelly sand, sandy gravel, occasional cobbles
21.3	Schist bedrock. Very weathered at top of unit, decreasing degree of weathering with depth.

4. ARRAY DESIGN AND INSTALLATION

4.1 Array Engineering

Below we will discuss the specific challenges and engineering considerations for continuous monitoring in the permafrost as specified in the LDRD goals. We note here that while this short list covers the challenges in our specific situation, each Arctic site location requires a thorough evaluation of power, communications, temperature extremes, etc.

- Polar regions receive little to no sunlight in the winter months and can experience twenty-four hours of sunlight in the summer months. Many remote seismic installations rely on solar panels to recharge a suite of batteries that provide power to the station. This configuration is not desirable in high latitude deployments unless an alternative source of energy is available for the winter months. Recent deployments in the Arctic and Antarctica often utilize dozens of deep-cycle batteries, a few very expensive lithium ion batteries, and/or wind turbines to sustain them through the winter. Choosing appropriate equipment for power becomes challenging because Polar Regions are very cold and most equipment is not designed to operate in such low temperatures. For reference, low temperatures in the winter months at PFRR average -17 degrees Celsius, with record temperatures being as low as -50 degrees Celsius
- We had to ensure that our equipment was resistant to animals chewing on cables, knocking over antennas, stomping on cables, etc.
- Alaska generally has extensive snow cover in the winter months. Therefore we had to design systems that could survive being buried in multiple feet of snow. Furthermore, during spring snowmelt, water would likely inundate the array. Therefore, the systems also had to be waterproof.
- The active layer of permafrost is structurally unstable. Every time the active layer thaws or freezes, any instrument deployed therein will likely shift slightly. For most sensitive seismometers, which require meticulous leveling, this would be a definite contaminating influence on the data. This required that we consider sensors that could either self-level or could tolerate a larger amount of tilt.

- For the project to be successful, we needed to record high frequency (i.e. above 20 Hz) ambient noise with reliable fidelity. These signals are known to have very small amplitudes, thus requiring very quiet and sensitive instruments.

4.2 Array Equipment

Considering the hazards discussed above and the requirements for project success, the team designed a seismic network with the following components.

4.2.1 Seismometers:

We chose to purchase seven Nanometrics Trillium Compact (TC) Posthole sensors (see Figure 6). These state-of-the-art sensors were chosen because of several attractive characteristics. First, the instruments had self-noise levels below the USGS New Low-Noise Minimum Model (NLNM) at the frequencies of interests (> 1 Hz). The NLNM is calculated from the quietest sites in the World-Wide Seismograph Network. This characteristic helped ensure that we could record ambient noise at the PFRR site above instrument noise levels. Secondly, the TC sensor, which is in a waterproof case, is designed for direct burial, meaning it does not require a seismic vault or enclosure. Lastly, the TC sensor has wide tilt tolerance (+/- 10 degrees from horizontal). Therefore, the instrument is capable of high fidelity measurements as long as the tilt tolerance is not exceeded. This characteristic is particularly important because the instrument was expected to tilt slightly with each active layer freeze/thaw cycle.

Figure 6: Nanometrics Trillium Compact (TC) Posthole sensor

4.2.2 Digitizers:

Refraction Technologies (RefTek) Model 130 6-channel digitizers (see Figure 7) were chosen for the digital acquisition systems (DAS). We chose this DAS because of our familiarity with the system (SNL maintains a significant number of them) and also their successful use in other Arctic and Antarctic deployments (Tim Parker, per. comm.)

Figure 7: Refraction Technologies (RefTek) Model 130 6-channel digitizer.

4.2.3 Power System:

After evaluating all of the possible power options, we decided to power the system from the Balloon Inflation building at PFRR, which is approximately 100 meters from the center of the array. From the building, we wired the 120 V AC power to the center of the array, where we placed a Power-Over-Ethernet (PoE) hub. The PoE distributed 40 Volts DC to the seven array elements. There the 40 Volts were reduced to 12 Volts by a DC-to-DC power converter (See Figure 8).

4.2.4 Communications:

The array's close proximity to a building with power and Internet allowed us to install a physical Ethernet cable for communication. The Internet cable from the building was plugged into the PoE and distributed to the seven stations. Inside the building, data was stored on an external hard drive attached to a laptop computer running RefTek's communication software RTPD.

4.2.5 Cold Protection:

The buried TC seismometers did not require additional protection from the cold because the ground is a sufficient insulator from potential cold air temperatures. The DAS, PoE, power converters etc, did require protection, however. For instrument enclosures, we retrofitted Pelican Stormcase waterproof cases with insulting pink fiberboard. Inside the cases, we installed small

sections of resistive heating mats similar to those used in residential radiant heat floors. We split the DC power (delivered by the PoE) between the digitizer and a thermostat to regulate the radiant heating mat. The thermostat was set to turn on for temperatures below approximately zero degrees Celsius (See Figure 8).

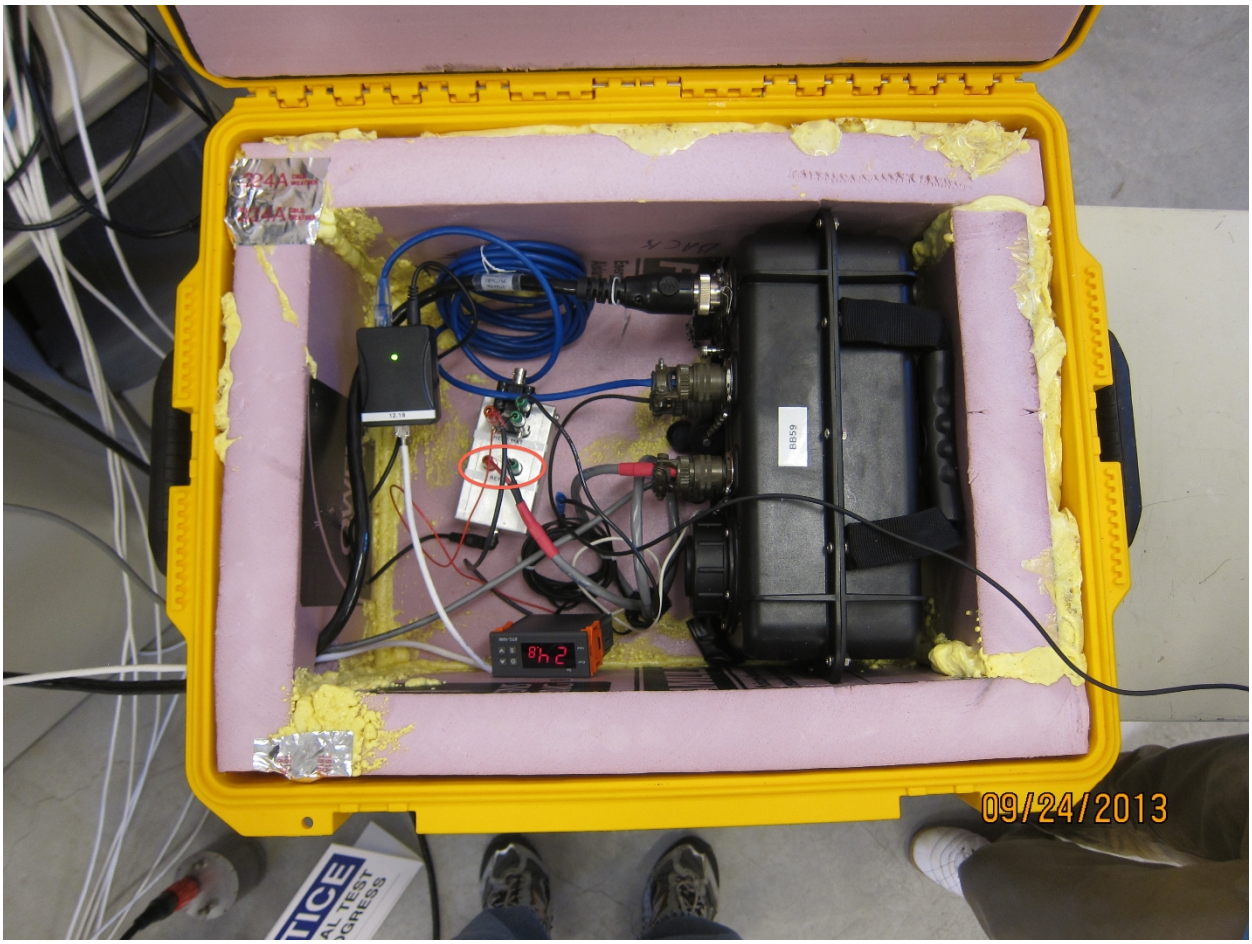

Figure 8: Instrumentation case filled with all equipment during a huddle test. The large black box on the left is the RefTek Rt130; the grey box in the center on the lower wall (displaying 24.8) is the temperature control unit; the heating pad can be seen fixed to the wall on the left; the power over Ethernet connection is in the upper left corner (black box with green light); and finally the DC to DC power converter is the silver bow in the center.

4.2.6 Heat Protection:

Testing showed that the PoE instrumentation inside the central element box generated substantial heat. In fact, it generated enough heat during the winter that the heating mat was never required. Unfortunately, this meant that in the summer, the box approached 50 degrees Celsius regularly. This is the upper temperature limit for operating the equipment therein. Upon

discovery of this fact, we retrofitted the central station with a fan and snorkel system that drew fresh air through the box, while keeping the insects and rain out (See Figure 9).

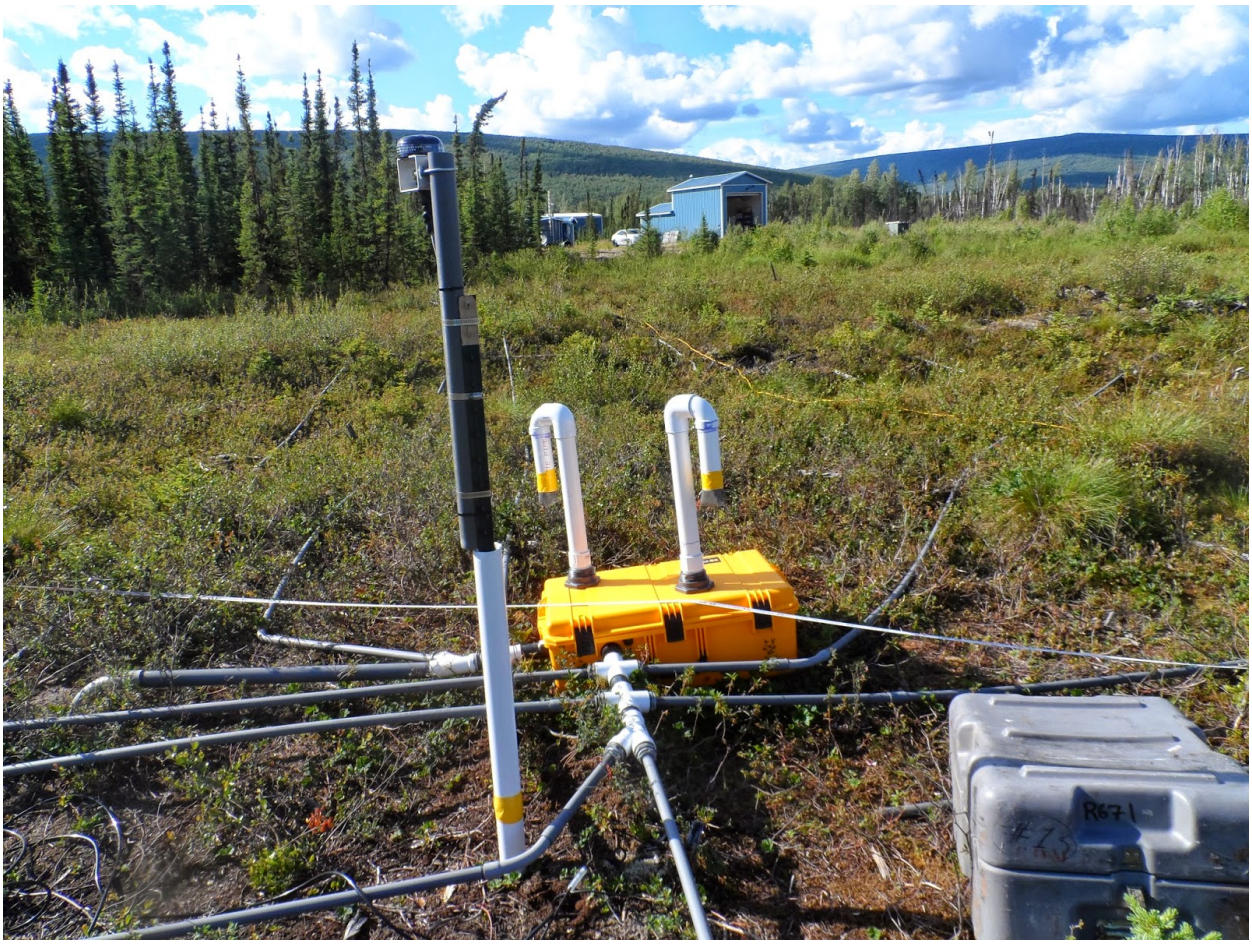

Figure 9: Central element station retrofitted with a fan (inside yellow case) and snorkel system to keep the equipment cool in the summer months. The GPS unit is mounted to the top of the post in the center.

4.2.7 GPS Timing:

The RefTek 130s came with GPS clocks and antennas for timing. We installed the GPS antennas on T-posts high enough (about 1.5 meters) to be above the presumed snow depth (see top of post in Figure 9).

4.2.8 Cable Protection:

The following lines of cables required protection from the environment.

- 2 runs of 100-m length from the building to the array center
- 3 runs of 25 meters to the close-in array elements

- 3 runs of 50 meters to far-offset array elements
- 7 GPS clock cables of 4 meter length
- 7 instrument to DAS cables of 4 meter length

All told, 425 meters of cable had to be armored. We accomplished this by threading the cables through schedule 40 PVC conduit that was then screwed and cemented together to create a waterproof cable run (See Figure 10 for example). This design was chosen because it is resistant to stomping by large animal, such as Moose, and chewing by smaller animals, such as fox or rodents.

Figure 10: Outer ring station configuration showing the cabling and conduit configuration.

4.3 Engineering Results and Data Availability

Below we provide a systematic evaluation of the network's design and state-of-health, along with the unforeseen problems that we encountered operating the remote site. We will also

provide some insight into the Sandia-centric complications that we experienced during the course of the project. Finally, we present the data availability as a qualitative evaluation of the experiment design.

As can be seen from the discussion above, most of our design efforts tried to mitigate the effects of the harsh environment. For the most part, we were very successful in preventing network failure due to the extreme polar environment and in total we had two system failures related to environmental factors. First, we had one system failure related to moisture penetrating a buried seismometer signal cable. This was found to be operator error, as the cable was not tightened correctly. Once the cable was dried out, there were no further problems at that station. Second, towards the end of the recording period, an entire station was compromised when it and the surrounding region became submerged in a local lake. This lake did not appear during the first year of recoding. The station was not re-occupied as there were only a few months left in the deployment. During the extent of the project, there were no issues with stations freezing, animal damage, or other moisture/snow problems. The experiment design and siting were deemed successful by this measure.

Ironically, most of the network's issues arose from intermittent communications and power, which we thought would not be a problem given the site location. Because PFRR is a remote research range and Alaska has frequent and violent storms, the site did not have entirely reliable power or internet access. Also, PFRR was due for a major infrastructure upgrade, scheduled during our deployment, which compounded the issues. We note here that detecting network outages from Albuquerque was difficult given that the network could not be accessed from behind the Sandia National Laboratories' firewall. This meant that the network state-of-health could only be evaluated from offsite. Repeated attempts to open a reliable hole in the firewall were unsuccessful and ultimately we decided that it was a waste of resources to pursue the matter further.

Another complication with the field site arose from our reliance on PFRR staff to aid us with small network repairs. Although we paid personnel at PFRR a small fee for this onsite maintenance, other, presumably higher, priorities often led to delayed response on their part.

This was especially true during the winter months when PFRR is performing rocket launches. Compounding this were the personnel shortages in the summer months, which is an optimal time for vacation in Alaska. In retrospect, the experiment may have been more successful if we had chosen to pay a UAF graduate student's stipend for help maintaining the array.

Despite the frequent network outages, we were able to recover a substantial amount of data. Figure 11 shows that we acquired representative data for all seasons during the course of the two-year monitoring period. Subsequent analysis also showed that we successfully captured both the thickening and the thinning of the active layer, which was the ultimate goal of the project.

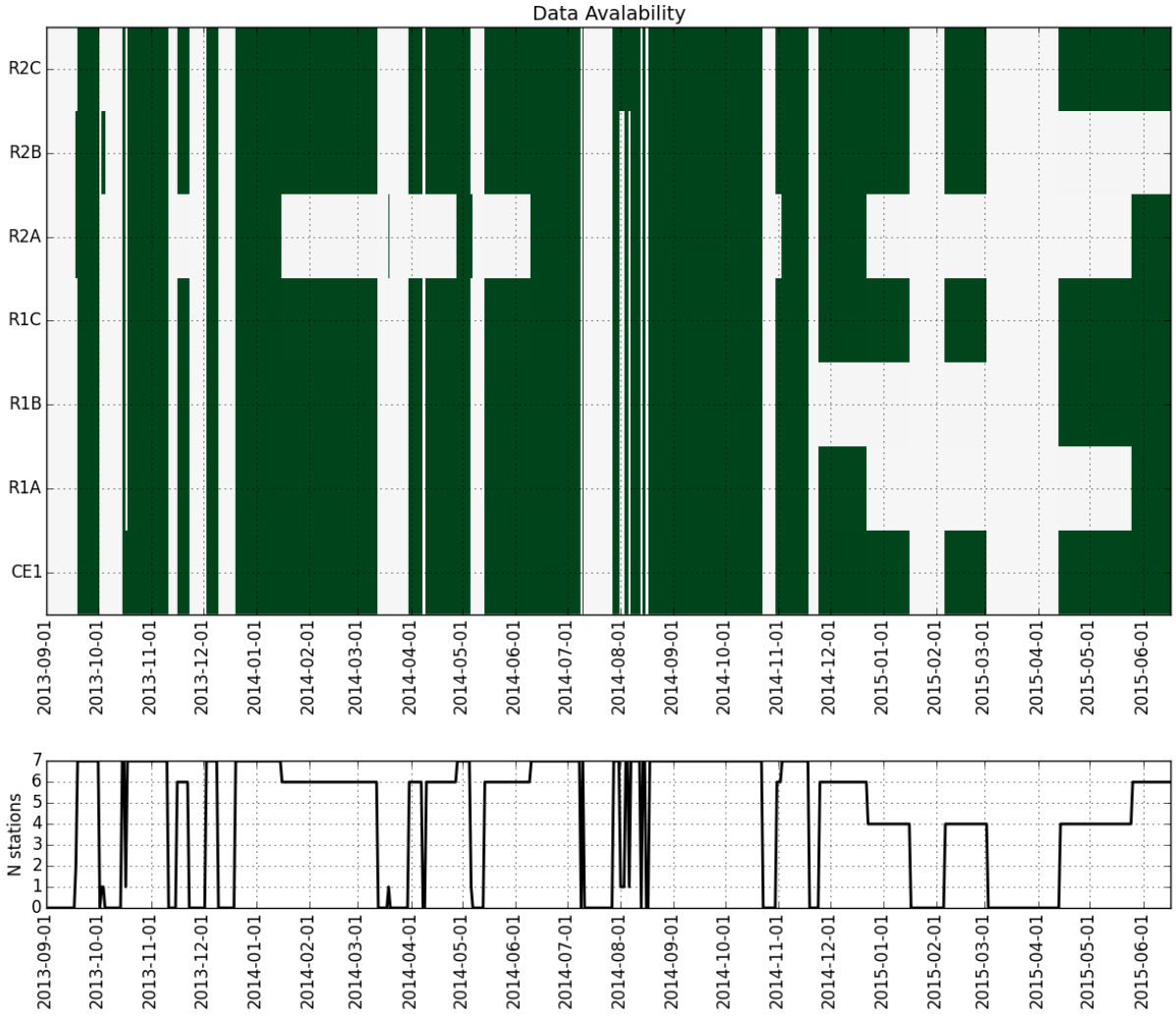

Figure 11: Data availability plot from the continuous recordings at PFRR. Green areas designate time periods when data is available for a given station. The bottom plot illustrates the number of stations available as a time series.

5. GROUND TRUTH MEASUREMENTS

We acquired three traditional (i.e. more common) datasets throughout the course of the project for two purposes: 1) To compare our results with more established methods; and 2) To use the results as constraints (i.e. ground truth) for our newer methods. Dataset 1 is an active-source surface wave study conducted the week of July 9, 2014, using the Refraction-Microtremor method. We note here that all details for this survey and the data mentioned in the text below can be found at the IRIS Data Management Center (IRIS DMC). Dataset 2 was a cross-borehole study conducted June 16th and 17th, 2015. Dataset three was a tile-probe survey that concurrently acquired with datasets 1 and 2 (and two additional times, see Appendix A: Active Layer Thickness Measurements for details).

5.1 Data Set 1: Refraction-Microtremor

Measuring shear-wave velocity with depth is common practice in the geotechnical industry. V_S30, defined as average shear-wave velocity in the shallowest 30 meters, is a parameter in International Building Codes and in probabilistic seismic hazard calculations. There are several accepted ways to measure V_S30, including cone penetrometers or borehole velocity studies. In addition to those methods, surface-waves surveys (such as Single-Channel Analysis of Surface Waves (SASW), Multichannel Analysis of Surface Waves (MASW), and Refraction-Microtremor (ReMi)) are used when non-destructive tests are needed. Surface-wave methods have the additional benefit of being significantly faster and cheaper.

The ReMi method of Louie (2001) builds upon the slowness-frequency (p-f) methodology of McMechan and Yedlin (1981). Slowness, denoted by the letter 'p', is simply the inverse of velocity. The p-f transform is a wave-field transformation from the distance-time field to the slowness-frequency field. The first step in the p-f method is the p-τ (slowness-intercept time) transform, or slant-stack. Just as normal moveout (NMO) summation attempts to amplify reflections on multi-channel records by summing along hyperbolic curves in the distance-time wavefield, the slant-stack attempts to amplify arrivals with linear moveout by summing along lines of constant slowness. Surface waves, given their linear moveout and generally large amplitudes, are prominent on τ -p plots created during slant-stacking. The second step in p-f

analysis is to compute the power spectrum (squared magnitude of the complex Fourier transform) along the intercept-time direction to create a representation of the spectral power at discrete p-f values. Louie (2001) added a spectral ratio across all slowness' for a given frequency to McMechan and Yedlin's (1981) method so that signal strength variations with frequency are eliminated. This final step aids in the interpretation of dispersive arrivals. Then, the peak amplitude of the p-f plot is picked to create a surface-wave dispersion curve (i.e., the frequency vs. velocity relationship). Finally the dispersion curve is inverted for seismic shear-wave velocity versus depth. Because the survey was conducted in the summer months, the active layer should be recognizable in such a plot as an extremely slow layer at the surface, underlain by faster layers of frozen soil or rock.

Before discussing the results of the ReMi survey, would like to discuss the field conditions. Permafrost terranes have a reputation of being one of the most challenging places to acquire field data, and this case was no exception. In ordinary circumstances, say in New Mexico or Nevada arid conditions, ReMi transects can be laid out and acquired in a matter of 1.5-2 hours. As such, we had planned acquisition of 8 ReMi transects of varying lengths and station spacing during our field deployment. We were only able to acquire three lines in our time at PFRR.

Coupling of the geophones to the ground proved the most challenging and time consuming aspect of the survey. Out first aborted attempts at collecting good data consisted of simply pushing the geophones into the thawed active layer by hand. Data quality signal-to-noise ratio in this case was extremely poor. We surmise it was largely due to the tilt of the geophones during the deployment, as the active-layer has little to no shear strength to hold the phone vertical. Out next attempt to acquire reasonable data involved placing the geophones deeper in the column such that the spike penetrated some distance into frozen soil. This proved to be untenable as the depth-to-permafrost in some areas was greater than others. We finally settled on using a small-diameter pipe and handheld sledgehammer to pound holes in the active layer to a consistent depth, approximately 30 cm. Then, as the pipe was removed, we poured clean, dry sand (provided by PFRR but of the sort you can get at the hardware store) into the hole before it closed. We then inserted the geophone into the sandy medium to uniform depth.

Coupling the source (i.e. a metal plate struck by a sledgehammer) also greatly contributed to the much slower data acquisition. The mossy surface acted like a shock absorber and the ground had to be cleared to a depth of approximately 10 cm to get to any sort of soil layer. If this was not done each and every time (the metal plate was 30 cm square) all energy was lost onto the mossy layer.

5.1.1 ReMi Transect #1 Acquisition

The first ReMi survey was completed on July 9, 2014. The weather was reasonably warm and calm. Using 48 4.5 Hz resonance-frequency geophones, the survey line was laid out with 1.5 meters spacing beginning at station R2A and terminating 4.5 meters from station R1C (Figure 12). For this survey, the geophones were placed in the ground by lightly hammering them in with a PVC pipe. The calibration tests showed that all geophones were operational, but observations of variable ground coupling were noted. Observations suggested that some of the geophones might have been deployed in a tilted fashion (see discussion above).

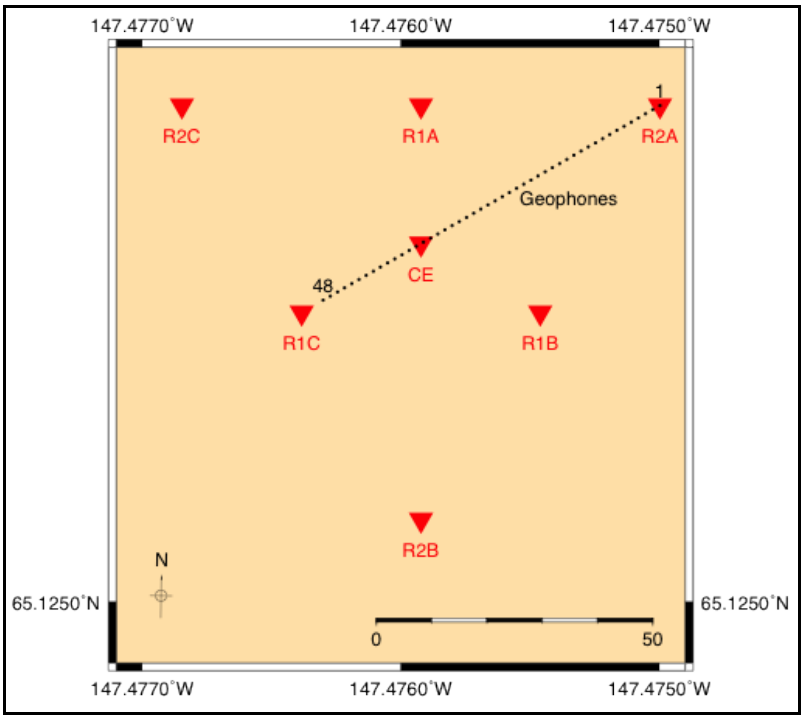

Figure 12: Map of ReMi Survey #1. Upside-down red triangles indicate locations of permanent seismic stations while black dots represent the locations of the 48 geophones.

For this survey, three files were collected each consisting of a stack of 16 shots from various source locations: 4.5 meters northeast of R2A and channel 1, 7.5 meters southwest of station R1C (12 m southwest of channel 48), and halfway between channels 24 and 25 (See Figure 12 & Table 2). The source for all 48 shots in this survey was a 3.6-kg hammer. See Appendix B: ReMi Geophone Locations July 2014 for latitude and longitude receiver locations.

Table 2: Description of Data Acquisition for ReMi Survey 1

File Name	Source Type	Latitude	Longitude	Source Location Description
110.segy	8.0 lbs. hammer	65.12582542	-147.4749148	4.5 meters off channel 1, towards the east-northeast, as an extension of the receiver line
111.segy	8.0 lbs. hammer	65.12543523	-147.4765216	12 meters off channel 48, towards the west-southwest, as an extension of the receiver line
112.segy	8.0 lbs. hammer	65.12564715	-147.475649	Half way between channels 24 and 25

5.1.2 ReMi Transect #2 Acquisition

The second ReMi survey was also conducted on July 9th, 2014 with the weather turning more towards a mix of rain and sun. The survey was deployed along the same azimuth as transect #1, but much shorter with only 33 cm spacing between geophones (Figure 13). To overcome the issue of weak ground coupling and tilted orientation, geophones were emplaced in 10 cm holes that were pre-dug then back-filled with sand (see discussion above). The calibration tests for this survey showed a better signal-to-noise ratio than transect #1.

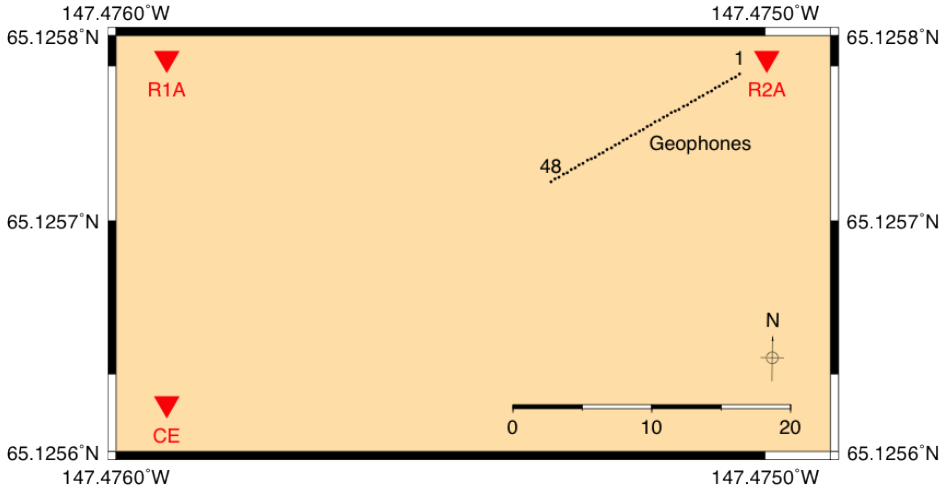

Figure 13: Map of ReMi Survey #2. Upside-down red triangles indicate locations of permanent seismic stations while black dots represent the locations of the 48 geophones.

For this survey, both the 3.6-kg and 1.1-kg hammers were used in three separate locations. The first four groups of shots originated 2.4 meters to the northeast of station R2A. Following this, the next four groups were shot from 2.3 meters southwest of geophone 48 and the final group had a source location 5.1 meters southwest of geophone 48. See Table 3 for source locations and Appendix B: ReMi Geophone Locations July 2014 for receiver locations.

Table 3: Description of Data Acquisition for ReMi Survey 2

File Name	Source Type	Latitude	Longitude	Source Location Description
201.segy	8.0 lbs. hammer	65.12581978	-147.4749543	8.7 meters off channel 1, towards the east-northeast, as an extension of the receiver line
202.segy	2.5 lbs. hammer	65.12581978	-147.4749543	
203.segy	2.5 lbs. hammer	65.12581978	-147.4749543	
204.segy	2.5 lbs. hammer	65.12581978	-147.4749543	
205.segy	8.0 lbs. hammer	65.12571106	-147.4753718	2.3 meters off channel 48, towards the west-southwest, as an extension of the receiver line
206.segy	2.5 lbs. hammer	65.12571106	-147.4753718	
207.segy	2.5 lbs. hammer	65.12571106	-147.4753718	
208.segy	2.5 lbs. hammer	65.12571106	-147.4753718	
209.segy	2.5 lbs. hammer	65.12571106	-147.4753718	
210.segy	8.0 lbs. hammer	65.12569409	-147.4754227	5.1 meters off channel 48, towards the west-southwest, as an extension of the receiver line

5.1.3 ReMi Transect #3 Acquisition

Third ReMi dataset was taken outside the SNL array area near an IRIS station called PIC. Data and information pertaining to this station can also be found at the IRIS DMC. We chose to acquire this data because the PIC station had already been in operation for a full season, unlike the PALSIE array. The PIC array, which is situated on an eroding ridge top, is not on permafrost. We do not present the results for tis acquisition, but note that the signal-to-noise was greatest for this collect, and the acquisition was by far the easiest.

5.1.4 Remi Results

As mentioned previously, low signal-to-noise ratio and energy coupling proved to be challenging aspect of this survey. While the ReMi results are on the poor side (as compared to other surveys performed by the team), they are interpretable. Figure 14 shows the p-f plots and subsequent dispersion picks on transect #2. Since the dispersion curve had restricted bandwidth, we were forced to fix the active-layer thickness at 40 cm (from the results of the concurrent tile probe measurements, 5.2 Data Set 2: Tile Probe Measurements). Doing this showed that the ReMi dispersion results were consistent with the "known" active layer thickness. That is, we could construct a shear-velocity model that resulted in a dispersion curve that closely matched the observations. As can be seen in Figure 14 (right), a fast layer overlies an extremely slow shear velocity layer. To make the dispersion fit, however, this fast layer was made to be thin, and the model required a relatively thick section of relatively slow material underneath it. The result of the inversion, while consistent, was viewed with some skepticism. This motivated us to acquire the cross-borehole dataset (5.3 Data Set 3: Crosshole Seismic Survey) in 2015.

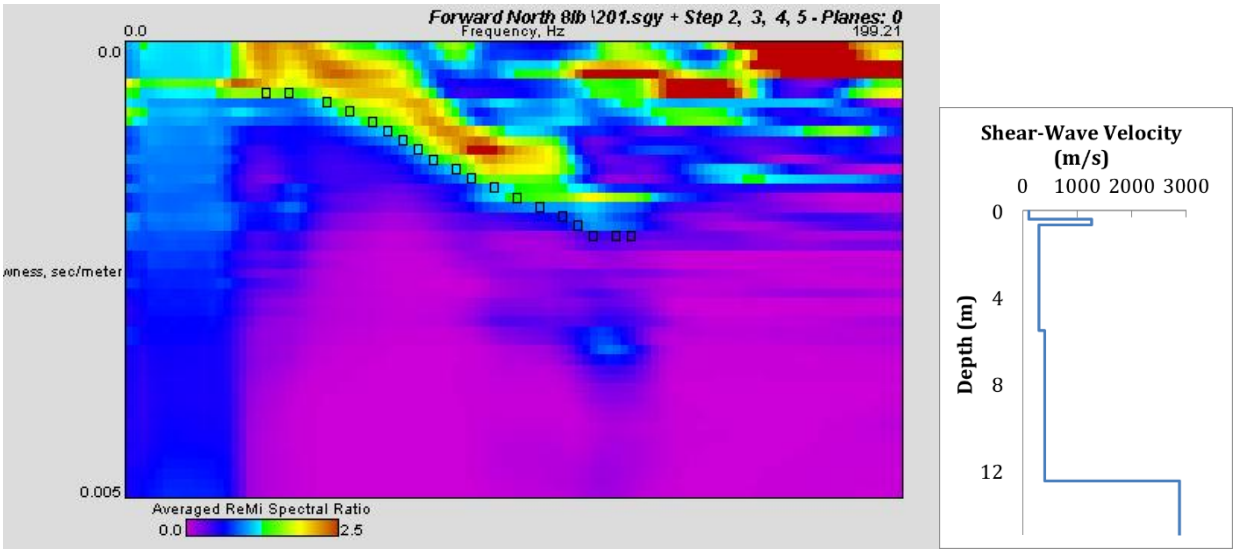

Figure 14: P-F Plot (left) and subsequent dispersion curve (right) from ReMi survey performed along transect #2.

5.2 Data Set 2: Tile Probe Measurements

A tile probe is a thin steel rod with a pointed tip and a bar-type handle at the top. For these measurements, the tile probe was inserted into the soil until it met refusal at the top of the frozen ground. We then measured the thickness of the active layer by grasping the tile probe at ground level and measuring the distance between that point and the tip at the end of the tool. This measurement method is considered the most standard and common for active layer thickness measurements (e.g. Nelson et al. 1996 and Jorgenson et al. 2006).

5.2.1 Tile Probe Acquisition

We conducted tile probe transects over the entire array in the summers of 2014 and 2015. These transects were coincident with the perimeter of the survey area and included one diagonal measurements through the center of the array (see Figure 15 & Figure 16). In addition, probe measurements were made just at the stations themselves on two other occasions (See Appendix A: Active Layer Thickness Measurements). The consistency of these measurements on an individual survey basis was maintained by ensuring that the same person inserted the tile probe and felt a similar refusal each time. This can be a subjective measurement since there was occasionally a transition zone, where the top of the permafrost was soft enough to insert the rod a short distance (i.e. 1-10 cm).

5.2.2 Tile Probe Results

Survey results are shown in Figure 15 & Figure 16. In general, both surveys show the active layer to be less than ~0.75 m thick through most of the array at the time of acquisition. There are two notable results from the combined surveys, however. Firstly, for the most part, the depth of the active layer is remarkably consistent for most of the array area. This bodes well for the hypothesis that small-aperture arrays can be used to generalize conditions over a wider area. Secondly, the exception to this uniformity is evident in the northwest corner of the array, which is coincident with a black spruce forest. Note that the HVSR, multi-station method, and remote sensing results all point to different behavior fir the northwest section of the array. It is our interpretation that the northwest corner of the array is on "degraded" permafrost and the spruce trees act as an insulator.

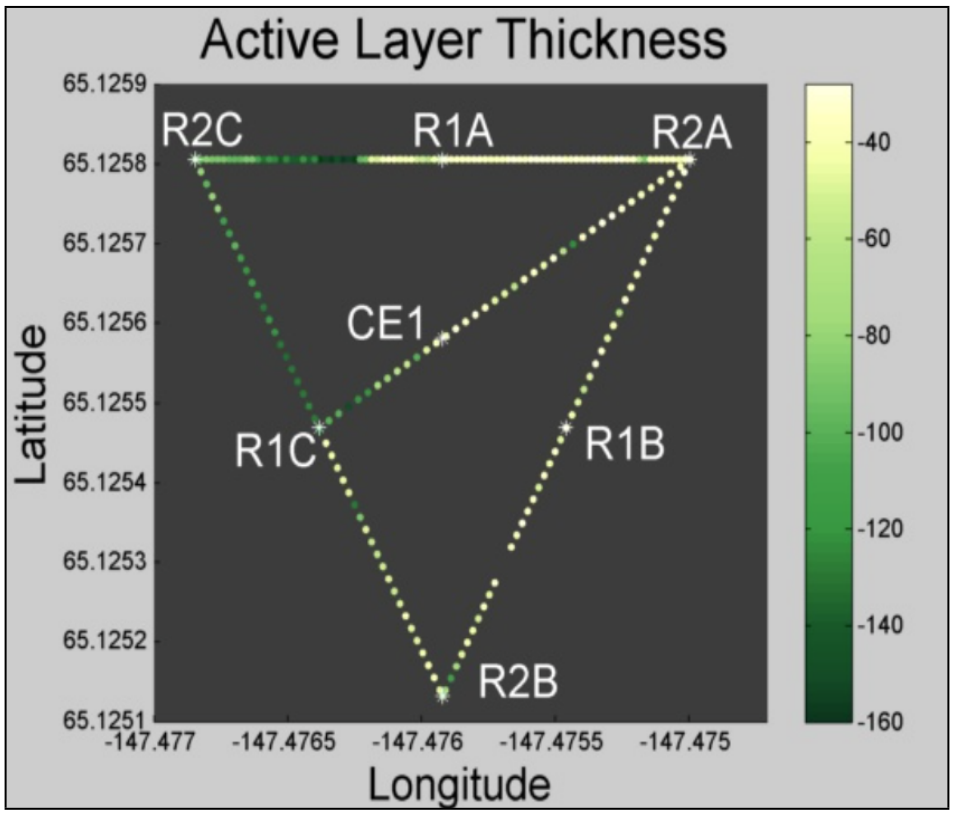

Figure 15: Active layer thickness map obtained from a tile probe investigation conducted in July 2014. Station names are shown for reference. The investigation shows that the active layer thickness is greater in the northwest corner of the survey area. This region is densely populated with Black Spruce, which has been correlated with degraded permafrost.

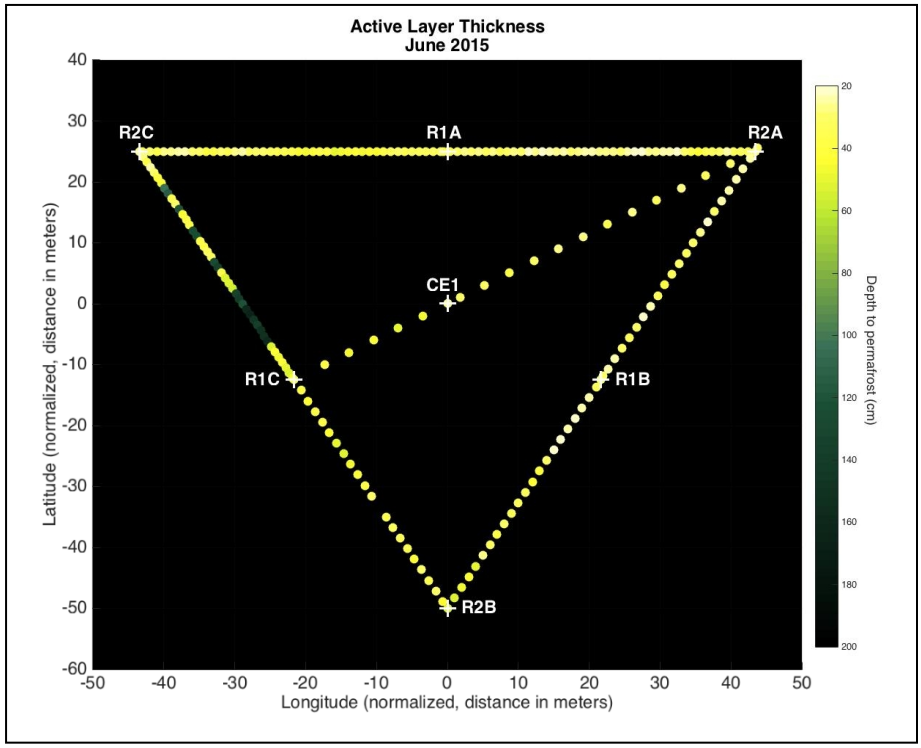

Figure 16: Active layer thickness map obtained from a tile probe investigation conducted in June 2015. Station names are shown for reference. Note that in this case the Latitude and Longitude have been normalized on the horizontal and vertical axes. The investigation shows that the active layer thickness is greater in the area between R1C and R2C.

5.3 Data Set 3: Crosshole Seismic Survey

The poor signal-to-noise ratio and subsequent inconclusive results of the ReMi surveys motivated us to acquire a crosshole seismic survey on the boundary of the survey area. Crosshole seismic (CS) methods are often thought to be the most rigorous method of determining shear-wave velocity with depth. The measurement method is not without weaknesses, however, since they are essentially point measurements and fine scale velocity perturbations may be missed. Understanding this limitation, we chose to conduct our survey in the northwest part of the array, where tile probe measurements indicate that the active layer is a consistent thickness over larger areas. This data collect coincided with the tile probe survey conducted in June 2015. The team

contracted Olson Engineering, Inc. (Olson) to coordinate the drilling of the boreholes and conduct the survey.

The CS survey was conducted by geophysicist Paul Schwering on June 16th and 17th, 2015. Sandia personnel, Matthew Perry and Stephanie James, supported the field effort. The CS test was performed in accordance with ASTM standard D4428-M00. The following sections present the geophysical method, survey specifications, processing parameters and procedures, and results from the investigation.

5.3.1 Methodology

The CS survey was performed in accordance with ASTM D4428/D4428 M-00 in order to measure the in-situ compressional (P-) and shear (S-) wave velocity values of soils and rock with depth. The test requires a minimum of two boreholes– one for the seismic source and one for the receiver. To perform a CS survey, a three-component electromechanical source (capable of producing upward, downward, and horizontal impacts) is lowered to the bottom measurement depth in one borehole and is coupled to the casing with an air-pressurized piston. A tri-axial geophone receiver (comprised of vertical, radial, and transverse measurement components) is then lowered to the same depth in each adjacent borehole and is coupled to the casing by inflating an air bladder. The source generates horizontally-polarized P-wave energy with horizontal impacts, while up and down impacts generate vertically-polarized S-wave energy. The two vertical reversed impacts and corresponding polarizations are used to enhance S-wave identification over random noise (e.g., local mechanical vibrations or traffic). For the CS method, the radial and transverse components are used to record P-wave energy, while the vertical component records S-wave energy. Once the measurements at a given depth are complete, the source and receiver(s) arrays are moved up to the next measurement depth.

5.3.2 Survey Specifications

Two boreholes were completed for CS testing under the supervision of Shannon & Wilson, Inc. (Shannon & Wilson). Each borehole was cased with 2.5 inch (6.35 centimeter) I.D. PVC pipe, grouted in-place. The ground surface was uneven, but the tops of the borehole casings were at approximately equal elevations. Therefore, the top of casing (TOC) was used as the

depth reference for the CS survey. The distance from the ground surface to TOC was also measured at each borehole (Figure 17). The horizontal distance between the boreholes was 3.93 meters, measured at TOC (Figure 17). The maximum measurement depth was 21.64 meters below TOC. The CS source was placed in the southwestern borehole, and the CS receiver in the northeastern borehole (Figure 17). The survey was performed by moving the source and receiver up from the bottom at 30.48 cm increments following each set of three-component measurements. Data were collected up to 1.52 meters below TOC; however, data from 1.52 to 3.05 meters below TOC were unusable (i.e., too noisy).

Figure 17: View of the CS boreholes, looking approximately northward, during deviation logging.

5.3.3 Processing Parameters and Procedures

CS analysis typically begins with picking the P- and S-wave arrival times, which Olson conducted for each record. Stack plots of the CS records and arrival time picks are provided as figures in Appendix C: Waveforms Acquired at Poker Flat. P-wave arrivals were picked on both

the radial and transverse components; for each depth, the highest-quality pick of the two components was selected as the P-wave arrival. S-wave arrival times were nominally picked on the vertical component, using the overlaid up- and down-impacts. However, electronic cross coupling (aka cross talk) between the source and vertical receiver channel distorted the traces at depths from 58 to 69 feet below TOC. The S-wave arrival times, for this specific depth interval, needed to be picked from the radial component instead of the vertical component. See Appendix C: Waveforms Acquired at Poker Flat for figures related to the picking described here.

Taking into account the borehole deviation logs, the P- and S-wave travel time picks were used to create seismic velocities assuming straight ray paths from source to receiver. Poisson's Ratio, and contained and shear moduli were calculated from these values, assuming formation density (see Appendix E: Seismic Velocity & Elastic Modulus Table).

5.3.4 CS Results

A P- and S-wave velocity plot from the CS survey is shown in Figure 18. Borehole lithology, as reported by Shannon & Wilson, is comprised of frozen gravel sand and sandy gravel with occasional cobbles in the CS measurement range (3.35 to 21.64 meters below TOC). This unit overlies schist bedrock, encountered at a depth of 22 meters below TOC. Refractions from the underlying bedrock are associated with the significant velocity increases at the base of the velocity profiles (> 20 meters below TOC).

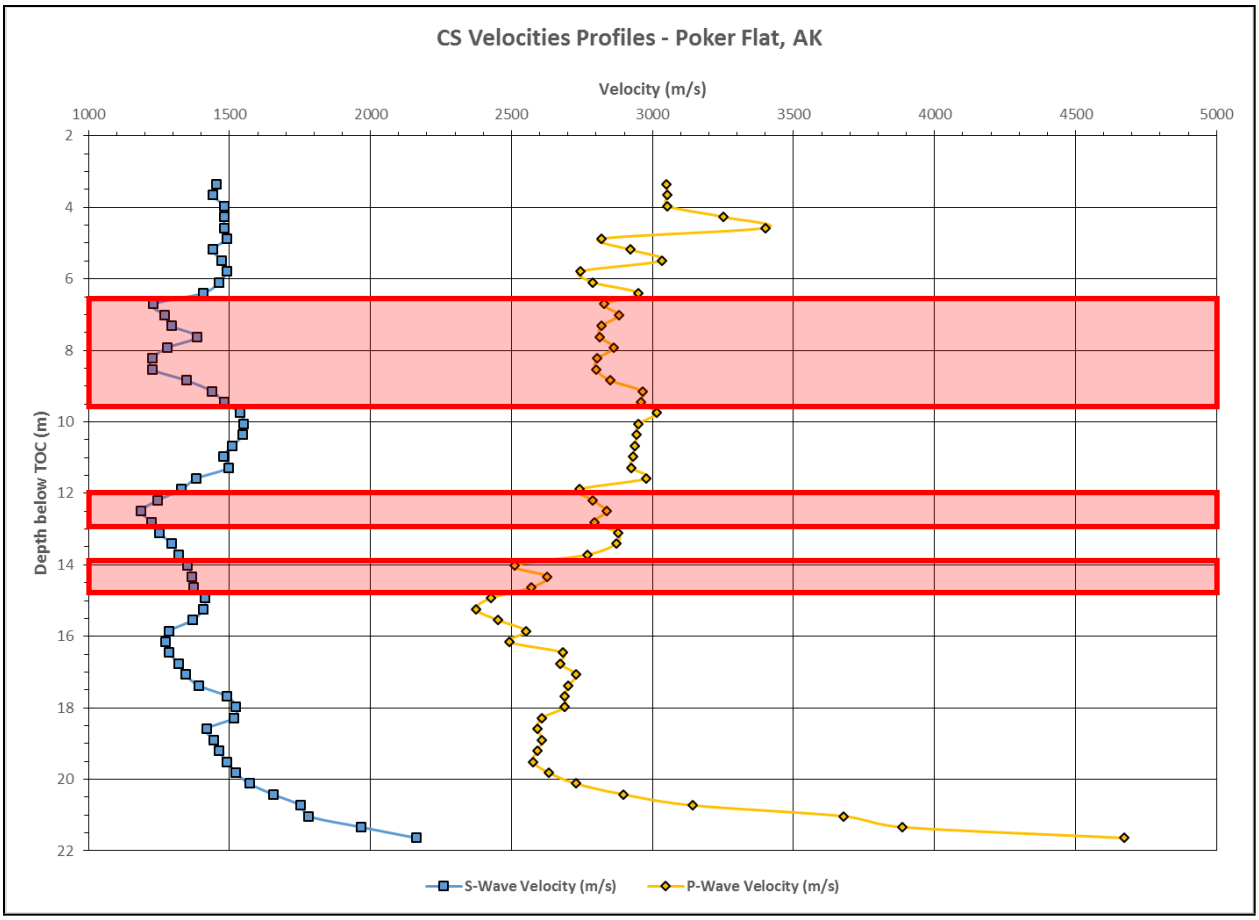

Figure 18: CS velocity profiles. Low data quality zones are indicated in red.

Nominally, the quality of the P-wave data was good, and the S-wave data was generally very good. However, there were three depth zones of low quality data: 6.5 to 9.5 meters, 12 to 13 meters, and 14 to 15 meters below TOC (Figure 18). The confidence in the velocity calculation, and thereby the resultant elastic moduli, is low in these zones. The low quality signals in these zones are characteristic of poor casing-to-formation coupling. For these specific depth zones, there are no distinct indications from the CS data or from the drilling/grouting reports as to the cause of the poor coupling. The most likely explanation is that the thermal effects of drilling and grouting processes may have produced isolated thawed zones (co-located with localized inhomogeneities in the nominally frozen substrate), which would create a condition conducive to poor grout / casing / formation coupling. Shannon & Wilson personnel reported that refreezing of thawed formation could take as long as several weeks. It is possible that resurveying these depth sections would result in better data at a later date, assuming that the holes are not plugged and abandoned.

The broad P-wave velocity trend is a gradual decrease from approximately 3,100 m/s near the surface down to approximately 2,900 m/s at approximately 11.5 meters below TOC. The P-wave velocity then decreases to between approximately 2,400 and 2,800 m/s from 11.5 to 17.5 meters below TOC. The S-wave velocity profile is nearly constant at 1,500 m/s to a depth of approximately 11.5 meters below TOC (notwithstanding the low velocity zone of poor data quality). From 11.5 to 17.5 meters below TOC, the S-wave velocity values are lower, ranging between approximately 1,200 to 1,400 m/s. The velocity profiles are noisy and unreliable from 17.5 to 21 meters below TOC, and then increase in response to refractions from the schist bedrock. To summarize, the velocity plots indicate 1) a relatively high velocity zone approximately 3 to 11.5 meters below TOC, then 2) a relatively low velocity zone from approximately 11.5 to at least 17.5 meters below TOC, and finally 3) a sharp increase in velocity due to bedrock.

5.4 Summary of Ground Truth Measurements

We conducted three types of surveys over the three-year project for the purposes of providing ground truth for the unproven ambient noise methods. As we have noted above and will discuss further below, all three had their strengths and weaknesses. Consequently, our experience demonstrated why improved methods to measure active layer thickness are necessary.

The CS survey adequately determined bulk velocities deeper than 3 meters. Coupled with the drilling reports, the method was also able to definitively measure the depth-to-bedrock. Unfortunately, the inability of the method to resolve shallow layers in this situation is a fatal weakness, as the active-layer was shallower than the uppermost resolved layer. Also, unknown factors (i.e. poor grout coupling, potential cross talk between the instrumentation) caused poor signal quality at certain depth intervals. It is possible that Olson's assessment is correct and the drilling process melted the in situ soils in these sections and that this situation could resolve itself with time.

ReMi measurements were extremely time consuming and difficult to acquire. Poor source and receiver coupling led to bandwidth-constrained dispersion curves. This in turn led to depth

reconstructions, while consistent with tile probe measurements that poorly resolved deeper velocities and exhibited a general lack of uniqueness.

Not surprisingly, as they are the "standard" method of active-layer thickness measurements, tile probing proved to be the most satisfactory method. Of course, it too suffers from drawbacks that this LDRD was hoping to alleviate. That is, the requirement of costly site visit, the resultant sparcity of the year-to-year datasets resulting, and the lack of any spatial and temporal resolution below the top of the permafrost. The latter could be important for understanding the deeper effects of changing active layer thickness in discontinuous permafrost regions.

All told, fusing the three methods yielded some improvement for determining the shallow velocity structure at the site. ReMi was unable to resolve deeper layers, while CS was unable to resolve shallower ones. ReMi suffered from non-uniqueness, but fixing active layer thickness with tile probe measurements and deeper velocity from CS resulted in an adequate model for our purposes.

6. HORIZONTAL-VERTICAL SPECTRAL RATIO (HVSR) – SINGLE STATION METHOD

6.1 Introduction

Near-surface soils have long been recognized as having a great effect on seismic recordings. These effects, such as travel time delays, or frequency dependent attenuation or amplification, are often termed "site effects" and are generally regarded as a signal to be minimized or corrected when analyzing earthquakes or active-source seismic data. This is understandable when the goal of the research is the source properties of a distant earthquake or a deep reflection off oil-bearing reservoir rocks. There are situations, however, when site effects are a useful signal to be exploited, rather than disregarded. For instance, frequency dependent ground motion amplification is of interest when trying to predict ground motions from earthquakes (e.g. Field and SCEC Working Group, 2000; Aki, 1993). Other uses of site effects include determining the depth of alluvial basins (e.g. Le Roux, et. al, 2009; Poggie et al., 2015) or in geophysical prospecting to find the nearest strong reflector (Curtis et al., 2006; Dragonov, et. al, 2007). As will be discussed below, stations on permafrost should have a very strong site effect. Moreover, the site effect should be time-dependent, as the freezing and thawing of the active layer modify the bulk properties of the surficial soils dramatically.

6.2 Causes of Site Effects

Near surface soils are almost always seismically slower than the underlying materials. This leads to a number of phenomena that can be observed by seismometers installed at the surface.

1. As seismic waves traveling in deeper, faster, formations approach the surface, they pile up in the slow surface soils, depositing more energy per unit time. This results in amplification of ground motion.

2. Amplification can also occur when seismic waves are trapped in the near surface layer. The soils at the surface are sandwiched between highly contrasting layers. The upper boundary is the air above the ground, and the lower boundary is the stiffer, less weathered soil or rock below. This creates a situation where strong reflections at both interfaces keep seismic waves (especially horizontal shear waves) from leaving, thus

amplifying the ground motion. This is called body-wave resonance and the effect is frequency dependent. The frequency of amplification is inversely proportional to the thickness of the soil layer. The "quarter-wavelength approximation" is often used as a good estimator of the depth to the layer causing the resonance (Boore and Joyner, 1997).

$$f = V_S/(4*h)$$

3. Rayleigh waves are surface waves with "retrograde elliptical" partial motions. That is, for this seismic phase, the ground moves simultaneously in a horizontal plane parallel to the propagation direction, and in the vertical plane. The ratio of horizontal-to-vertical ground motion is called the Rayleigh wave ellipticity. This ellipticity is strongly affected by the physical properties of the near surface geology at the recording site (Aki and Richards (2002) Chapter 5). Under this mechanism, horizontal or vertical ground motion is amplified at the expense of the other ground-motion component.
4. Much like light rays are bent by glass with different refractive indexes, seismic rays are bent by geologic formations with different seismic velocities. This can lead to focusing (amplification) or de-focusing (attenuation) of rays depending on where the measurement is taken.

5. Finally, topography at the surface of the Earth can result in both scattering and focusing effects.

Of the five sources of site effects mentioned above, we expect numbers 1, 2, and 3 to be present on permafrost and be related to the active layer.

6.3 Measuring the Site Effect

There are two commonly used methods to measure site effects. One is called the spectral ratio method (or standard spectral ration method (SR)), and the horizontal-to-vertical spectral ratio method (HVSR). The goal of both methods is to compare a signal at a site that may be amplified to another signal thought to be free of amplification. The SR method does this by measuring the Fourier amplitude of ground motion spectrum at a test it and comparing it to the

Fourier amplitude of ground motion spectrum at another site, installed nearby on rock. The rock site is assumed to be free of site effects, although this is not always the case, in practice (Steidl et al., 1996; Boore and Joyner, 1997). When the SR method is not practical (for instance, if there is no nearby rock site with which to compare), the HVSR method is often used. The HVSR method does not need another site, as it is a single-station method. It compares the Fourier amplitude of vertical motion at the site to the horizontal component of ground motion at the same site. As in the SR method, the HVSR method assumes that the vertical component of ground motion is relatively free of amplification.

We chose to use the HVSR method to measure the site effect at PFRR, as there are no suitable rock outcrops proximal to the array site. In addition, nearby rock sites would also go through freeze/thaw cycles, causing potential complexities. The Geopsy software suite was used for all of our data reduction and computation of the spectral ratios. Processing steps are reproduced below:

1. Record continuous seismic data. Each of the seven array sites recorded three components of ground motion. Sample rates were either 250 or 125 samples per second, depending on the timeframe. Regardless of the sample rate, we present analysis only up to 60 Hz. Spot checks above that frequency showed no relevant phenomena.

2. Following recommendations in Bard (2005) we limited our daily time window to nighttime hours to reduce the influence on cultural noise in our dataset. A nightly window of midnight to 4 AM was used after extensive testing showed that that window produced the most stable HVSR.

3. Within that window, high-amplitude events were removed, so that only ambient noise remained. The high amplitude events were identified by using a short time average/longtime average (STA/LTA) algorithm. Once the event was identified, the data for that event was excised from the time series recorded at that site.

4. For the four-hour daily time frame, the Fourier transform of all three components of

ground motion were computed for 50-second time windows with 5% overlap and subsequently stacked and smoothed. The spectra were smoothed using the method of Konno and Ohmachi (1998) with a smoothing constant of 40. Finally the north-south and east-west spectra were averaged together and ratioed with the vertical component to form the daily HVSR. See Appendix F: Geopsy Parameters for more detail.

6.4 Interpretation and Inversion of Site Effects

Once the site effects have been calculated by the HVSR, the next step is to use the results to infer the geologic structure, which leads to that site effect. Microtremor HVSR has long been known to be sensitive to shallow earth structure (e.g., Nakamura, 1989). In Nakamura's model of body-wave resonance site effects, simple equations delineate (which can be reduced to the quarter wavelength approximation (see #2 in section 6.2 Causes of Site Effects) the relationship among the dominant frequency of the HVSR, the magnitude of amplification at that frequency, and the shear-wave velocity of the surficial layers and the underlying basement (Nakamura, 1998). In our case, the surficial layer is the active layer above permafrost and the "basement" is the permafrost itself. As an example, inserting generalized thawed soil shear-wave velocity (100 m/s) and predicted active-layer thickness for PFRR into the quarter wavelength approximation (0.5 m), the quarter-wavelength equation predicts resonance 50 Hz.

These equations are strictly related to the body wave resonance mechanism. In most circumstances body-wave resonance alone can describe most of the HVSR for ambient noise. However, in the case of a very shallow, very low shear-weave velocity layer, Rayleigh-wave ellipticity has been shown to dominate (Kawase et al., 2015). In cases where it is easy to discriminate Rayleigh waves from other seismic phases, for example as in teleseismic earthquake data where the Rayleigh waves separate in time from body waves and Love waves, methods of inversion for medium parameters is relatively straightforward (e.g Corchete, 2013, Lin et al, 2012). When using ambient noise data, however, no such separation is possible. Modeling HVSR of ambient noise using diffuse field theory, Kawase et al. (2015), are able to separate the influences of body-wave resonances, surface-wave resonances, and ellipticity. In this report, we show preliminary results using the methodology of Kawase et al. (2015) (courtesy of Josè Piña, using a small sample our data).

6.5 Results

Figure 19: and Figure 20 show example HVSR for one station. The HVSR shown is a 7-day geometric mean for two different time periods. As can be seen in Figure 19 for Calendar Week 7 (February), HVSR magnitude is small (maximum amplitude of 1.5 at 2.5 Hz). Above approximately 10 Hz, HVSR amplitude is approximately 1, showing no amplification of horizontal motion at all. In contrast, for the same station in Week 39 (Figure 20, late September, after thawing), the HVSR has a dramatically difference character. The 2.5 Hz peak is still present at about the same magnitude, but higher frequencies show much greater amplitude. Figure 21 shows a progression by week for CE1 for the 2014 calendar year. Note that the spectra are generally flat above 8 Hz for all weeks except the range of approximately Week 31 (early August) to approximately Week 42 (Mid October).

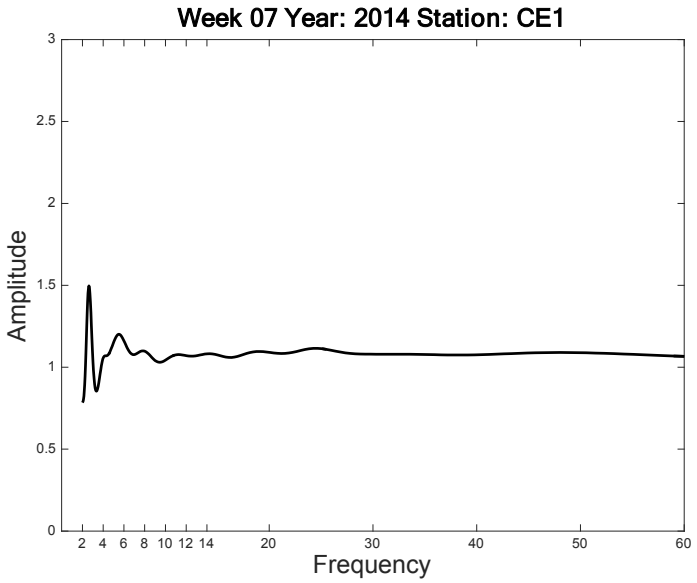

Figure 19: Calculated HVSR for station CE1 of the data stacked during week seven (February 10-16) of 2014. We note here that the maximum amplitude of the HVSR is approximately 1.5 and the ratio is nearly equal to one for frequencies above approximately 10 Hz.

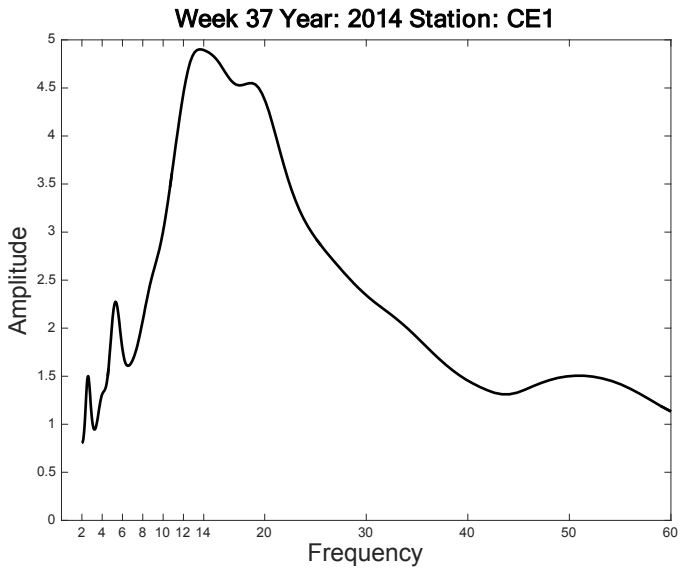

Figure 20: Calculated HVSR for station CE1 of the data stacked during week thirty-seven (September 8-14) of 2014. We note here that the maximum amplitude of the HVSR is much larger (~5) compared to the HVSR calculated in Figure 19 and the ratio is no longer constant or equal to one for frequencies above approximately 10 Hz. This change illustrates the drastic changes observed in calculated HVSR between a zero thickness active layer (Figure 19) and a maximum thickness active layer (shown here).

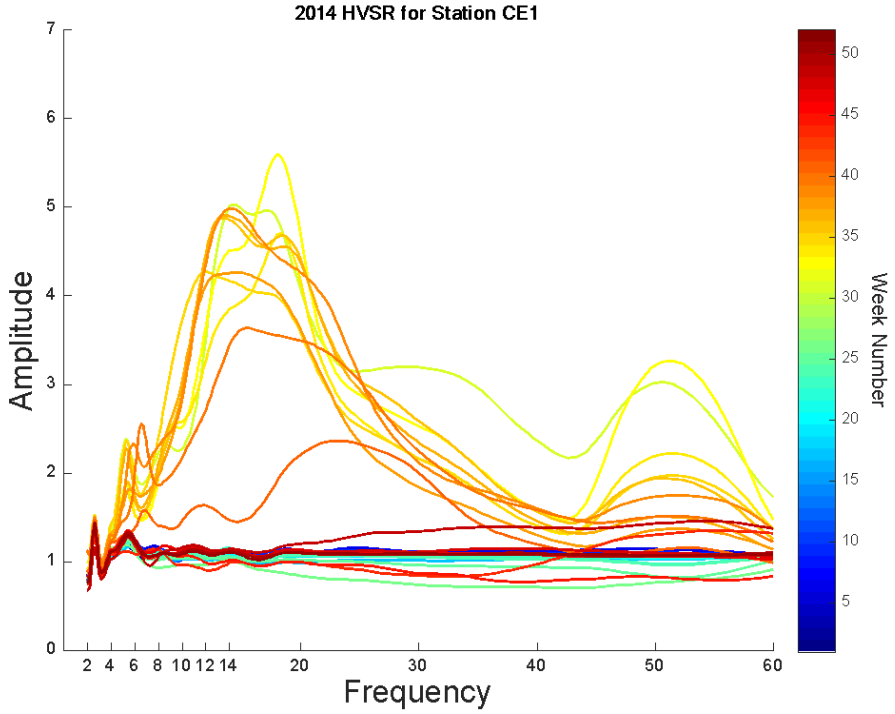

Figure 21: Calculated HVSR for each week in 2014 showing the temporal variations for station CE1. Drastic increases in amplitude for frequencies above ~8 Hz are observed for a time period between August and late September (weeks 31-40). A distinct spectral peak near 50 Hz is also observed during this period of time.

Other stations, such as R1B and R2A (Figure 22 & Figure 23) show similar patterns. The farthest northeast stations in the array, R1C and R2C (see Figure 12 for station configuration) show a different character (Figure 24 and Figure 25). These are stations that either on the outskirts of, or are inside, a stand of Black Spruce trees. Rather then predominately flat spectra for most of the year, these stations have peaked spectra year-round. The 2.5 Hz spectral peak is in common with the rest of the array, but a much higher amplitude peak at around 6.5 Hz is present at both stations. It is interesting to note that the widest range of HVSR values at R1C and R2C is approximately the same (20-25 Hz) as CE1 and the others. We interpret these peaks to be associated with the seasonal thaw. The additional large-amplitude peak at 6 to 7 Hz we speculate is caused by incomplete freezing of the local permafrost during the winter. Either the trees act as an insulator during the winter or the trees were allowed better root systems, or both.

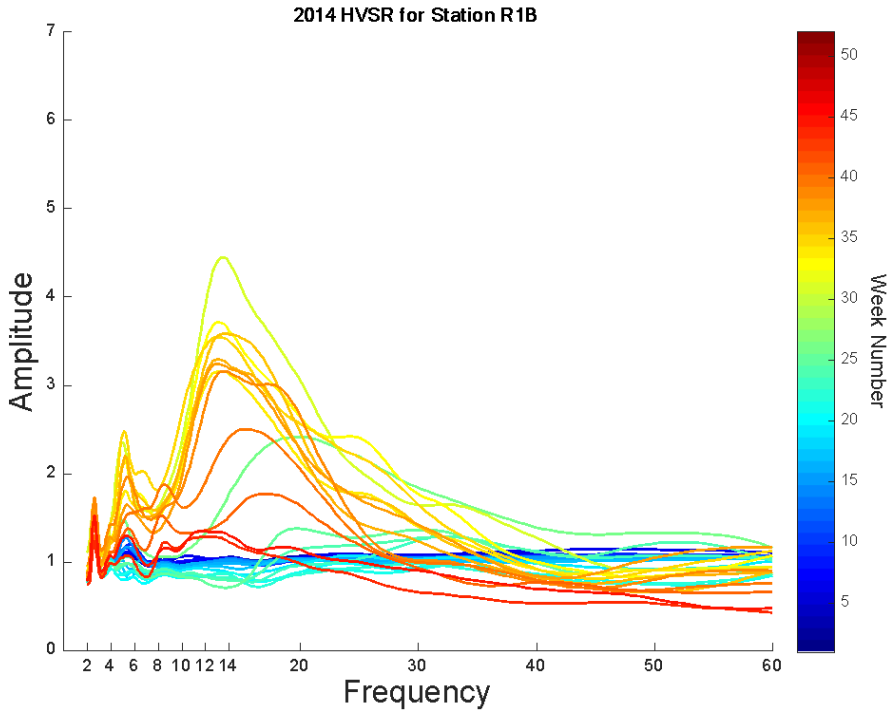

Figure 22: Calculated HVSR for each week in 2014 showing the temporal variations for station R1B. Drastic increases in amplitude for frequencies above ~8 Hz are observed for a time period between August and late September (weeks 31-40). The distinct spectral peak near 50 Hz is not observed.

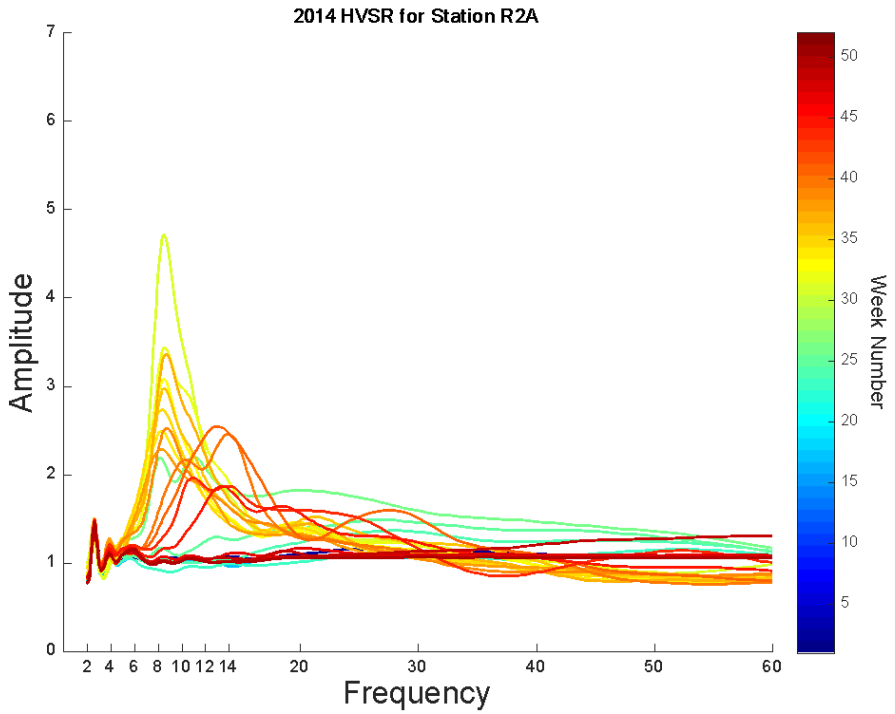

Figure 23: Calculated HVSR for each week in 2014 showing the temporal variations for station R2A. Drastic increases in amplitude for frequencies above ~8 Hz are observed for a time period between August and late September (weeks 31-40). The distinct spectral peak near 50 Hz is not observed.

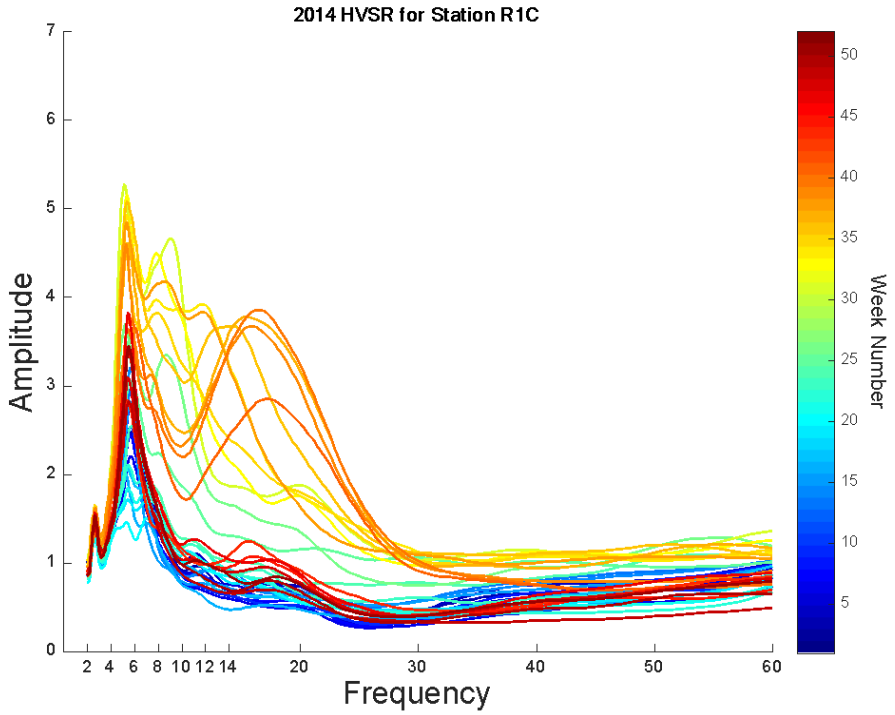

Figure 24: Calculated HVSR for each week in 2014 showing the temporal variations for station R1C. Drastic increases in amplitude (compared to other stations) are seen at all frequencies and at all times of the year. This is presumably attributable to the station's proximity to a black spruce forest.

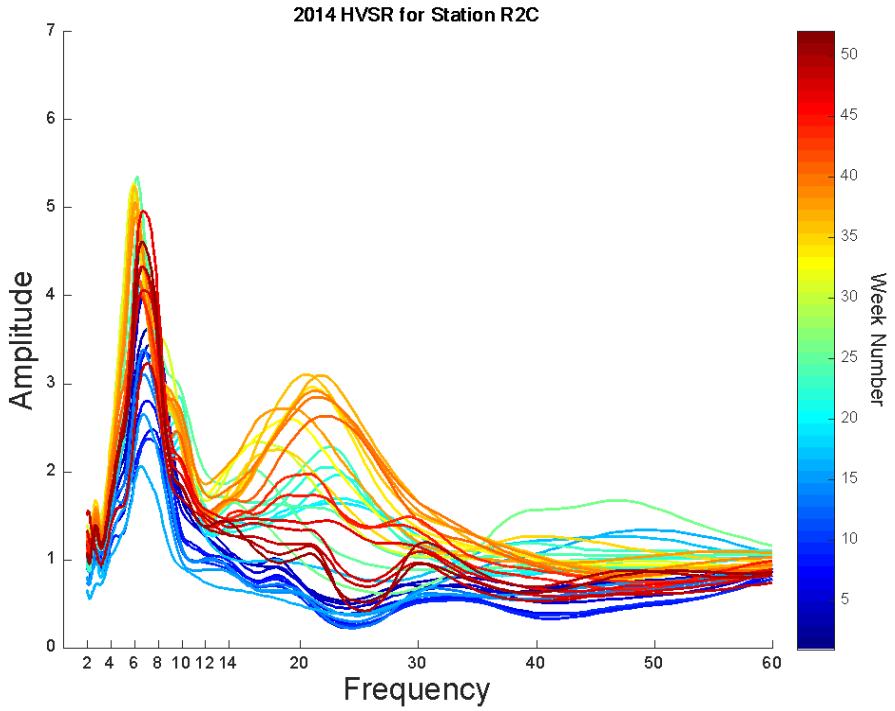

Figure 25: Calculated HVSR for each week in 2014 showing the temporal variations for station R2C. Drastic increases in amplitude (compared to other stations) are seen at all frequencies and at all times of the year. This is presumably attributable to the station's proximity to a black spruce forest.

6.6 Inversion

The simplest relation to convert HVSR to shear-wave velocity vs. depth is the aforementioned quarter-wavelength approximation. There are three "unknowns" in the equation, shear-wave velocity V_s, depth to interface h, and frequency of amplification f. The frequency of amplification is known from the HVSR, so knowledge of either V_s or h is needed to make the equation deterministic. Published values for shear-wav velocity for mud (e.g. Holzer et al., 2005) can be used substituted for the shear-wave velocity or *in situ* velocity can be measured at the site using an active source survey. Similarly, thickness can be measured at the site using a method such as probing. We chose to do measure both values (see Section 5. Ground Truth Measurements) and supplement with published values. Since these measurements were made at discrete times (see Appendix A: Active Layer Thickness Measurements), they should be compared to the concurrent HVSR. Using the quarter-wavelength approximation with h= 45 cm (July, 2014 ground truth, Figure 15 and Table 8 & Table 12 in Appendix A: Active Layer Thickness Measurements), and Vs = 100 m/s (Holzer et. al, 2005; mud Vs, and ReMi results)

results in a peak at 55 Hz. This agrees pretty well with the high frequency secondary peak (52 Hz, Figure 20). This peak does not migrate to 35 Hz, predicted for 68 cm depth (October, 2014 ground truth), however. In order for the peak to remain constant at 52 Hz given thickening active-layer, the shear-wave velocity of the active-layer would have to increase by the same factor. We are not observing this in the HVSR results. This velocity increase is not out of the question, as the active layer freezes and thaws from the top down. It is possible that thawing is still occurring at depth while partial freezing is starting from the top. Average low temperature in the region for October is 17 degrees Fahrenheit. Regardless, body-wave resonances are not adequate to explain the HVSR as the dominant peaks at 15-20 Hz do not match any reasonable shear-wave velocity or layer depth horizons.

Since body-wave resonances fail to capture the entire phenomenology observed, we must assume that Rayleigh-wave ellipticity is a contributing or controlling factor. Figure 26 shows the contribution of body-wave and surface-wave resonances in two generic cases (Figure courtesy of Francisco Sanchez-Sèsma). The two panels (upper and lower) of Figure 26 show a candidate shear-wave velocity profile (left) and the separation of individual contributors to the total HVSR calculation (right). The difference between the two panels resides entirely in the shear wave velocity of the uppermost layer. In the upper case, the layer has a much faster shear wave velocity, which is representative of winter conditions at the site or zero thickness active layer. The lower case represents the summer case or maximum active layer thickness with a much slower shear wave velocity in the shallow layer. The primary difference in these two cases is that in the winter case (upper) ellipticity represents a small contribution compared to the contribution in the summer (lower). Specifically, we see that the ellipticity contribution dominates the total HVSR calculation at 1-2 Hz in the summer case.

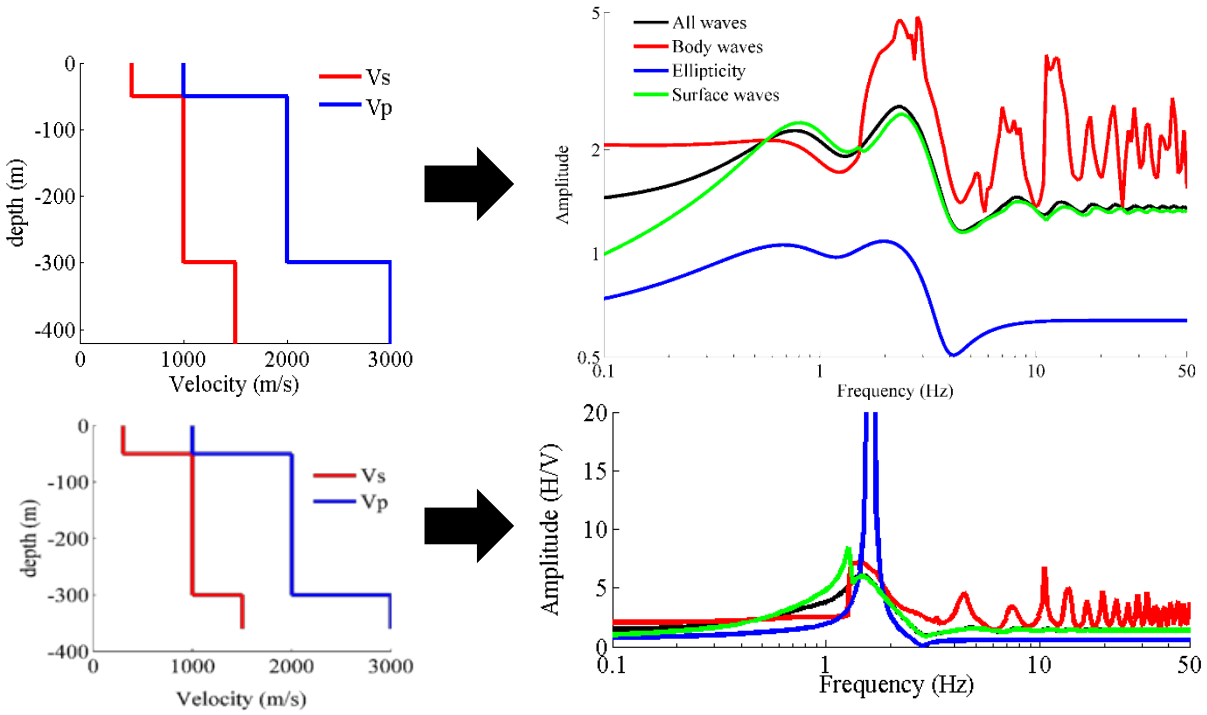

Figure 26: HVSR modeling results courtesy of Francisco Sanchez-Sèsma illustrating the effect of a melting active layer on the contribution of ellipticity to the total HVSR calculation. The upper left plot, which has a relatively fast shear wave velocity assigned for the shallowest layer (a.k.a. active layer), is used to calculate the ellipticity contribution (upper right) for the winter case (active layer thickness is zero). The lower set of plots represent the summer case where the active layer has a much slower shear wave velocity.

To test the hypothesis that the temporal variation in our HVSR results was attributable to a change in Rayleigh-wave ellipticity, we sent sample data to Josè Piña Flores, in Sanchez-Sèsma's research group at UNÀM. This test was conducted to rule out other contributing factors such as a change in ambient noise back azimuth, which can also contribute to temporal changes in HVSR calculations. We chose to send data from station CE1 representing the 7-day mean HVSR for July 2014 (concurrent with the tile probe measurement that showed 45 cm active-layer thickness). Figure 27 shows the measured HVSR in black and multiple realizations of the inverted (i.e. calculated) HVSR in multiple colors. As can be seen, the model fit is quite good and fits the predominant peak well. The shear-wave velocity models leasing to that mode are presented in Figure 28. The model iterations all show two very thin, very shallow, low shear-wave velocity layers. The uppermost layer thickness is 45 cm and the second layer is 2.2 meters thick. It is an enticing result that the uppermost layer fits the layer thickness seen by probing

exactly. Flores cautions, however, that the inversion results are nonlinear and suffer from non-uniqueness (Flores. pers. comm.). Any other ancillary information, such as dispersion curves or velocity models from active-source surveys, can be used to decrease the non-uniqueness, however.

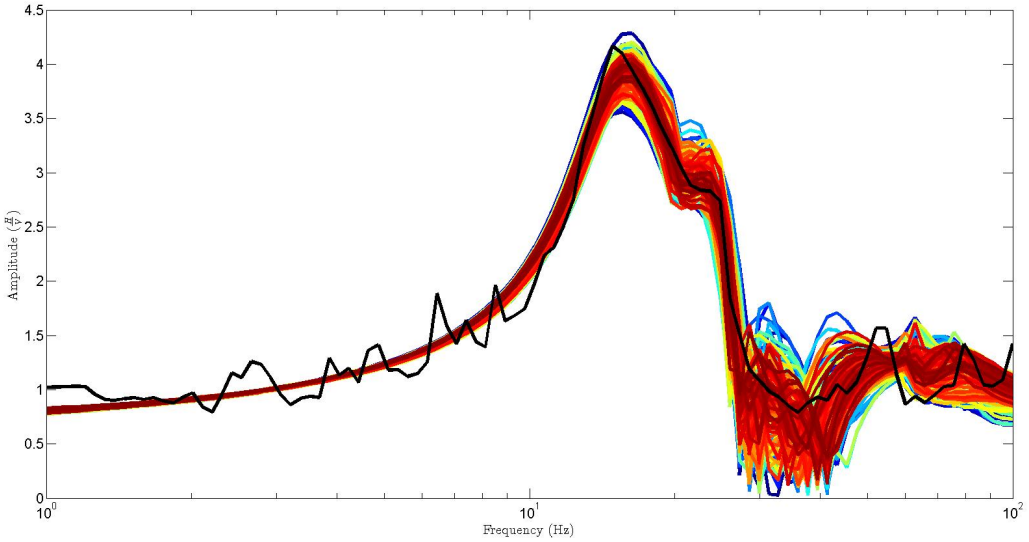

Figure 27: Black line illustrates the mean HVSR for station CE1 during the week in July 2014 when the active layer thickness was measured to be 45cm. The colored lines represent the HVSR calculated for the velocity models shown in Figure 28. We note here that the data fit is relatively good especially for the frequencies between 10-30 Hz, which we propose are attributed to changes in Rayleigh-wave ellipticity.

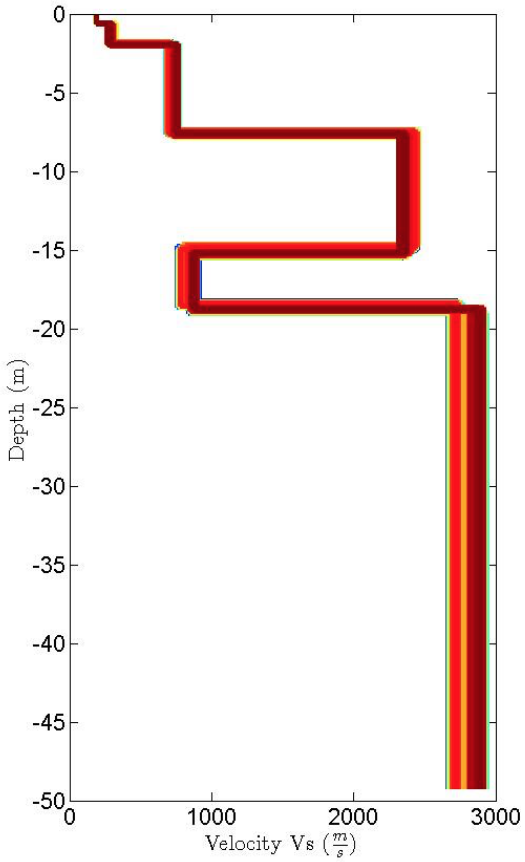

Figure 28: Resultant shear wave velocity profiles calculated from Figure 27. We note the presence of two shallow layers with very low (<300 m/s and <500 m/s) shear wave velocities. The thinnest layer (representing the active layer in this case) is 45 cm thick in this calculation. We caution the reader, however, that this inversion is nonlinear and suffers from non-uniqueness. This issue could be rectified with additional information such as ground truth results.

Unfortunately, we were unable to get the Sanchez-Sèsma group our ground truth data in time for results to be published in this report. We are currently pursuing follow-on funding that may benefit both research programs and lead to more constrained results.

7. AMBIENT NOISE SEISMIC INTERFEROMETRY – MULTI-STATION METHOD

7.1 Method Introduction

As research into ambient seismic noise characteristics expands, so too are the number of techniques for extracting valuable information of the subsurface from the noise wave field. In addition to the single-station HVSR method described earlier, records of ambient noise can also be used in multi-station methods. In particular, the most common technique for processing ambient seismic noise relies on the cross-correlation of records from a pair of stations. Under the assumption of a continuous and diffuse wave field generated by numerous natural and/or anthropogenic sources, the waves that are recorded at one station to then propagate towards, and be recorded by, a second station can be cross-correlated to extract the impulse response (or Green's Function, GF) of the ground between the two stations (Shaprio & Campillo, 2004; Shapiro et al., 2005). With this technique, the first station becomes a virtual source for the seismic wave; therefore information about the actual source location is not needed. This gives ambient noise an advantage over traditional seismic methods involving ballistic waves generated from specific sources such as earthquakes or explosions (Shaprio & Campillo, 2004; Shapiro et al., 2005).

By correlating long time periods, the wave field becomes effectively random and the signal-to-noise ratio of the waveform representing the direct path taken between the two stations increases. The arrival time of the envelope of this prominent waveform represents the travel time of waves that propagate along the direct path, which can be used with the known interstation distance to calculate group velocity. Having a 2-D array of stations and cross-correlating all possible station pairs samples the subsurface repeatedly and provides a group velocity dataset than can then be used for tomographic inversion. In addition, the ambient noise wavefield is largely composed of surface seismic waves, i.e. Rayleigh and Love waves, which are dispersive. Therefore different frequencies have different depth sensitivities. Differences in depth sensitivity provide vertical resolution, which is necessary for obtaining vertical velocity profiles. Using this conceptual set-up, numerous studies have successfully used ambient seismic noise for regional and continental scale 2-D and 3-D tomographic inversions for crustal structure (Shapiro et al.,

2005; Sabra et al., 2005; Moschetti et al., 2007; Yang et al., 2007; Lin et al., 2008). However, recent studies have also been successful in exploiting later arrivals (coda) in ambient noise cross-correlations (CCs) for tracking temporal variations in subsurface velocity (Sens-Schonfelder & Wegler, 2006; Wegler & Sens-Schonfelder, 2007; Brenguier et al., 2008; Duputel et al., 2009; Mordet et al., 2010; Brenguier et al., 2011; Mainsant et al., 2012). Therefore, different portions of ambient noise CCs can be used to extract valuable information of the subsurface in the absence of an active source.

7.2 Basic Data Processing

We used almost two years of nearly continuous ambient noise records from the 7-station PALSIE array to construct daily cross-correlation functions. The python package MSNoise was used to pre-process and calculate the correlations. Table 4 displays the parameters used. We refer the reader to Bensen et al. 2007 and Lecocq et al. 2014 for more detailed information on the cross-correlation procedure. In addition to daily CCs, the MSNoise package allowed for moving window stacks of pre-specified numbers of days to be computed (Table 4). The correlations were then used for two separate multi-station ambient noise methods. The first method consisted of measuring the travel-time of the direct wave in order to construct group velocity dispersion curves to be inverted for 1-D shear velocity profiles. The main goal of this method was to assess if seasonal changes in the vertical velocity profiles resulting from winter versus summer dispersion curves could be retrieved. Detailed resolution of changes in active layer thickness was the main target, though shifts in permafrost depth range and thickness were also of interest. The second method employed was the Moving Window Cross-Spectral (MWCS) method using the python package MSNoise in order to construct semi-continuous time series depicting perturbations in subsurface velocity. The main goal of this method was to determine if ambient noise could be used for continuous monitoring of annual changes in active layer thickness as well as long-term degradation of permafrost resulting from climate change.

Table 4: Outline of parameters used in the cross-correlation and MWCS procedures. Modified from configuration table of MSNoise (Lecocq et al., 2014).

Cross-Correlation Parameters		
Value Used	Parameter Name	Description
ZZ	Component	Station components correlated Z = vertical, R = radial, T=transverse
86400	Analysis Duration	Total period of time each day to be analyzed (in seconds), i.e. 86400 means use the whole day
3600	Correlation Duration	Length of records being correlated at a time (in seconds), i.e. 3600 means hour-long records were correlated
4	Max Lag	Maximum time shift (in seconds) allowed during the cross-correlation process
3	Windsorizing	Temporal normalization method used for pre-processing. N times RMS, 0 disables windsorizing, -1 enables 1-bit normalization
True	Spectral Whitening	Flatten the spectrum of the time series being correlated by spectral whitening during pre-processing
60.0	Low Pass	Frequency (in Hz) at which to low pass filter records during pre-processing
10.0	High Pass	Frequency (in Hz) at which to high pass filter records during pre-processing
2,5,10,15,20,30,40,50	Move Stack	All options for number of days to be stacked using a moving time range
2013-09-01	Start Date	Date to begin the analysis process
2015-06-17	End Date	Date to end the analysis process
MWCS Parameters		
Value Used	Parameter Name	Description
Varied $10.5 < x < 55$	Fmin	Lower frequency (in Hz) limit defining the range in which MWCS is calculated
Varied $12 < x < 59.5$	Fmax	Higher frequency (in Hz) limit defining the range in which MWCS is calculated
Varied $1 < x < 3$ $t = x/f$	Window Length	Length (in seconds) of the moving window. Calculated based on variable number of cycles (x) and center frequency of band pass filter (f)
0.5* Window Length	Step Size	Length (in seconds) of the step size for the moving window
Jan Ref: 2014/01/01 – 2014/01/31 Year Ref: 2013/09/01 – 2014/09/01	Reference Stack	Time range used to create the reference stack.
0.7	R^2 threshold	Lower limit for acceptable R^2 values from the weighted linear regression of phase vs. frequency.
static	dtt lag	Determines how the lower lag time limit is defined. Static = constant time limit, e.g. 0.5 s. Dynamic = limit defined by constant velocity, e.g. 1 km/s
0.001	dtt v	Velocity (in km/s), if dtt lag = dynamic
0.2	dtt minlag	Lower lag time limit (in seconds) if dtt lag = static
3.8	dtt width	Length (in seconds) of full time lag range used
0.5	dtt maxerr	Maximum error allowed on dt measurements
0.8	dtt mincoh	Minimum coherence allowed on dt measurements
0.1	dtt maxdt	Maximum dt value accepted

7.3 Group-Velocity Dispersion Curves & Vertical Velocity Profiles

7.3.1 Method

The primary objective with respect to making measurements of group velocity was to determine if the GF resulting from correlations of ambient noise was seasonally affected. Changes from frozen ground in the winter to thawed ground in the summer results in a significant decrease in rigidity, which subsequently influences the velocity at which seismic waves propagate. Studies have documented reduced seismic velocities in thawed soil compared to frozen (Barnes, 1966; Zimmerman & King, 1986; Kneisel et al., 2008). Therefore, we hypothesized that the seasonal thawing of the active layer should be observable through a decrease in seismic velocity in summer compared to winter. The vertical transition between frozen and thawed soil at the permafrost table was expected to result in a velocity drop at a specific frequency range corresponding to waves most sensitive to the active layer. Thus, by utilizing the dispersive nature of surface waves it was hoped that the specific thickness of the active layer could be obtained.

The two active layer thickness surveys (see Figure 15 & Figure 16) conducted in early summer show that the permafrost table occurs at less than ~0.75 m depth for most of the array area, with the exception of the northwest corner. The dispersive nature of surface waves, in which higher frequencies are sensitive to shallow structure while lower frequencies sample deeper structure, dictates that the highest frequencies obtained should be the most sensitive to the active layer. However, the upper frequency limit of the experiment was limited by the sampling rate of the sensors, which was either 125 or 200 samples per sec (sps), depending on the station and time during the deployment period. During pre-processing all records were resampled to 125 sps and low pass filtered at 60 Hz. To determine if the ambient noise CCs recorded the thawing of the active layer, winter and summer stacks were made for every station pair. The sum of all daily CCs in the months of December, January, and February constituted the winter stacks for each station pair, while summer stacks were the sum of all daily CCs in the months of August, September, and October. It should be noted that due to the "thermal offset" between the ground surface temperature and ground temperature in the active layer, the maximum active layer thaw occurs at a lag behind peak ground surface temperatures (Burn & Smith, 1988; Romanovsky & Osterkamp, 1995; Jorgenson et al., 2010). The winter and summer CCs for each station pair were

filtered at a variety of frequency bands. The envelopes of the filtered CCs were normalized and assembled into frequency-time plots from which group velocity measurements were made. Winter and summer group velocity measurements were averaged over all station pairs to create a winter and summer network average dispersion curve. Computer Programs in Seismology (CPS) was used to invert through iteration the winter and summer dispersion curves (Herrmann & Ammon, 2002). This produced a summer and winter vertical velocity profile.

7.3.2 Results

Figure 5 shows example summer and winter CC stacks filtered at three different frequency bands for station pair R1B-R2A. At low frequencies (Figure 29A) the summer and winter CCs are very similar and produce the same group velocity. At a mid-high frequency range (Figure 29B) the summer signal-to-noise ratio (SNR) is lower compared to the winter and the summer group velocity is significantly slower. Finally, at high frequencies (Figure 29C) the summer arrival is even slower still and the SNR remains lower compared to winter. The winter group velocity remains static between all three frequency bands. Frequency bandwidth had a large effect on the frequency-time plots and subsequent group velocity measurements.

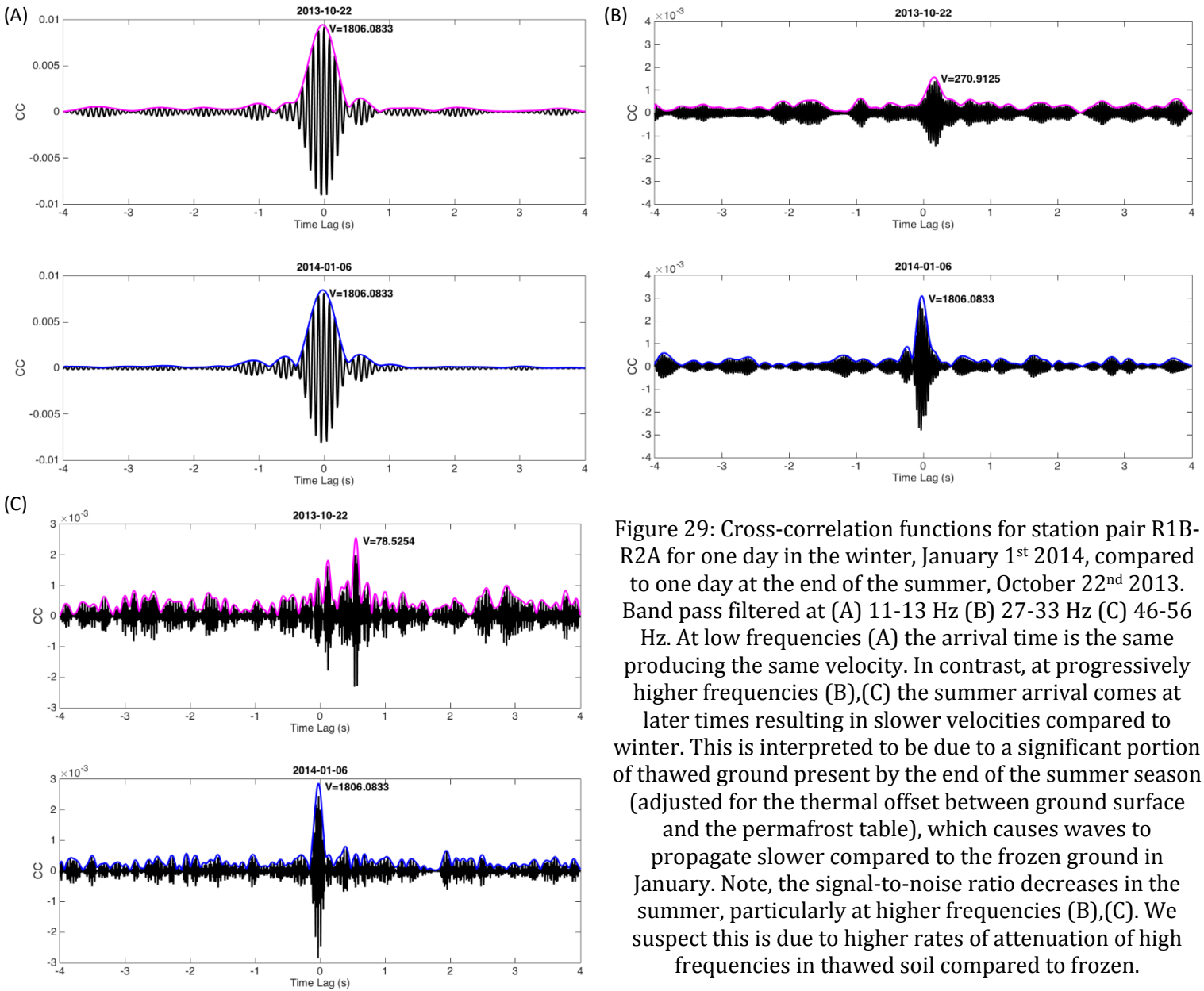

Figure 29: Cross-correlation functions for station pair R1B-R2A for one day in the winter, January 1st 2014, compared to one day at the end of the summer, October 22nd 2013. Band pass filtered at (A) 11-13 Hz (B) 27-33 Hz (C) 46-56 Hz. At low frequencies (A) the arrival time is the same producing the same velocity. In contrast, at progressively higher frequencies (B),(C) the summer arrival comes at later times resulting in slower velocities compared to winter. This is interpreted to be due to a significant portion of thawed ground present by the end of the summer season (adjusted for the thermal offset between ground surface and the permafrost table), which causes waves to propagate slower compared to the frozen ground in January. Note, the signal-to-noise ratio decreases in the summer, particularly at higher frequencies (B),(C). We suspect this is due to higher rates of attenuation of high frequencies in thawed soil compared to frozen.

If bands are kept at a constant, narrow width of 2 Hz (Figure 30A-D) the filtered waveforms are wide in time. This is due to the trade-off between the frequency and time domains. To be localized in the frequency domain results in less localization in the time domain, i.e. wider waveforms. In contrast, when the bands are kept at a constant width of 8 Hz (Figure 30E-H) the filtered waveforms are narrow in time. Thus, to be localized in the time domain results in less localization in the frequency domain. This is observed in the large degree of smoothing between frequency bands seen in Figure 6E-H compared to Figure 6A-D.

To optimize the frequency-time tradeoff, a dynamic filtering scheme was adopted where bandwidth was scaled to 10% of the center frequency (Figure 31). Another complication encountered was the prominence of multiple waveforms in the CCs. Stacking longer time periods helps to stabilize the CCs and typically results in the strong emergence of the direct arrival since that path is the shortest and most common compared to random scattered paths. However, even after stacking an average of 90 winter days and 85 summer days persistent arrivals continued to stack positively resulting in multiple prominent waveforms. The maximum amplitude peak could not be assumed to be the direct arrival. Therefore measurements were made manually by plotting frequency-time images and tracking the waveform that smoothly migrated with frequency (Figure 31).

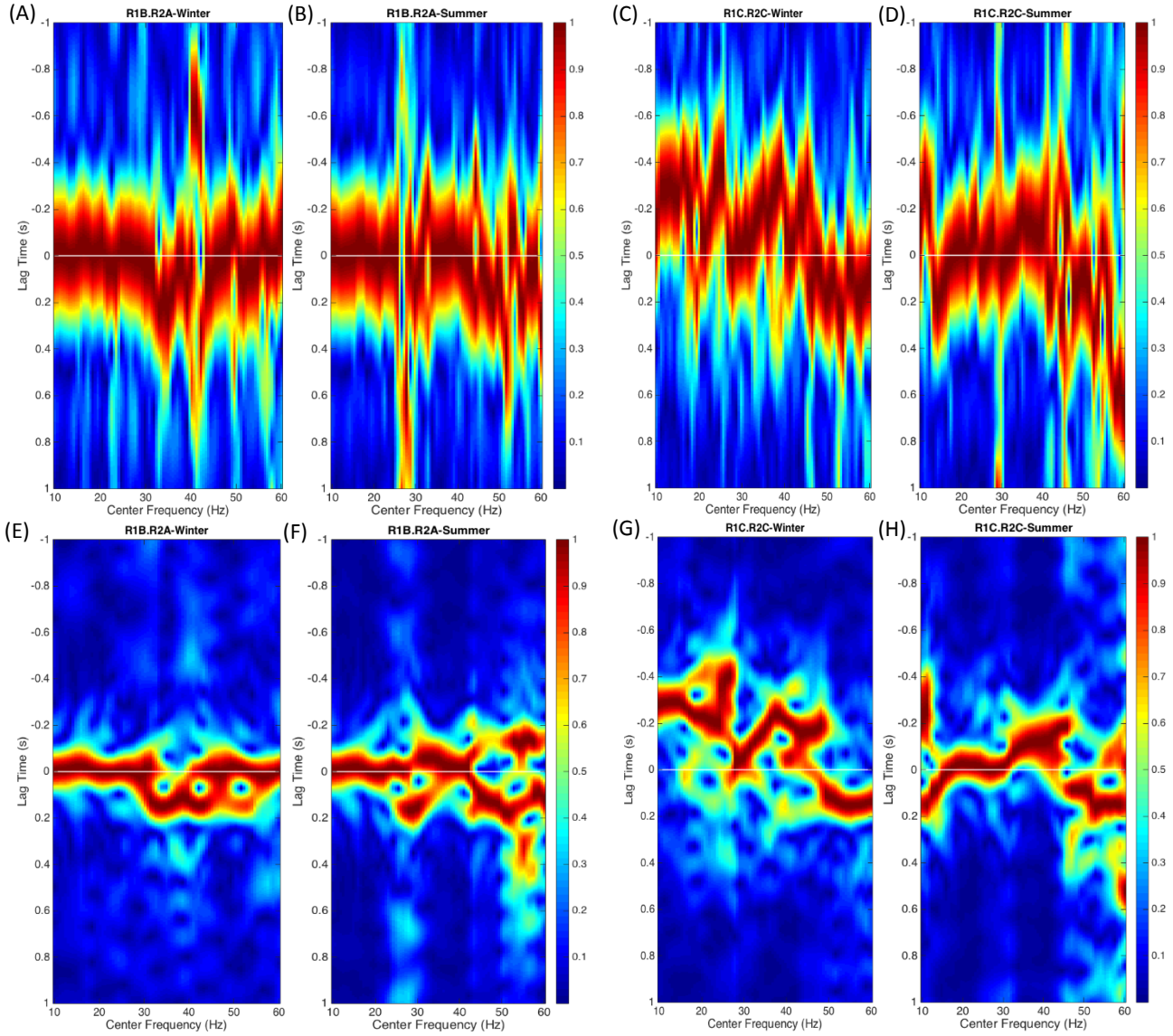

Figure 30: The summer and winter CCs for station pairs R1B-R2A (A,B,E,F) and R1C.R2C (C,D,G,H) were filtered at constant 2 Hz bands (A-D) and 8 Hz bands (E-H). The envelopes of the filtered waveforms were normalized and assembled into the frequency-time color plots where red represents the maximum amplitude. The trade-off between localization in time versus frequency was apparent and made frequency band selection difficult. When bands are kept at a constant width of 2 Hz, waveforms are much wider in time and more variability between adjacent frequencies is seen (A-D). When bands are kept at a constant width of 8 Hz, waveforms are much narrower in time and variations with frequency are much smoother. Since measurements are made at the peak of waveform envelopes the width in time was important in establishing uncertainty. Note that the station pairs have the same interstation distance.

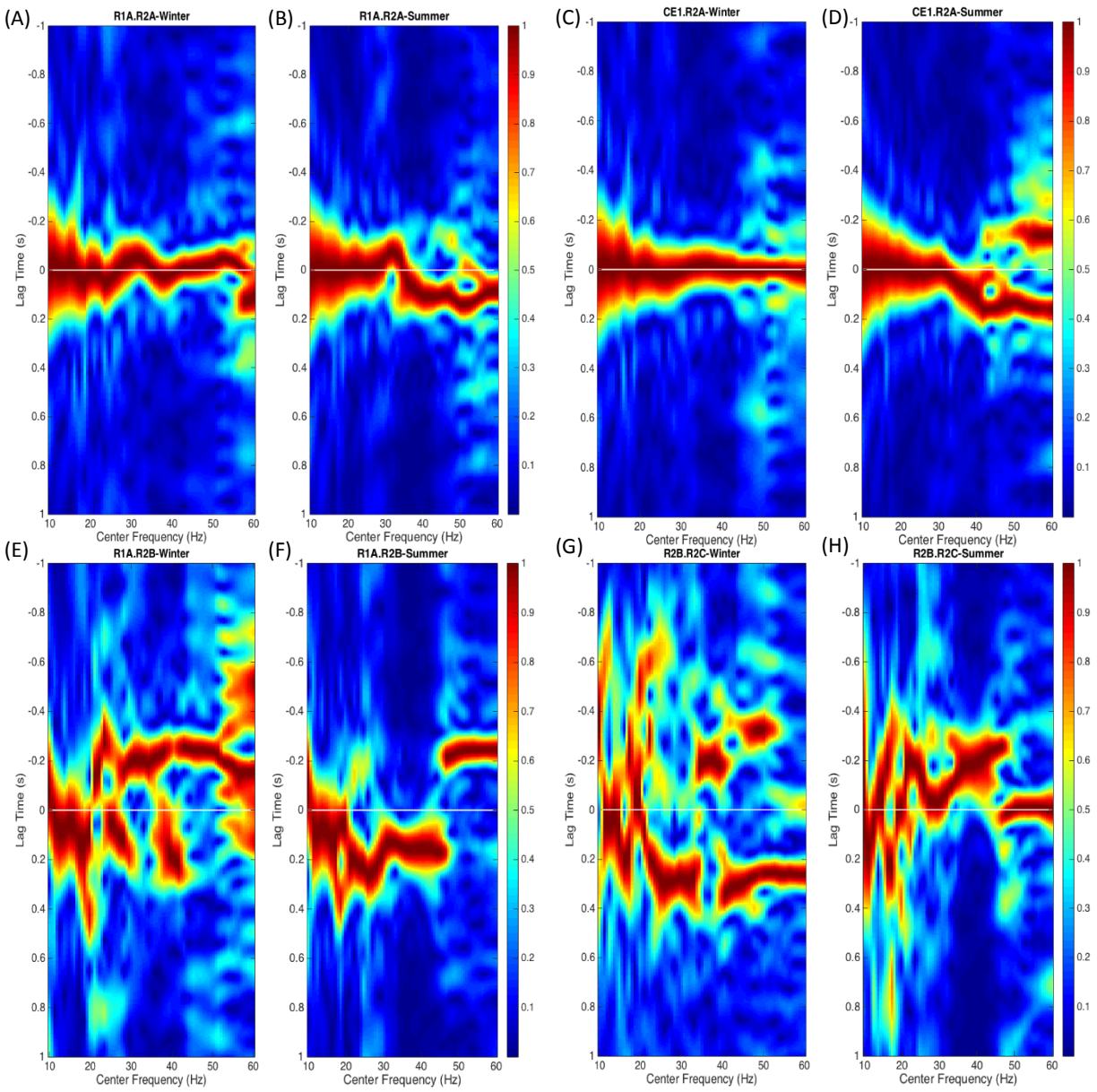

Figure 31: To optimize the trade-off between frequency and time localization, frequency bands were scaled to 10% of the center frequency. Travel-time measurements were made by selecting the time corresponding to the peak of the direct arrival. Selection of the correct peak was made difficult due to the presence of multiple arrivals, as shown in these plots for 4 different station pairs (A-H). For example, the winter plot of station pair R2B-R2C (G) shows a clear trend in the maximum peak (red). The summer plot (H) shows a distinct jump in arrival time of the maximum peak starting at ~48 Hz to near infinite velocities. Selection of the accurate GF arrival time was made by following the migration trend of the maximum, which led to a series of secondary peaks at around -0.35 seconds. Differences between winter and summer can be observed, particularly at high frequencies. For example, station pair R1A-R2B shows the maximum arrival of high frequencies (50-60 Hz) occurring at a smaller lag time in winter compared to summer. At lower frequencies the velocities the winter and summer arrival times are similar. We note that switches between causal and acausal arrivals between winter and summer indicates changes in source locations.

The network average winter and summer dispersion curves show similar velocities at frequencies below ~35 Hz (Figure 32). At higher frequencies a clear separation between the dispersion curves is observed, where the winter dispersion curve has consistently faster group velocities compared to summer. The inversion results of the winter and summer dispersion curves show similar velocity structure below 6 meters depth (Figure 33). Above 6 m depth the winter velocity profile shows constant fast velocities within the range normal for frozen silt and organic rich soil (Barnes, 1966). The summer velocity profile shows slow velocities that gradual increase to 6 m depth. The depth sensitivity kernels produced by CPS show that the upper frequencies of the dataset have high sensitivity above ~5-6 m depth, however the sensitivities are the same in that depth range (Figure 34A). This indicates that vertical resolution of the dataset is not sufficient to detect the specific thickness of the active layer. However, as seen in Figure 33B, the slower velocities of the summer dispersion curve still produce a slow velocity zone at the shallowest depths. Figure 34 A,B both show the maximum depth sensitivity of the dataset diminishes below ~24 meters depth.

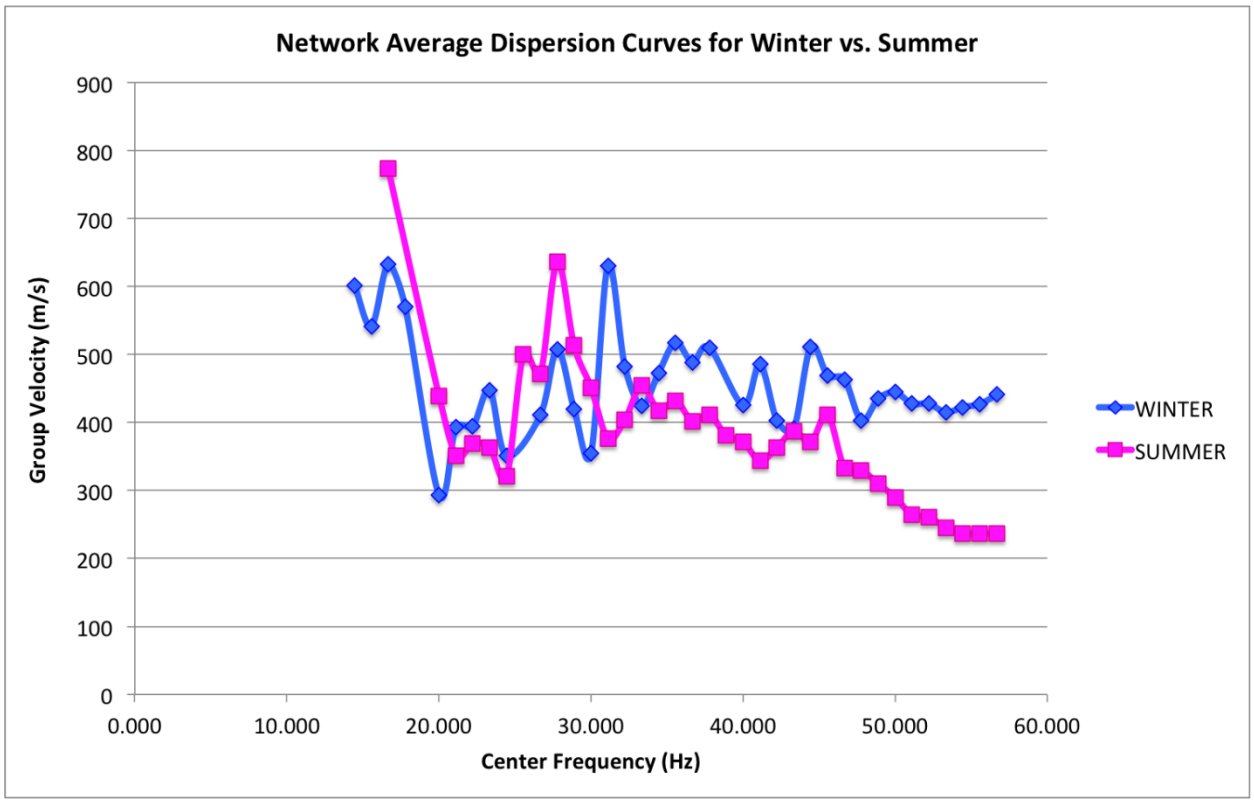

Figure 32: Network average dispersion curves for winter and summer. Note that the higher frequencies (> 35 Hz) show the most separation between winter and summer and are also better resolved compared to lower frequencies, which show more scattered.

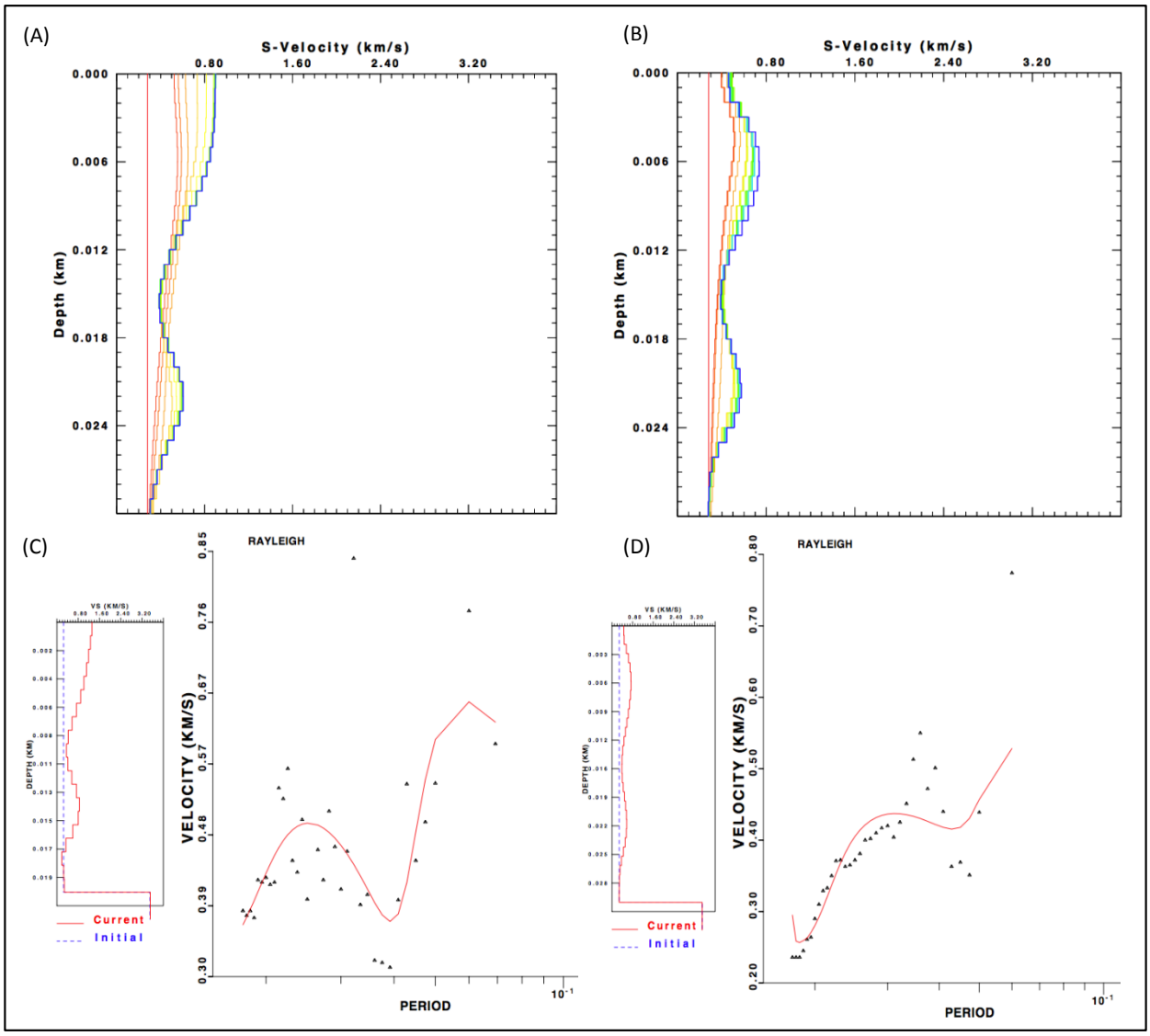

Figure 33: Results from iterative inversion using Computer Programs in Seismology (Herrmann & Ammon, 2002). Both winter and summer inversions start with the same constant velocity initial model (red in (A),(B), blue in (C),(D)) (A) The final shear velocity profile (blue) resulting from the network average winter dispersion (C) shows fast velocities from the surface down to 6 m depth followed by a gradual decrease to 15 m and subsequent increase to 22 m depth. (B) The final shear velocity profile (blue) resulting from the network average summer dispersion (D) shows slow velocities near the surface that increase down to 6 m depth followed by a decrease and increase matching that seen in the winter model. Both models navigate back toward the starting model below 24 meters depth, which is consistent with the maximum depth sensitivity seen in Figure 34.

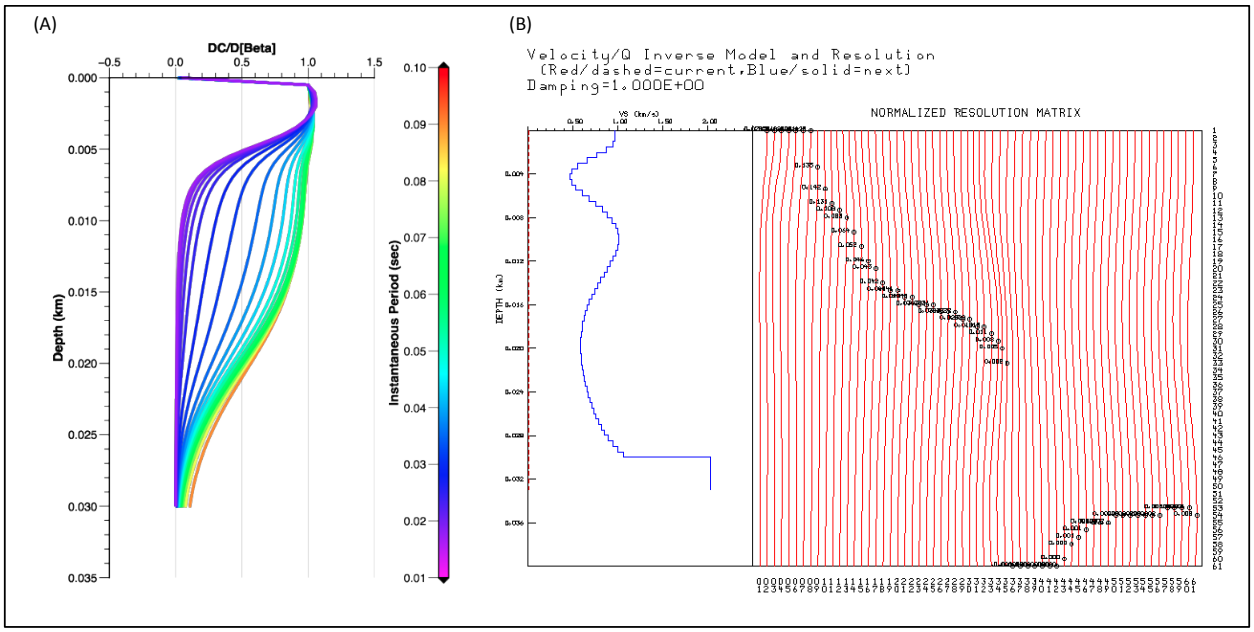

Figure 34: (A) Depth sensitivity kernels for frequencies in the range of 10-60 Hz (0.016 – 0.1 s). The highest frequencies have the same sensitivity for the top ~5 meters, which means there is no vertical resolution for velocity changes above that depth. In terms of resolving the active layer thickness, this means our frequency range is not high enough to discern the specific depth at which the active layer ends. However, sensitivity is still high above 5 meters so overall changes in that range should still be recorded. (B) Shear wave model and associated resolution matrix. The resolution matrix shows the top 7 layers co-vary together, this supports the sensitivity kernels in that there is no resolution within the uppermost layers. Both (A) and (B) also show that the 10-60 Hz frequency range is not sensitive to structure below ~25 m depth.

7.3.3 Discussion

The successful cross-correlation of ambient seismic noise in the 10-60 Hz frequency range is itself an exciting outcome as shallow environmental applications of this method are still rare within published literature. The application of this method for permafrost investigations is novel, which unavoidably comes with complications not encountered in traditional ambient noise studies. In particular, the presence of multiple strong arrivals in the CCs produces an unforeseen difficulty in making group velocity measurements. A working theory for the cause of this problem is that it is due to the small station spacings of the experiment. Waveforms that increase in amplitude with stacking are those that occur persistently. In traditional applications, station pairs are separated multiple kilometers apart. Therefore scattered waves, which travel even further distances, occur much less frequently compared to the direct path so that stacking CCs only increases the amplitude of the direct arrival. For this dataset, the stations were separated tens of meters apart in a zone of discontinuous permafrost. The possible presence of talik zones

and pockets of permafrost would likely serve as strong scatterers. Persistent scatterers would cause waves to arrive at similar lag times consistently with time leading to the large amplitudes in the correlations when long time periods are stacked. The farther the travel path of the scattered wave the more it is affected by attenuation and other scatterers due to heterogeneity. Therefore it is possible the short station distances of this experiment allow for persistently scattered waves to reach the recievers more consistently than they would at farther distances. This theory would largely explain waves arriving after the direct arrival. Waveforms that arrive before the direct arrival could be due to the presence of higher mode Rayleigh waves, or possibly even body wave arrivals (Forghani & Snieder, 2010).

Also, the problem of prominent waves forms commonly centered at or very near zero time lag is interpreted to be due to a combination of factors. Firstly, the short travel-times of the direct waves put the arrivals near zero. However, the width of the waveform arriving commonly spans a wider time range than its arrival, particularly at low frequencies, leading to overlap into negative time. The overlap of the causal and acausal arrival could lead to the combined waveform having a peak centered at zero. Secondly, Fan & Snieder (2009) demonstrate that spurious fluctuations centered at zero can occur in ambient noise correlations when the number of sources is low (< 40). Thus a minimum number of sources is needed. Lastly, point sources located along the line perpendicular to the direct path between the station pairs could produce a wavefront that travels outwards and is recorded simultaneously at both stations. When correlating the station records, the point source wave would correlate most strongly at zero time offset.

The results of comparing winter and summer CCs and group velocity dispersion curves show that ambient seismic noise does detect seasonal differences in subsurface velocity. The significantly lower seismic velocity of the thin active layer was sufficient enough to result in slower travel times for the direct arrival in summer compared to winter (Figure 32 and Figure 33). However, the upper frequency limit of the dataset was not high enough to have vertical resolution above ~5 meters depth (Figure 34). Therefore, this dataset was unable to resolve the specific thickness of the active layer but was still sensitive to the velocity change. We suspect this is why the shear velocity model in Figure 33 has a gradual increase in velocity above ~6 m rather than the idealized model of a slow top one meter layer followed by a sharp velocity jump.

7.3.4 Future Work

The findings from this portion of the PALSIE project leave open a number of lines of further investigation. The following future work will be completed by PhD. candidate Stephanie James, at the University of Florida, as part of her dissertation:

- Write script to conduct more rigorous group velocity measurement using Frequency-Time Analysis (FTAN) as described by Levshin et al. (1972). The complication of multiple arrivals led to uncertainty in group velocity measurements. FTAN includes an additional step to reduce contamination from higher mode waves and create measurements based on assumptions of smoothly varying dispersion curves.
- Write script to loop through 30 day moving stacks, run newly completed FTAN script and CPS inversion on resulting dispersion curves with the goal of isolating the timing and duration of the active layer thawing and freeze-up.
- Group station pairs by similar characteristics and investigate for spatial differences in dispersion and vertical velocity models.
- Create CPS sensitivity kernels for synthetic dispersion curves of frequencies higher than 60 Hz to identify the frequency range needed for resolving the active layer thickness.
- Run Markov Chain Monte Carlo (MCMC) inversions on representative group velocity dispersion curves (winter, winter-summer transition, summer, summer-winter transition) as alternate inversion method to the iterative method in CPS. The CPS iterative inversion is highly dependent on the starting model and is restricted to a specific number of layers with fixed interfaces. A trans-dimensional MCMC algorithm is not dependent on initial models and would allow inversion for interface depths along with layer velocities.

7.4 Temporal Variation

7.4.1 Method

The use of scattered seismic waves to monitor velocity changes of the subsurface was first proposed in the 1980s through analysis of seismic coda waves (Poupinet et al., 1984). This technique was later named Coda Wave Interferometry (CWI) (Snieder et al., 2002; Snieder,

2006). However, CWI relies on repetition of active sources, e.g. earthquakes, which can thereby result in discontinuous monitoring (Sens-Schonfelder & Wegler, 2006; Hadziioannou et al., 2009). Recent studies have sought the advantages of ambient seismic noise for use in monitoring applications, through a technique named Passive image interferometry (PII). PII combines the basic procedure of ambient noise cross-correlation with CWI to return measurements of temporal variations in seismic velocities of multiply scattered waves (Sens-Schonfelder & Wegler, 2006; Brenguier et al., 2008; Hadziioannou et al., 2009; Sens-Schonfelder & Wegler, 2011). PII has proven effective for a variety of applications such as detection of magma movement and changes in a volcanic edifice prior to eruption (Brenguier et al., 2008; Duputel et al., 2009; Mordet et al., 2010; Brenguier et al., 2011), co-seismic changes in fault-zone stress field (Wegler & Sens-Schonfelder, 2007), landslide prediction (Mainsant et al., 2012), and seasonal variations in hydrologic conditions (Sens-Schonfelder & Wegler, 2006).

In this study we tested the use of PII for measuring changes in the active layer thickness of permafrost. This method utilizes the late arrivals of the cross-correlations. The late arrivals are the result of scattered waves that travel longer paths through the medium compared to the direct arrival. Therefore, these scattered waves will be more sensitive to homogeneous velocity changes (Clark et al. 2011; Mikesell et al. 2015). This method is conducted by measuring changes in phase between a reference CC, (CC_{ref}), and the current CC, (CC_{cur}). The reference is meant to represent average background conditions while the current trace represents the velocity condition at a specific point in time. The amount of phase change between CC_{cur} and CC_{ref} can be measured and used to calculate the relative change in velocity from the background condition to the current point in time. We used the Python package MSNoise of Lecocq et al. 2014 to calculate the relative velocity changes. MSNoise uses the PII method called Moving Window Cross-Spectrum (MWCS) analysis.

In MWCS analysis, the first step is to take windowed segments of CC_{cur} and CC_{ref} and find their Fourier transforms, $F_{cur}(\upsilon)$ and $F_{ref}(\upsilon)$, respectively (Clarke et al. 2011). The cross-spectrum function, $X(\upsilon)$, of $F_{cur}(\upsilon)$ and $F_{ref}(\upsilon)$ is found in the frequency domain as follows:

$$X(\upsilon) = F_{ref}(\upsilon) \bullet F^{*}_{cur}(\upsilon) = |X(\upsilon)|e^{i\phi(\upsilon)}$$

where υ is frequency in Hz, * denotes the complex conjugate, |X(υ)| is the amplitude of the cross-spectrum and ϕ(υ) is the phase of the cross-spectrum. A weighted linear regression of the cross-spectrum phase is used to get the slope of a line that best fits phase changes with frequency, weighted by the coherence between CC_{cur} and CC_{ref}. Points where the two time-series have low coherence will count less in the linear regression compared to points that have high coherence (Figure 35A). A quality control step was added to the MSNoise algorithm in order to reject all δt values for windows with an R^2 from the linear regression of less than 0.7 (Figure 35B). The slope, m, of the best fit line is related by a factor of 2π to the time shift, δt, between the two time series for j=l,...,h. within the frequency range defined:

$$\phi_j = m \bullet \upsilon_j, \quad m = 2\pi\delta t$$

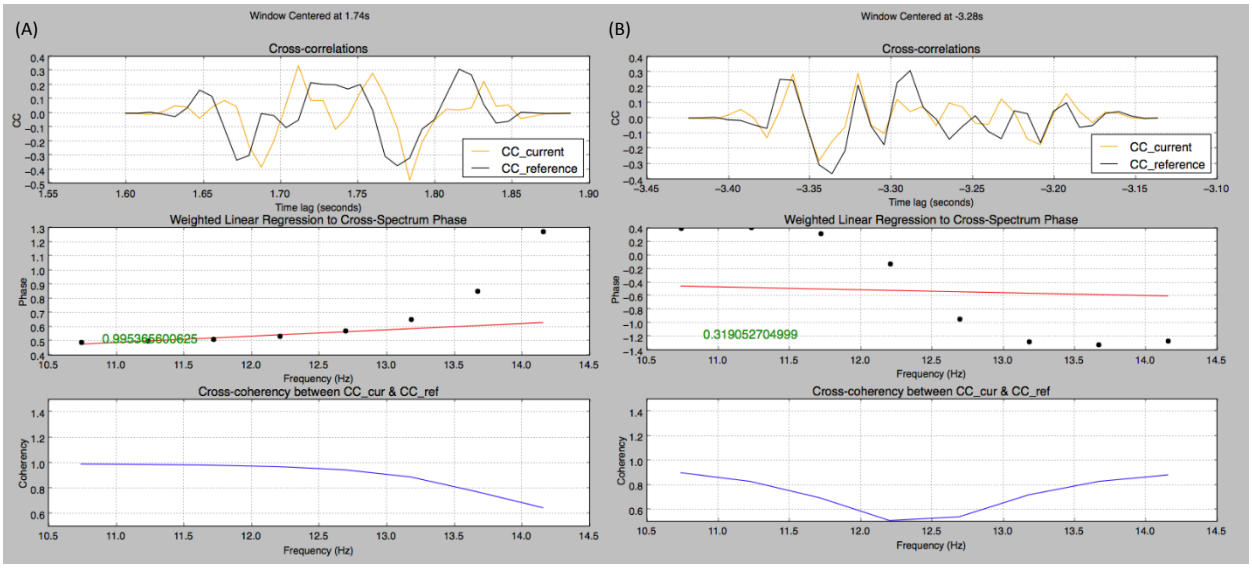

Figure 35: Examples of the weighted linear regression conducted as part of the MWCS analysis of MSNoise are shown for two different time windows for a 30-day stack from the station pair R2B-R2C. Time windows are 0.3 seconds long and the frequency range defined was 10.5-14.5 Hz. (A) The weighted linear regression produces a good fit (red line) with a high R^2 value (green) to the phase data when coherence is near 1 (< 13 Hz). (B) In this window, the weighted linear regression produces a poor fit as a result of low coherence as well as the constraint that the line intersects the origin (zero phase at zero frequency). The R^2 metric was identified as a possible quality control parameter in the analysis. Therefore, only δt values for windows with an $R^2 > 0.7$ were kept for the δv/v calculation.

Time shift measurements are made for a series of overlapping windows moving through the CC functions. For a homogeneous velocity perturbation, δv/v, the resulting time shift will approximately be the opposite:

$$\delta v/v = -\delta t/t$$

Therefore, a second linear regression is done to the δt measurements at different lag times, as defined by the center time of the moving window for which the δt measurement was made. The slope of the best fit line is the relative velocity change between CC_{cur} and CC_{ref}. A sequence of selection parameters is defined to improve the quality and accuracy of the results (Table 4) (Lecocq et al. 2014). The window length and frequency range defined are important parameters in this method. We chose to conduct MWCS analysis over a series of narrow frequency bands. The window length was scaled by the center frequency of the band such that the length spanned a specified number of cycles, between 1 and 3 (Table 4).

In the MWCS method it is assumed that one trace is a time-shifted version of the other (Mikesell et al. 2015). This assumption can introduce error as it allows for cycle skipping, which occurs when the incorrect waveforms are correlated between the CC_{ref} and CC_{cur}. Cycle skipping can occur for a variety of reasons. To start, if the SNR of the late arrivals are too low the noise can result in the wrong waveforms being compared. Secondly, if the analysis window is too short or if the δt is larger than the dominant period, then the two windowed time segments may not contain the same arrivals. Furthermore, cycle skipping can occur if differences between the reference and the current condition are so large that the particular scattered arrival is no longer present (Mikesell et al. 2015). The change from frozen (Vs ≈ 1000 m/s) to thawed ground (Vs ≈ 100 m/s) can be as much as a 90% change in subsurface velocity. Therefore, it is suspected that cycle skipping will occur when the MWCS analysis, as it is currently employed by MSNoise, is applied to this dataset. This problem is addressed in further detail in the Discussion section below.

A continuous record of relative velocity changes can be calculated when all available days are compared to the reference. However, there is a trade-off between CC stability and time resolution. Single-day CCs prove very noisy and highly variable, therefore stacking multiple days together improves the stability of CC_{cur} and the reliability of the δv measurement made.

However, as more days are stacked the resolution in time decreases (Lecocq et al., 2014). To combat this tradeoff, MWCS analysis was done on moving stacks of a variable number of days (N = 2,5,10,15,20,30, and 40).

Since the large change in velocity between winter and summer is expected to be isolated to the active layer, the largest δv/v values are likely isolated to a specific frequency range most sensitive to that layer. Therefore, by conducting the MWCS analysis over a range of frequency bands, the frequencies most sensitive to the active layer should have significantly larger decreases in relative velocity in the summer compared to lower frequencies. In this way, we should be able to target the ideal frequency range in which to monitor for seasonal changes in the active layer. Additionally, δv/v changes at lower frequencies not sensitive to the active layer can be useful in assessing larger scale degradation, or possibly expansion, of permafrost within the study site.

7.4.2 Results

Relative velocity changes were calculated for all station pairs for a variety of parameters (Table 4). Results were highly sensitive to the window length and frequency range defined (Figure 35, Figure 36, and Figure 37). We found that a minimum of 3 cycles was needed to produce suitable measurements. High variability in the cross-spectrum phase, even within narrow frequency bands, led to poor fits in the linear regression (Figure 35). When the unwrapped phase of the cross-spectrum was viewed for the entire frequency band of the dataset, large oscillations in phase where observed (Figure 37). Also, the constraint of the regression to have the predicted line intersect the origin (zero phase at zero frequency) led to poor fits when the cross-spectrum contained large phase values that would necessitate a y-intercept other than zero. Therefore, an additional quality control parameter was added to the MSNoise procedure in order to reject all delay times where the R^2 of the regression was below a specified threshold.

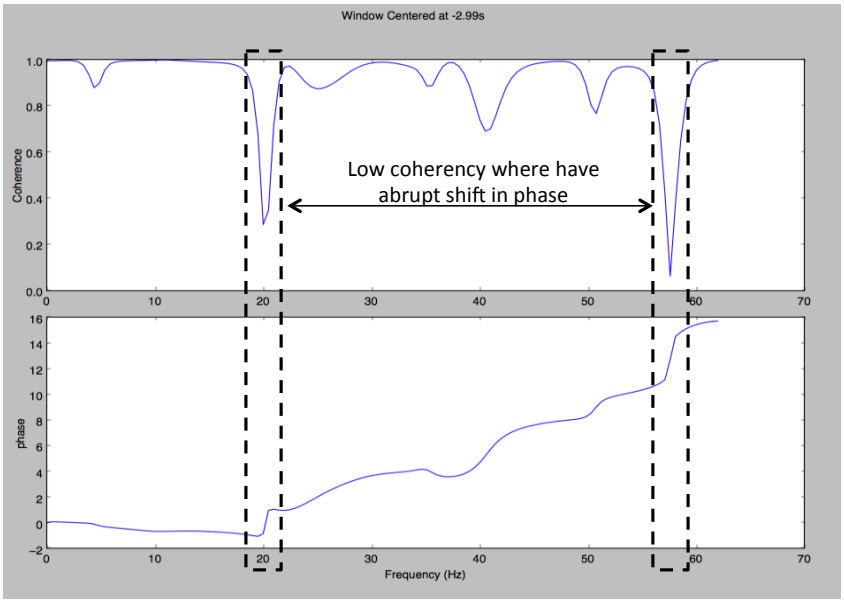

Figure 36: Example of phase change across the entire frequency band of the dataset (10-60 Hz). A relationship is observed between the coherence of the two time series and the change in slope of the phase plot. When there is an abrupt change in phase there is a drop in coherence. Conversely, when the slope stays constant with frequency the coherence stays more or less stable

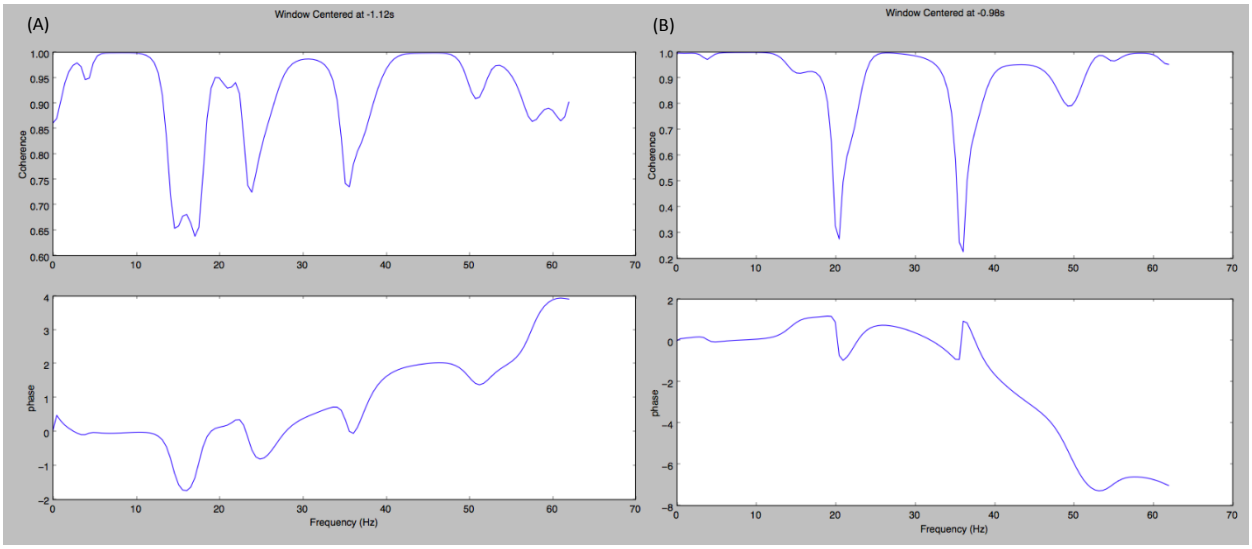

Figure 37: The high degree of variability in phase across the entire frequency band of the dataset (10-60 Hz) is shown for two adjacent time windows (A) and (B) within the same 30-day stack for the station pair R2B-R2C. The abrupt changes in phase are not consistent between windows meaning the two windows have high coherence in different frequency bands. The unpredictability of the cross-spectrum phase with frequency prohibits selection of only frequency bands with high coherence. Also, the general trend in phase is positive in (A) but negative in (B). Therefore, the window in (A) would generally produce a $+\delta t$ and $-\delta v$ while the window in (B) would produce a $-\delta t$ and $+\delta v$. Since the slope of the cross-spectrum phase leads directly to the $\delta t/t$ estimates, which subsequently determines the $\delta v/v$, the high degree of variability in phase with frequency leads to large variability in $\delta v/v$ estimates and ultimately lower accuracy.

The sensitivity of the reference stack was also investigated. The month of January is considered the most stable time period of the year. Therefore, with the reference stack as the month of January 2014, the resulting relative velocity changes represent deviations from the stable "background" condition of fully frozen ground (Figure 38). An alternate case was tested where the reference was made to be the yearly average (Figure 39). In general, the results from both reference cases show variability in δv/v decrease with increasing number of days stacked. Larger amplitude fluctuations are seen within the late summer months of 2014 (August through October), which then return to stable conditions within the winter of 2014-2015. It is important to note that due to gaps in data availability, the actual number of days included in the moving window stacks vary. To visualize this, the time axis in Figure 39 is aligned for all δv/v plots and the data availability plot. The δv/v plot for the 30-day moving window stacks in Figure 15 extends beyond the range of the data available. This is because the 30-day stacks are the summation of all available CCs for the last 30-day period. For this station pair, the available data ends at the beginning of March 2015. Therefore the positive spike in δv/v seen in the 2 day stack gets dragged out to the end of March 2015, as the 30 day stack at that time would simply include the stack of the final CCs from the beginning of March.

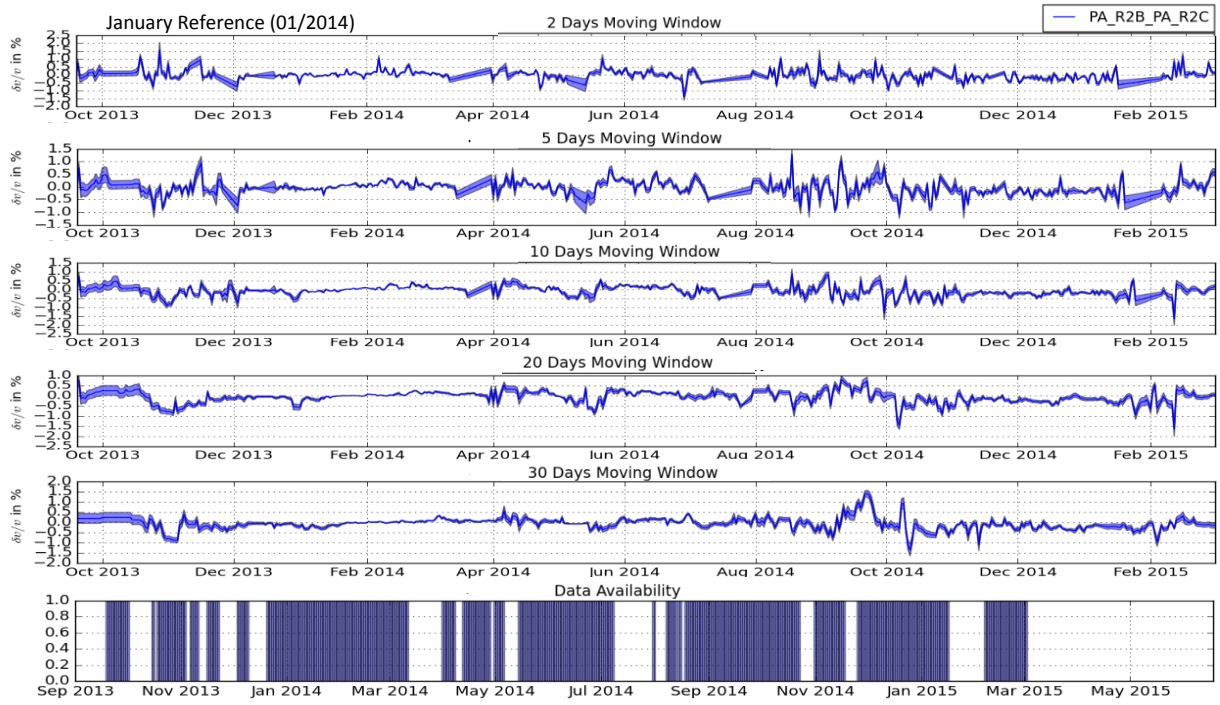

Figure 38: Results of MWCS analysis for the station pair R2B-R2C within the frequency range 10.5 – 14.5 Hz using the month of January 2014 as the reference. The fully frozen ground in January provides a stable baseline from which deviations can be measured.

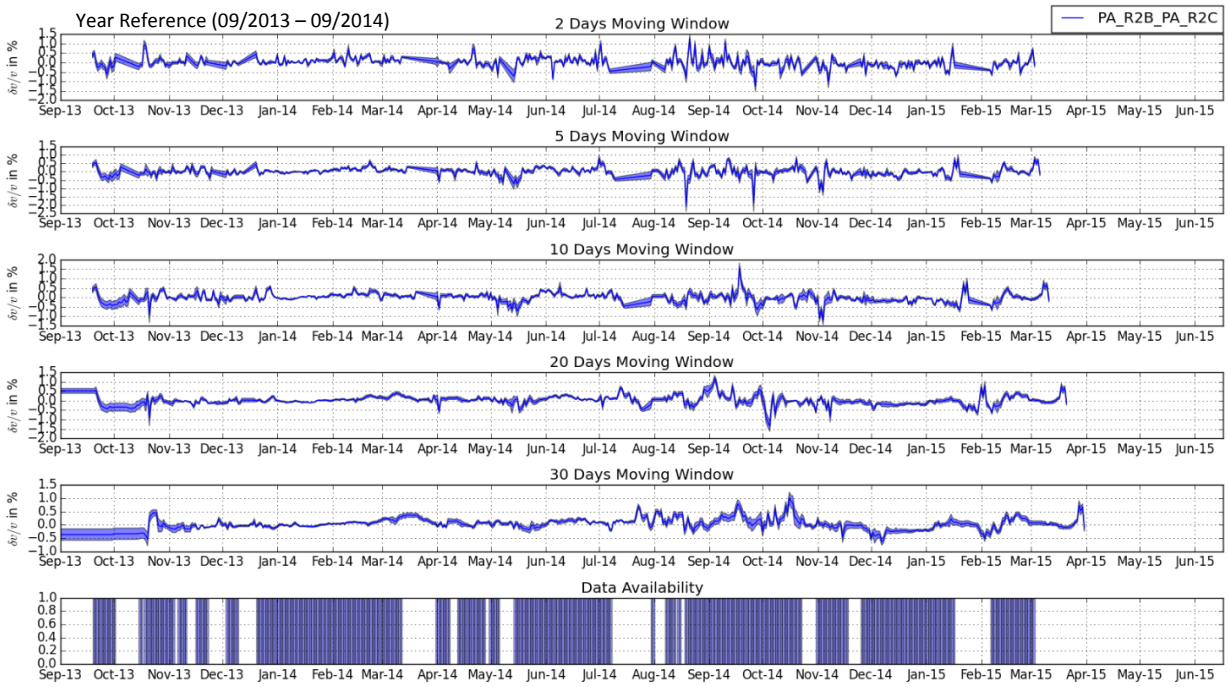

Figure 39: Results of MWCS analysis for the station pair R2B-R2C within the frequency range 10.5 – 14.5 Hz using the first year of data as the reference. Stacking all days over a year effectively averages the CC functions. Therefore, the δv/v measurements were made compared to the yearly average CC.

7.4.3 Discussion

Initial results from the MWCS analysis using the procedure defined by MSNoise are promising. A general trend is observed of more stable, lower amplitude δv/v variations in winter followed by high amplitude variability in summer, regardless of the reference stack (January versus yearly average). Overall, both reference choices produce the same large-scale features, but finer scale differences can be observed. However, by itself the yearly average CC is not meaningful as it is the average of large fluctuations between two end-member conditions, i.e. summer/thawed, winter/frozen. Therefore since the yearly average was not significantly different from the January stack, the month of January is concluded to be a better, more meaningful reference as the migration in δv/v can be tracked from the frozen to the thawed condition and back again.

An interesting outcome is the lack of a clear pattern of negative δv/v values in summer and positive δv/v values in winter. The summer months show both faster and slower velocities compared to the reference, which in the case of a January reference, is unexpected. There are a

couple possible explanations for this. First, the system could be more dynamic and complex than the simple transition from frozen to thawed ground as assumed. For example, the presence of groundwater in the thawed soil of summer and potentially saturating talik zones could result in a faster velocity compared to an unsaturated talik zone in winter. The percentage of ground ice within the permafrost could also be variable. Also, the spatial continuity of the permafrost and possible presence of talik zones at the study site is unknown. A second explanation is that cycle skipping within the MWCS analysis as employed by MSNoise produces inaccurate measurements. Both of these considerations are likely true.

To start addressing these concerns, it is best to first verify that the method used is appropriate for the objective of this project. The issue of possible cycle skipping was discussed in a recent publication by Mikesell et al. 2015 in which the authors compared the MWCS technique with an existing stretching technique and a new dynamic time warping technique (DTW) developed by the authors. Mikesell et al. 2015 demonstrated that cycle skipping was common for the MWCS technique, particularly for window lengths of less than 5 cycles. The stretching technique performed better, but has an additional drawback with regards to spurious velocity changes resulting from changes in the source frequency spectrum (Zhan et al. 2013; Mikesell et al. 2015). Overall the newly developed DTW technique was found to be more immune to cycle skipping and produced more accurate results.

Upon further consideration, it is our conclusion that the MWCS analysis of MSNoise can be altered to suit this project. The problem of cycle skipping is thought to occur when the velocity changes between winter and summer produces a time shift larger than the window size of the analysis, thereby prohibiting phase comparison of the same scattered arrival. However, window lengths cannot simply be made very large, as that would limit the number of δt measurements used in the linear regression solving for $\delta v/v$, while having multiple smaller windows increases the number of data points and subsequently the robustness of the regression (Clark et al. 2011). The MWCS method has previously been employed for very small (<1 %) $\delta v/v$ changes within typically narrow frequency bands. Therefore, the application of this technique to large ($\leq$ 90%) $\delta v/v$ changes across a wide frequency range (10-60 Hz) requires further customization. It is assumed that daily changes in velocity are small, and gradually over a

season the velocity changes become much larger. A cumulative dt scheme can be used where small time shifts are tracked from day to day and dictate the boundaries of the moving windows within CC_{cur} for each subsequent day. In this way, the window lengths may remain a suitable size, e.g. 3-10 cycles, and the arrival time of the correct wave can be tracked through time so that the phase of the proper waveforms are compared. In other words, the boundaries for the windows of the reference trace and the current days trace will vary.

7.4.4 Future Work

Overall, the findings from this portion of the PALSIE project indicate that monitoring velocity changes using ambient seismic noise is a promising new technique for permafrost studies. However, application of this method to the unique setting and characteristics of the Poker Flat dataset have led to complications not previously encountered in the seismic literature. Therefore customized procedures need to be developed. The following future work will be completed by PhD. candidate Stephanie James, at the University of Florida, as part of her dissertation:

- Alter the MSNoise source code to use the new scheme for tracking phase changes without cycle skipping.
- Dependent on the outcome of the aforementioned task, attempt the dynamic time warping (DTW) method of Mikesell et al. 2015 to increase the reliability of dt measurements and limit cycle skipping.
- Use the successful δv/v calculation method (either MWCS-altered or DTW) to identify how δv/v changes with time, frequency, and location. Use these results to isolate the frequency range in which the thaw and freeze of the active layer is most pronounced. Assess spatial variations in δv/v to determine if heterogeneity in permafrost characteristics can be determined using this method.

8. SATELITTE MEASUREMENTS

8.1 Introduction

A goal of this LDRD was to use seismic measurements, which have a relatively small aperture, as ground truth for remote sensing observations, which have a relatively large aperture. Ideally, the continuous seismic measurements would calibrate the regularly spaced (in time) remote sensing observations, which in turn could provide active layer thickness estimates over a much greater area. This measurement approach is appealing for a number of reasons including:

- Compared to current practices (i.e. isolated tile probe surveys), the method increases both temporal and spatial resolution of active layer thickness.
- The method is advantageous because it provides a mechanism for long-term sustained monitoring.
- Monitoring with satellites reduces the health and safety risk for remote field measurements in inclement weather.
- In the long term, monitoring with satellites and seismometers will be more economical than taking enough physical measurements.

In order to accomplish this goal, we teamed up with personnel from the Bureau of Land Management (BLM). The BLM administers over 250 million acres of public lands in the Western United States, with approximately 72 million acres of public lands alone in Alaska. Permafrost changes and disturbances in Alaska pose potential human and environmental impacts, which must be tracked and characterized. Due to its geographic size, and varying climate, it is impractical to monitor all permafrost cover in Alaska using manual surveying methods. The ability to monitor permafrost cover trends using deployed, in-situ instruments (such as the array described here), and to integrate these measurements with multi-temporal remotely sensed imagery, would prove greatly beneficial to the BLM, as it would increase the agency's ability to quantify and understand potential impacts to land and resource management.

8.2 Data

Multi-scale, multi-temporal remotely sensed data were used for this study. Passive electro-optical (EO) imagery systems – those that require illumination from an external power source (i.e., the Sun) were used, including high-resolution commercial WorldView-2 and WorldView-3, and synoptic Landsat missions 5 and 8. A small number of WorldView-2 and WorldView-3 scenes were available for this study. They were collected in 2014 and 2015. Landsat offered a multi-decadal historical archive, which was leveraged for this study.

Multiple Synthetic Aperture Radar (SAR) systems were used, because of their ability to collect information regardless of solar illumination or weather condition. These SAR instruments chiefly included commercial Radarsat-2, and the European Space Agency's new Sentinel-1A instrument. The Radarsat-2 and Sentinel-1A imagery exploited for this study are summarized in Table 5 and 6.

Table 5: Radarsat-2 imagery collection dates used for this study.

Date	Polarization	Spectral	Resolution	Pass (A/D)
3-Jun-13	Single - HH	Microwave	5-m	Descending
27-Jun-13	Single - HH	Microwave	5-m	Descending
21-Jul-13	Single - HH	Microwave	5-m	Descending
14-Aug-13	Single - HH	Microwave	5-m	Descending
7-Sep-13	Single - HH	Microwave	5-m	Descending
29-May-14	Single - HH	Microwave	5-m	Descending
22-Jun-14	Single - HH	Microwave	5-m	Descending
16-Jul-14	Single - HH	Microwave	5-m	Descending
9-Aug-14	Single - HH	Microwave	5-m	Descending
2-Sep-14	Single - HH	Microwave	5-m	Descending
26-Sep-14	Single - HH	Microwave	5-m	Descending

Table 6: Sentinel-1A imagery collection dates used for this study.

Date	Polarization	Spectral	Resolution	Pass
11/17/2014	Single - VV	Microwave	20-m	Ascending
1/4/2015	Single - VV	Microwave	20-m	Ascending
2/21/2015	Single - VV	Microwave	20-m	Ascending
3/5/2015	Single - VV	Microwave	20-m	Ascending
3/29/2015	Single - VV	Microwave	20-m	Ascending
4/14/2015	Single - VV	Microwave	20-m	Descending
4/22/2015	Dual - VV, VH	Microwave	20-m	Ascending
5/16/2015	Single - VV	Microwave	20-m	Ascending
5/30/2015	Single - VV	Microwave	20-m	Descending
6/1/2015	Single - VV	Microwave	20-m	Descending
6/9/2015	Single - VV	Microwave	20-m	Ascending
6/23/2015	Single - VV	Microwave	20-m	Descending
6/25/2015	Single - VV	Microwave	20-m	Descending
7/3/2015	Single - VV	Microwave	20-m	Ascending
7/17/2015	Single - VV	Microwave	20-m	Descending
7/19/2015	Single - VV	Microwave	20-m	Descending
7/27/2015	Single - VV	Microwave	20-m	Ascending

8.3 Processing

Image processing was needed for all but the Landsat data to allow quantitative geospatial analysis. This chiefly involved orthocorrection using digital elevation model (DEM) information to reduce geometric distortions, and increase geospatial positional accuracy. Additionally, all SAR data were calibrated to sigma-naught (Radar Cross Section) to allow quantitative pixel comparisons between sensor image dates. Finally, individual SAR scenes were “stacked” to form multi-band, time series image composites, based upon the sensor type (i.e., Radarsat-2, Sentinel-1A) and type of pass (ascending, descending). This was done to allow the images to be

qualitatively assessed using traditional image interpretation techniques, and to allow image-to-image change detection. Finally, this also facilitated efficient extraction of pixel values for statistical trend analysis (see section 8.4 Methods).

An object-oriented approach was used to develop a dataset, which could be used to identify spatio-temporal trends at PFRR. Using this approach, raster data pixels are grouped into meaningful image objects (vector polygons), based upon their spatial and spectral characteristics. An image segmentation (vector) dataset was produced from the high-resolution WorldView-3 imagery spanning the study area (Figure 40). Pixel value statistics were calculated for each Radarsat-2 and Sentinel-1A scene date, for each image object (including PFRR). The final vector polygon dataset contains the mean, median, minimum, and maximum pixel statistics extracted from each SAR image date.

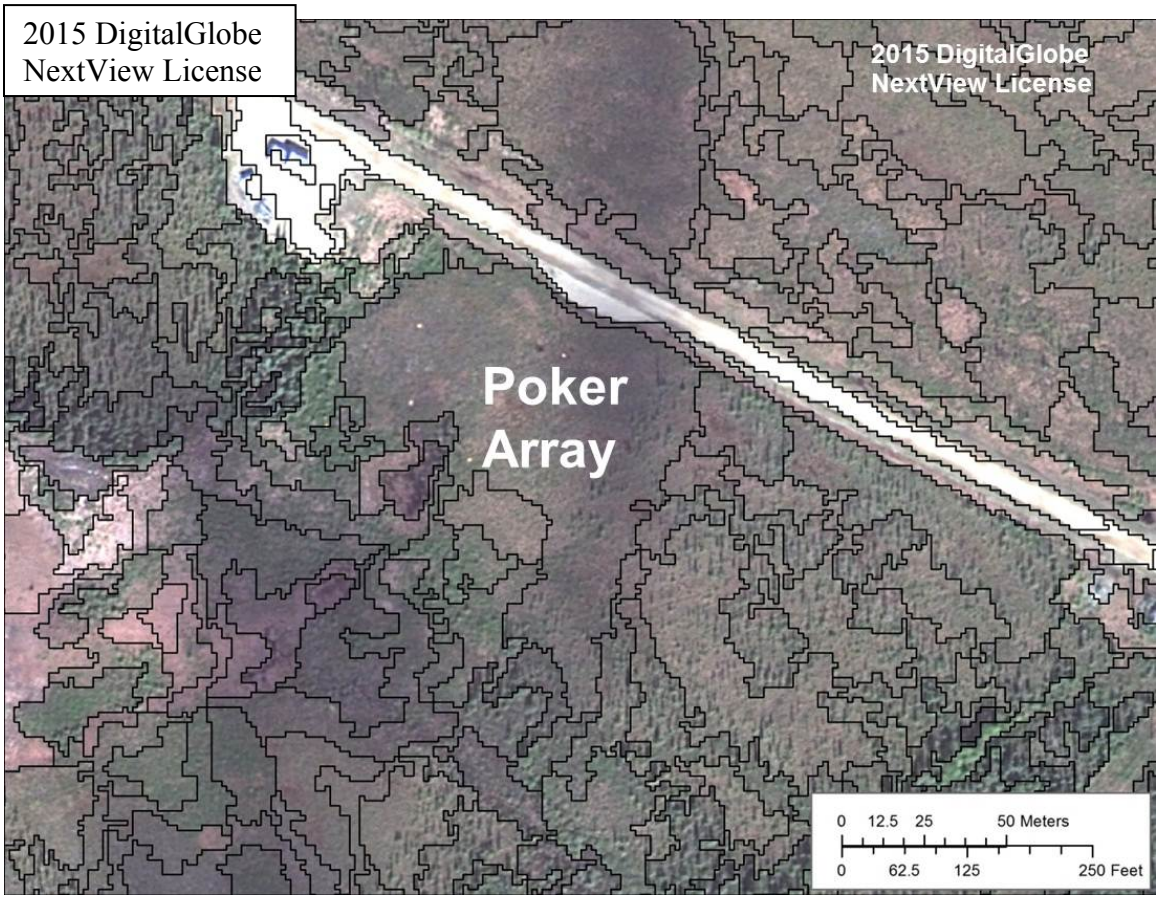

Figure 40: Image segmentation dataset (shown in black) derived from WorldView-3 imagery.

8.4 Methods

The time series stacks for Radarsat-2 and Sentinel-1A were analyzed using several techniques. First, an interpretative (qualitative) analysis was performed, to identify and understand changes in landcover, or changes in landcover state, over the greater study area of interest. A time series analysis was then performed using the image segmentation dataset (populated with imagery pixel statistics). This allowed the identification of spatio-temporal trends over time and by sensor. These trends were then summarized as charts for visualization purposes (Figure 41).

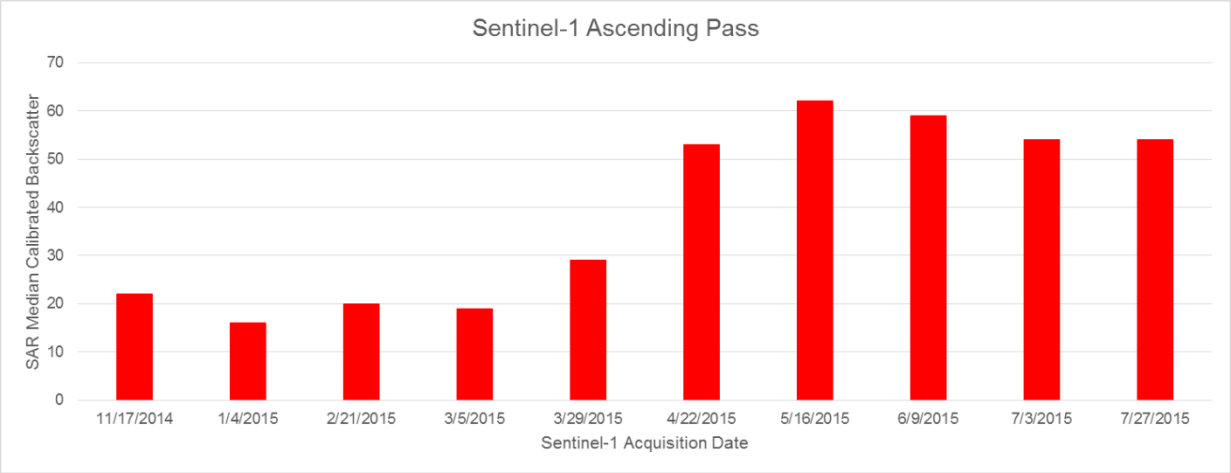

Figure 41: Time series chart identifying median Sentinel-1A (ascending pass) backscatter values for Poker Flat, Nov. 2014 to July 2015.

The use of Google Earth Engine (GEE) was also investigated and employed for this study. GEE is a cloud computing architecture, which allows the user to efficiently access, process, analyze, and develop products from large geospatial data archives. GEE proved greatly beneficial to this project, as it facilitated the analysis of spectral trends of land and water cover at PFRR over multiple decades by leveraging the entire U.S. Geological Survey (USGS) Landsat archive. This was accomplished without having to download the satellite data archive, nor devote local computational resources to process this massive dataset. Without the use of GEE, this analysis would not have been possible during the time span of the project. As such, GEE clearly provides an emergent tool for the scientific community.

We developed custom GEE scripts, which calculated multiple spectral indices (shown to be useful for land and water cover studies) from available Landsat 5 and Landsat 8 data from

1984 to the present. The spectral indices included Normalized Difference Vegetation Index (NVDI), Normalized Difference Snow Index (NDSI), and Normalized Difference Water Index (NDWI).

The script then extracted the median pixel values for each of the spectral indices (derived from each Landsat scene) spanning the PFRR study area, and produced a time series chart. This provided an unparalleled ability to characterize and visualize spatio-temporal spectral trends over the study site through multiple decades (Figure 42 and Figure 43).

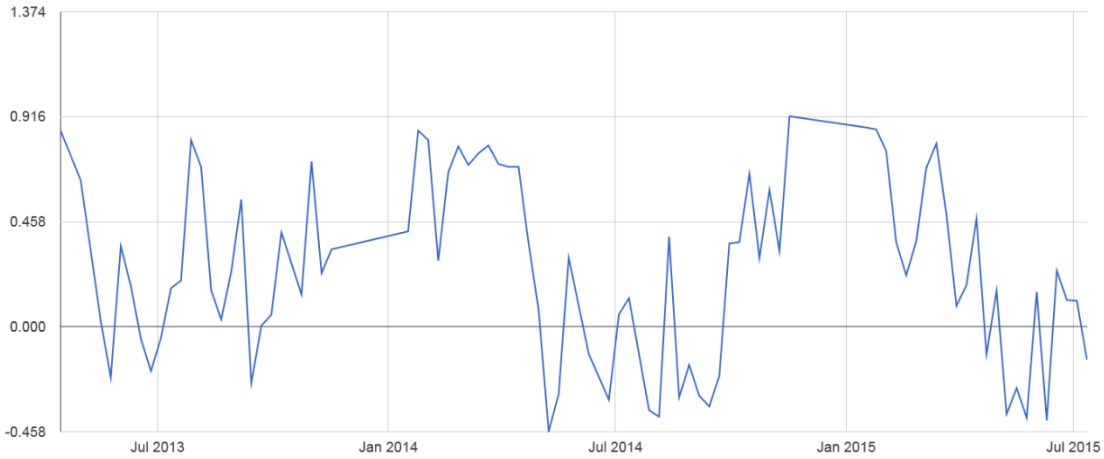

Figure 42: Time series chart identifying median Landsat 8 NDSI values for Poker Flat, 2013-2015.

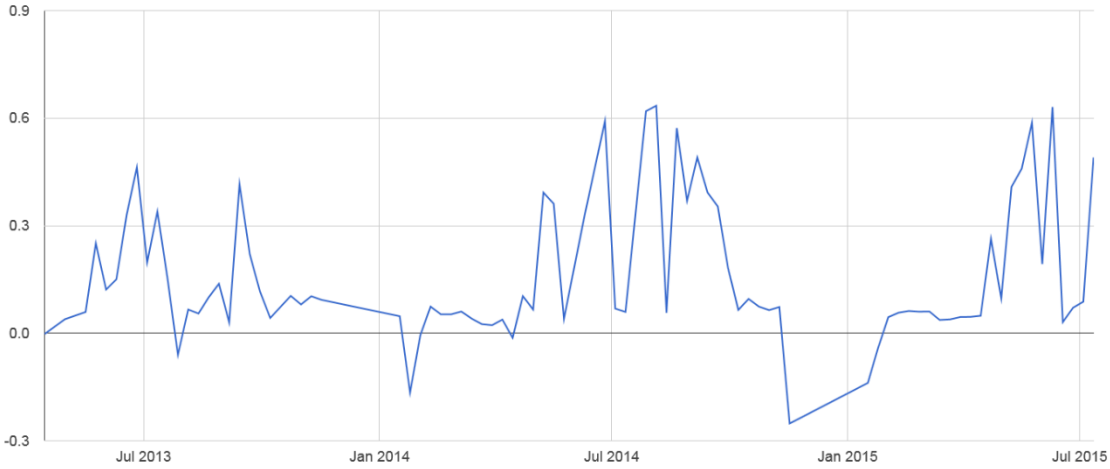

Figure 43: Time series chart identifying median Landsat 8 NDVI values for Poker Flat, 2013-2015.

8.5 Results

One encouraging result was the ability to create image classification results that match local seismic ground truth observations. The Image Segmentation dataset (Figure 40) automatically classified the PFRR region into multiple polygons. Six of the seven stations in our array occupy a single polygon and show results that are more or less consistent with each other. Station R2C, the seventh station in a neighboring polygon, showed anomalous results in the HVSR and multi-station methods and within the tile probe measurements, as well. This suggests that remote sensing can be used to generalize terrains into wide areas and use local measurements as ground truth.

Preliminary results note a strong relationship between seasonal trends and remotely sensed observations. Figure 41and Figure 43 suggest that spectral response in EO data, and in SAR backscatter measurements, differed with time of season. NDVI measurements at Poker Flats decreased strongly in winter, and increased strongly from spring to summer. This trend is likely due to phenology – that is, the increase in photosynthetic activity ("greenup") during the late spring and summer, and corresponding decrease in late fall to winter. Conversely, NDSI measurements at Poker Flats increased strongly in late fall to winter, and decreased significantly in summer. This is due to the presence of snow and/or ice cover. Time series analysis suggest SAR backscatter measurements followed a trend similar to that of the NDVI measurements - that is, an increase in backscatter during late spring to summer, followed by a decrease in winter. This trend was also confirmed by qualitative, interpretative analysis of the SAR multi-temporal imagery, and through change detection products derived from multiple SAR scene dates.

8.6 Challenges

There were unforeseen logistical and technical challenges, which adversely affected progress made in, and results obtained for, this study. The use of Interferometric SAR (InSAR) techniques was originally slated to comprise a significant portion of the study, and would have proven greatly beneficial in linking in-situ measurements and remotely sensed observations. However, a large portion of the commercial SAR data was lost and not recoverable during this stage of the project. Commercial InSAR software was not available until the end of this effort.

Additionally, while Sentinel-1A offers an emerging tool for fine-scale InSAR measurements, existing SAR analytical software packages have not fully developed an ability to ingest and analyze this system at present. Finally, agency budgetary restrictions forced a cancellation of a planned BLM/SNL workshop, which hindered our integrated analysis. Each of these problems should be resolved in the near future.

8.7 Proposed future work

Despite our progress and accomplishments, the work to quantitatively integrate field-based measurements and remotely sensed observations needs to be finalized. A future analytical workshop could assist in this regard. We further propose the acquisition and analysis of follow on Landsat 8, Sentinel-1A SAR, and ALOS PALSAR-2 remotely sensed imagery. The latter two instruments operate at different wavelengths (C- and L-Band, respectively), and offer different abilities to penetrate and resolve terrestrial cover information. While C Band SAR such as Sentinel-1A are very sensitive to surficial changes and disturbances, L-Band instruments such as ALOS are able to penetrate ground, and could be beneficial in characterizing permafrost, particularly when considering InSAR measurements.

The use of Google Earth should be further explored for this project as well. This could facilitate the integration of other geospatial datasets, including meteorological data and multi-scale remotely sensed observations into our methodological framework. GEE has begun ingesting Sentinel -1A SAR information into its burgeoning archive; this could streamline our efforts greatly. The refinement of existing scripts could be pursued to eliminate pixel outliers found in the Landsat time series, likely due to weather effects (snow, rain, clouds) at or near Poker Flat. Finally, GEE offers numerous analytical capabilities and data classification algorithms not yet fully explored at present.

9. PROJECT CONCLUSIONS

The LDRD, as it was originally designed, set out to remotely monitor active layer thickness in real time over an area larger than that occupied by a single borehole. Not surprisingly, the work here found that there are still technical gaps that must be filled before this method can be utilized on a regional scale. Below we will discuss the conclusions and lessons learned from each the station siting and engineering, the ground truth methods, the single station method, the multi-station method, and the calibration of satellite measurements.

Concerning the station siting and the engineering, the most important conclusions from this LDRD are as follows:

- Siting stations in a protected and remote location prevented vandalism and theft. The lack of trained on-site personnel, however, proved a bottleneck when operational problems arose. In the future, projects like these should seek partnerships where trained professionals (i.e. graduate students) are available for troubleshooting.
- The existing infrastructure proved a means by which batteries, solar panels, etc. were not required. The power and internet connections were not, however, as robust as initially thought. In the future, a backup battery system should be in place to help alleviate the data losses during power outages.
- The PoE system was determined as the highest likelihood single point of failure for the whole system. The PoE was particularly sensitive to changes in environmental conditions. In the future, the PoE housing structure needs to be rethought and/or there needs to be another means by which to provide both power and data transfer.
- Even with the exceptions listed above, the overall system design and siting was deemed to be highly satisfactory. The stations were protected and performed very well given the harsh environmental conditions they were exposed to. Ultimately, this pilot study provided further evidence that SNL has the capabilities to keep a remote, autonomous station recording high fidelity data through extreme environmental changes and harsh conditions.

Over the course of this 2+ year LDRD, the technical team decided to acquire three different types of ground truth data for calibrating the single and multi-station methods. The

challenges associated with each of these methods are detailed in the earlier sections. One of the primary take away messages from this work was that special considerations for both geophysical methods (ReMi and CS) need to be made for working in partially frozen/thawed ground and that standard installation procedures are likely inadequate. The second conclusion was that the fidelity of the ground truth measurements was greatly increased by incorporating all three results. Future investigations should employ all three techniques if budget and time constraints allow.

Concerning the exploratory nature of this project, specifically using single- and multi-station seismic methods for determining active layer thickness, there were many lessons learned and conclusions from the work. We will only discuss the most important ones here. The single station method showed that it could reliably measure temporal changes in HVSR and that these changes could be linked back to changes in active layer thickness. The inversion for active layer thickness was unfortunately non-unique, but the incorporation of ground truth data will adequately constrain the problem. The drawback of this technique is that it only samples the area directly surrounding the instrument, which is similar to the role of borehole thermometers and/or frost tubes. The added benefit of using this instrument to measure active layer thicknesses lies in the multi-purpose data gained from seismometers. Specifically, while measuring active layer thickness, the instrument will also be monitoring for local, regional, and teleseismic earthquakes, bombs, etc. This makes this active layer thickness monitoring tool much more diverse, albeit less accurate, than borehole thermometers and frost tubes. Finally, this method also illustrated that the standard way of estimating site responses for structural design needs to incorporate the drastic changes in near surface material property changes in a more sophisticated way.

The multi-station method has to-date proven promising but has not definitively shown temporally varying active layer thicknesses sampled at inter-station distances. This is because resolving actively layer thickness is unexpectedly and inherently difficult using this technique. The highest frequencies, which sample the very near surface, are attenuated in this geologically heterogeneous medium. This reduces the signal to noise ratio of the data required to make the measurement. The stations could be placed closer together, but this would cause the auto-correlations to be strong and drastically reduce the spatial sampling. Ambient noise modeling would need to be conducted to determine the appropriate station spacing SNR trade off.

Furthermore, the site where the stations are deployed should have a diverse (both in frequency content and azimuth) ambient noise field. This would drastically improve the SNR. We propose that ideal candidates would be military installations and other facilities with adequate anthropogenic noise. It is worth mentioning here that undertaking this analysis has brought new insight into the ambient noise field and how temporal changes are tracked in media where velocity changes are much greater than a few percent over a fixed time period. This work addressed that problem by creating a relative change detection, day-to-day, rather than a fixed time reference (i.e. pre-earthquake vs. post-earthquake) and cleverly accumulating those changes over a whole season in this case. This technique has not been utilized before. Work measuring active layer thicknesses as a function of time and space continues at the University of Florida and shows great promise.

The final objective of this LDRD was to calibrate satellite measurements that measure/estimate active layer thickness with a ground based method that samples similar spatial scales. This work as outlined above was undertaken by Chris Cole at the BLM (also an author here). This collaboration was unfortunately riddled with delays and was finally undertaken in a meaningful way in the last quarter of this LDRD. The research idea, however, shows great promise especially for entities like BLM, who manage the National Petroleum Reserve in Alaska (~24 million acres). The timing for this research is also primed with the new Sentinel-1 data and the use of GEE to process and integrate data sets. The team is seeking additional funding to solidify this research and build on the results of this LDRD.

In conclusion, the technical challenges associated with monitoring active layer thickness in real time and/or at the temporal and spatial scale described here are much better understood upon completing this pilot research project at PFRR. This LDRD also established a robust collaboration with the University of Alaska Fairbanks, the University of Florida, and the BLM. Future projects are presently being pursued to tackle remaining questions and technical challenges enlightened here.

10. REFERENCES

Abbott, R. E. "Seismic Spatial Autocorrelation as a Technique to Track Changes in the Permafrost Active Layer." *AGU Fall Meeting Abstracts*. Vol. 1. 2013.

Aki, Keiiti. "Local site effects on weak and strong ground motion." *Tectonophysics* 218.1 (1993): 93-111.

Aki, Keiiti, and Paul G. Richards. *Quantitative seismology*. Vol. 1. 2002.

Assessment, Arctic Climate Impact. "Impacts of a Warming Arctic-Arctic Climate Impact Assessment." *Impacts of a Warming Arctic-Arctic Climate Impact Assessment, by Arctic Climate Impact Assessment, pp. 144. ISBN 0521617782. Cambridge, UK: Cambridge University Press, December 2004.* 1 (2004).

Bard, P. Y. "Guidelines for the implementation of the H/V spectral ratio technique on ambient vibrations: measurements, processing and interpretation. SESAME European research project, WP12—Deliverable D23. 12." (2004).

Boore, David M., and William B. Joyner. "Site amplifications for generic rock sites." *Bulletin of the seismological society of America* 87.2 (1997): 327-341.

Brenguier, Florent, et al. "Towards forecasting volcanic eruptions using seismic noise." *Nature Geoscience* 1.2 (2008): 126-130.

Brenguier, Florent, et al. "Monitoring volcanoes using seismic noise correlations." *Comptes Rendus Geoscience* 343.8 (2011): 633-638.

Campillo, Michel, and Anne Paul. "Long-range correlations in the diffuse seismic coda." *Science* 299.5606 (2003): 547-549.

“Chatanika River Mine, Fairbanks District, Fairbanks North Star Borough, Alaska, USA,”. 8-7-15. http://www.mindat.org/loc-196874.html

Corchete, V. "A methodology for the analysis of the Rayleigh-wave ellipticity."*Earth Sciences Research Journal* 17.2 (2013): 127-133.

Curtis, Andrew, et al. "Seismic interferometry—turning noise into signal." *The Leading Edge* 25.9 (2006): 1082-1092.

Draganov, Deyan, et al. "Retrieval of reflections from seismic background-noise measurements." *Geophysical Research Letters* 34.4 (2007).

Duputel, Zacharie, et al. "Real time monitoring of relative velocity changes using ambient seismic noise at the Piton de la Fournaise volcano (La Réunion) from January 2006 to June 2007." *Journal of Volcanology and Geothermal Research*184.1 (2009): 164-173.

Evans, Jenni L. "Sensitivity of tropical cyclone intensity to sea surface temperature." *Journal of Climate* 6.6 (1993): 1133-1140.

Field, Edward H., and SCEC Phase III Working Group. "Accounting for site effects in probabilistic seismic hazard analyses of Southern California: overview of the SCEC Phase III report." *Bulletin of the Seismological Society of America*90.6B (2000): S1-S31.

Gruber, S., and W. Haeberli. "Permafrost in steep bedrock slopes and its temperature-related destabilization following climate change." *Journal of Geophysical Research: Earth Surface (2003–2012)* 112.F2 (2007).

Hadziioannou, Céline, et al. "Stability of monitoring weak changes in multiply scattering media with ambient noise correlation: Laboratory experiments." *The Journal of the Acoustical Society of America* 125.6 (2009): 3688-3695.

Holzer, Thomas L., et al. "Shear-wave velocity of surficial geologic sediments in Northern California: statistical distributions and depth dependence." *Earthquake Spectra* 21.1 (2005): 161-177.

Iwata, Yukiyoshi, et al. "Comparison of soil frost and thaw depths measured using frost tubes and other methods." *Cold Regions Science and Technology*71 (2012): 111-117.

Jorgenson, M. Torre, Yuri L. Shur, and Erik R. Pullman. "Abrupt increase in permafrost degradation in Arctic Alaska." *Geophysical Research Letters* 33.2 (2006).

Jorgenson, M. Torre, et al. "Resilience and vulnerability of permafrost to climate change This article is one of a selection of papers from The Dynamics of Change in Alaska's Boreal Forests: Resilience and Vulnerability in Response to Climate Warming." *Canadian Journal of Forest Research* 40.7 (2010): 1219-1236.

Kawase, Hiroshi, et al. "Applicability of Theoretical Horizontal-to-Vertical Ratio of Microtremors Based on the Diffuse Field Concept to Previously Observed Data." *Bulletin of the Seismological Society of America* (2015).

Konno, Katsuaki, and Tatsuo Ohmachi. "Ground-motion characteristics estimated from spectral ratio between horizontal and vertical components of microtremor." *Bulletin of the Seismological Society of America* 88.1 (1998): 228-241.

Lee, R. F., et al. "Seasonal changes in H/V spectral ratio at high-latitude seismic stations." *AGU Fall Meeting Abstracts*. Vol. 1. 2014.

Le Roux, Olivier, et al. "1-D and 2-D resonances in an Alpine valley identified from ambient noise measurements and 3-D modelling." *Geophysical Journal International* 191.2 (2012): 579-590.

Lin, Fan-Chi, Morgan P. Moschetti, and Michael H. Ritzwoller. "Surface wave tomography of the western United States from ambient seismic noise: Rayleigh and Love wave phase velocity maps." *Geophysical Journal International* 173.1 (2008): 281-298.

Lin, Fan-Chi, Brandon Schmandt, and Victor C. Tsai. "Joint inversion of Rayleigh wave phase velocity and ellipticity using USArray: Constraining velocity and density structure in the upper crust." *Geophysical Research Letters*39.12 (2012).

Lobkis, Oleg I., and Richard L. Weaver. "On the emergence of the Green's function in the correlations of a diffuse field." *The Journal of the Acoustical Society of America* 110.6 (2001): 3011-3017.

Louie, John N. "Faster, better: shear-wave velocity to 100 meters depth from refraction microtremor arrays." *Bulletin of the Seismological Society of America*91.2 (2001): 347-364.

Mainsant, Guénolé, et al. "Ambient seismic noise monitoring of a clay landslide: Toward failure prediction." *Journal of Geophysical Research: Earth Surface (2003–2012)* 117.F1 (2012).

McMechan, George A., and Mathew J. Yedlin. "Analysis of dispersive waves by wave field transformation." *Geophysics* 46.6 (1981): 869-874.

Mordret, A., et al. "Monitoring of phreatic eruptions using interferometry on retrieved cross-correlation function from ambient seismic noise: Results from Mt. Ruapehu, New Zealand." *Journal of Volcanology and Geothermal Research*191.1 (2010): 46-59.

Mortensen, J. K. "Pre-mid-Mesozoic tectonic evolution of the Yukon-Tanana terrane, Yukon and Alaska." *Tectonics* 11.4 (1992): 836-853.

Nakamura, Yutaka. "On the H/V spectrum." *The 14th World Conference on Earthquake Engineering, Beijing, China*. 2008.

Nelson, Fritz, et al. "Active layer protocol." *ITEX manual* (1996): 14-16.

Nelson, Frederick E., Oleg A. Anisimov, and Nikolay I. Shiklomanov. "Subsidence risk from thawing permafrost." *Nature* 410.6831 (2001): 889-890.

Newberry, Rainer J., et al. "Preliminary geologic map of the Fairbanks mining district, Alaska." (1996).

Nowacki, G., et al. "Ecoregions of Alaska and neighboring territory (map)." *US Geological Survey, Reston, VA. http://agdc. usgs. gov/data/projects/fhm/akecoregions. jpeg* (2001).

Poggi, Valerio, et al. "Modal analysis of 2-D sedimentary basin from frequency domain decomposition of ambient vibration array recordings." *Geophysical Journal International* 200.1 (2015): 615-626.

Robinson, Mark S., Thomas Edward Smith, and Paul A. Metz. *Bedrock geology of the Fairbanks mining district*. Alaska Division of Geological and Geophysical Surveys, 1990.

Sabra, Karim G., et al. "Surface wave tomography from microseisms in Southern California." *Geophysical Research Letters* 32.14 (2005).

Sens-Schönfelder, Christoph, and U. Wegler. "Passive image interferometry and seasonal variations of seismic velocities at Merapi Volcano, Indonesia."*Geophysical research letters* 33.21 (2006).

Sens-Schönfelder, Christoph, and Ulrich Wegler. "Passive image interferometry for monitoring crustal changes with ambient seismic noise." *Comptes Rendus Geoscience* 343.8 (2011): 639-651.

Shapiro, Nikolai M., and Michel Campillo. "Emergence of broadband Rayleigh waves from correlations of the ambient seismic noise." *Geophysical Research Letters* 31.7 (2004).

Shapiro, Nikolai M., et al. "High-resolution surface-wave tomography from ambient seismic noise." *Science* 307.5715 (2005): 1615-1618.

Schuur, Edward AG, et al. "Vulnerability of permafrost carbon to climate change: Implications for the global carbon cycle." *BioScience* 58.8 (2008): 701-714.

Schuur, Edward AG, et al. "The effect of permafrost thaw on old carbon release and net carbon exchange from tundra." *Nature* 459.7246 (2009): 556-559.

Snieder, Roel, et al. "Coda wave interferometry for estimating nonlinear behavior in seismic velocity." *Science* 295.5563 (2002): 2253-2255.

Snieder, Roel. "The theory of coda wave interferometry." *Pure and Applied Geophysics* 163.2-3 (2006): 455-473.

Steidl, Jamison H., Alexei G. Tumarkin, and Ralph J. Archuleta. "What is a reference site?." *Bulletin of the Seismological Society of America* 86.6 (1996): 1733-1748.

Weaver, Richard L., and Oleg I. Lobkis. "Ultrasonics without a source: Thermal fluctuation correlations at MHz frequencies." *Physical Review Letters* 87.13 (2001): 134301.

Geological Survey (US), and Frederic H. Wilson. *Geologic map of central (interior) Alaska*. US Geological Survey, 1998.

Yang, Yingjie, et al. "Ambient noise Rayleigh wave tomography across Europe."*Geophysical Journal International* 168.1 (2007): 259-274.

Yershov, Eduard Dmitrievich, and Peter J. Williams. *General geocryology*. Cambridge university press, 2004.

Yoshikawa, Kenji, et al. *Permafrost characteristics of Alaska*. Fairbanks: Institute of Northern Engineering, University of Alaska, 2008 (map).

Zimmerman, Robert W., and Michael S. King. "The effect of the extent of freezing on seismic velocities in unconsolidated permafrost." *Geophysics* 51.6 (1986): 1285-1290.

Zimov, Sergey A., Edward AG Schuur, and F. Stuart Chapin III. "Permafrost and the global carbon budget." *Science(Washington)* 312.5780 (2006): 1612-1613.

APPENDIX A: ACTIVE LAYER THICKNESS MEASUREMENTS

October 2013

Table 7: Tile Probe Measurements at Stations October 2013

Station Name	Measure (cm)
R1A	64
R2A	53
R1B	> 91
CE1	76
R1C	46
R2C	> 91
R2B	>> 91

July 2014

Table 8: Tile Probe R2A-R2C Transect July 2014

Transect: R2A-R2C		Date: 7/7/14
Meter Mark	**Thickness (cm)**	**Comments**
87	40	At R2A
86	42	
85	45	
84	38	
83	41	
82	38	
81	43	
80	40	
79	90	Lake
78	63	
77	36	
76	40	
75	31	
74	31	
73	39	
72	38	
71	31	
70	32	

69	34	
68	38	
67	32	
66	39	
65	38	
64	31	
63	34	
62	35	
61	32	
60	33	
59	32	
58	41	
57	36	
56	32	
55	36	
54	41	
53	40	
52	41	
51	40	
50	36	
49	35	
48	38	
47	38	
46	38	
45	39	
44	40	
43	61	
42	45	At R1A
41	66	
40	55	
39	55	
38	40	
37	45	
36	45	
35	40	
34	35	
33	42	
32	55	
31	50	
30	92	Lake
29	100	Lake

28	160	Lake
27	155	Lake
26	160	Lake
25	149	Lake
24	162	Lake
23	155	Lake
22	160	Lake
21	125	Lake
20	140	Lake
19	121	Lake
18	140	Lake
17	140	Lake
16	125	Lake
15	145	Lake
14	125	Lake
13	120	Lake
12	135	Lake
11	110	Lake
10	90	Trees
9	90	Trees
8	100	Trees
7	100	Trees
6	100	Trees
5	90	Trees
4	90	Trees
3	90	Trees
2	85	Trees
1	100	Trees
0	100	At R2C

Table 9: Tile Probe R2A-R1B Transect July 2014

Transect R2A-R1B		Date: 7/7/14
Meter Mark	**Thickness (cm)**	**Comments**
0	40	At R2A
2	30	
4	42	
6	36	
8	35	
10	34	
12	43	

14	35	
16	35	
18	40	
20	41	
22	35	
24	70	
26	43	
28	49	
30	36	
32	32	
34	50	
36	60	
38	50	
40	45	
42	40	

Table 10: Tile Probe R1B-R2B Transect July 2014

Transect R1B-R2B		Date: 7/7/14
Meter Mark	**Thickness (cm)**	**Comments**
0	45	At R1B
2	50	
4	38	
6	46	
8	38	
10	52	
12	40	
14	40	Lake
16	32	Lake
18	40	Lake
20	40	Lake
22	--------	Lake
24	--------	Lake
26	35	Lake
28	50	
30	40	
32	54	
34	45	
36	44	
38	50	
40	75	
42	110	

44	80	
45	88	At R2B

Table 11: Tile Probe R2B-R2C Transect July 2014

Transect R2B-R2C		Date: 7/7/14
Meter Mark	**Thickness (cm)**	**Comments**
86	50	
84	42	
82	44	
80	45	
78	50	
76	50	Tall Shrub
74	42	
72	52	
70	58	
68	50	
66	55	
64	60	
62	60	
60	50	
58	88	
56	130	
54	50	
52	48	
50	50	
48	45	
46	40	
44	140	At R1C
42	130	Wet
40	125	Wet
38	130	Wet
36	130	Wet
34	130	Wet
32	135	Wet
30	130	Wet
28	120	Wet
26	118	Wet
24	130	Dry
22	122	
20	110	

18	120	
16	110	
14	100	
12	110	
10	110	
8	80	
6	81	
4	100	
2	80	
0	92	At R2C

Table 12: Tile Probe R2A-R1C Transect July 2014

Transect R2A-R1C		Date: 7/8/14
Meter Mark	**Thickness (cm)**	**Comments**
76	42	
74	40	
72	36	
70	38	
68	40	
66	38	
64	36	
62	34	
60	28	
58	30	
56	33	
54	36	
52	122	
50	65	
48	32	
46	45	
44	35	
42	38	
40	61	
38	48	
36	48	
34	35	
32	31	
30	36	
28	32	At CE

26	45	At CE
24	40	
22	48	
20	100	
18	56	
16	60	
14	78	
12	70	Deep in H2O
10	120	Deep in H2O
8	120	Deep in H2O
6	14	Deep in H2O
4	100	Deep in H2O
2	100	Deep in H2O
0	120	At RIC

Table 13: Tile Probe PIC-2 Transect July 2014

Transect PIC-2		7/8/14
Meter Mark	**Thickness (cm)**	**Comments**
0	39	
2	32	
4	43	
6	44	
8	40	
10	48	
12	47	
13	38	
15	48	
16	47	

MAY 27, 2015

Table 14: Tile Probe Measurements at Stations May 2015

Station Name	Measure 1 (cm)	Measure 2 (cm)	Measure 3 (cm)	Measure 4 (cm)	Average (cm)	Standard Deviation (cm)
R1A	19.5	21	24	20	21.1	2.0
R2A	23.5	24	19.5	21	22.0	2.1

R1B	19	20	18	19	19.0	0.8
CE1	19	23	23.5	22	21.9	2.0
R1C	35	38	35.5	29	34.4	3.8
R2C	22	22	26	29	24.8	3.4

June 17, 2015

Table 15: Tile Probe R2A - R1A Transect June 2015

R2A to R1A	Total distance = 44.8 m			
	Depth (mm)			
Distance (m)	1	2	3	AVERAGE (mm)
0	325	336	306	322.333
1	356	347	360	354.333
2	335	291	327	317.667
3	334	306	339	326.333
4	260	240	239	246.333
5	287	290	290	289.000
6	343	278	325	315.333
7	360	310	373	347.667
8	408	446	435	429.667
9	398	399	390	395.667
10	291	270	315	292.000
11	225	240	206	223.667
12	275	224	257	252.000
13	246	259	250	251.667
14	242	275	277	264.667
15	286	292	264	280.667
16	225	234	197	218.667
17	225	203	235	221.000
18	247	247	263	252.333
19	305	285	284	291.333
20	284	261	274	273.000
21	270	260	264	264.667
22	288	281	264	277.667
23	275	214	245	244.667
24	238	228	220	228.667
25	273	266	255	264.667
26	296	275	294	288.333
27	255	245	250	250.000

28	247	260	268	258.333
29	232	246	275	251.000
30	216	220	230	222.000
31	290	275	285	283.333
32	70	285	265	206.667
33	310	290	315	305.000
34	290	265	280	278.333
35	284	286	290	286.667
36	333	355	345	344.333
37	267	293	285	281.667
38	307	343	345	331.667
39	260	298	260	272.667
40	305	270	280	285.000
41	286	272	271	276.333
42	295	289	300	294.667
43	327	335	337	333.000
44	455	443	434	444.000

Table 16: Tile Probe R1A-R2C Transect June 2015

R1A to R2C	Total distance = 43.1 m			
	Depth (mm)			
Distance (m)	1	2	3	AVERAGE (mm)
0	330	300	355	328.333
1	310	328	290	309.333
2	320	325	300	315.000
3	342	349	330	340.333
4	326	325	331	327.333
5	305	334	300	313.000
6	369	367	365	367.000
7	290	330	298	306.000
8	367	316	296	326.333
9	378	379	397	384.667
10	456	438	454	449.333
11	420	418	442	426.667
12	456	449	460	455.000
13	428	420	425	424.333
14	440	432	423	431.667
15	456	453	458	455.667
16	490	500	465	485.000
17	356	417	417	396.667
18	373	390	388	383.667

19	414	412	394	406.667
20	457	449	471	459.000
21	425	469	414	436.000
22	365	380	379	374.667
23	355	367	372	364.667
24	352	346	336	344.667
25	330	334	327	330.333
26	286	300	306	297.333
27	319	328	267	304.667
28	345	308	310	321.000
29	290	202	222	238.000
30	270	267	255	264.000
31	361	370	365	365.333
32	294	299	299	297.333
33	351	387	386	374.667
34	444	398	415	419.000
35	312	324	300	312.000
36	283	278	300	287.000
37	222	240	224	228.667
38	249	242	250	247.000
39	274	284	280	279.333
40	264	250	284	266.000
41	370	375	395	380.000
42	306	314	310	310.000
43	304	289	280	291.000

Table 17: Tile Probe R2C-R1C Transect June 2015

R2C to R1C	Total distance = 43.6 m			
	Depth (mm)			
Distance (m)	1	2	3	AVERAGE (mm)
0	320	295	290	301.667
1	260	270	272	267.333
2	380	395	370	381.667
3	220	251	248	239.667
4	298	299	308	301.667
5	400	424	406	410.000
6	439	413	464	438.667
7	1018	1034	1010	1020.667
8	1133	1111	1166	1136.667
9	330	383	385	366.000
10	300	324	292	305.333

11	1158	1204	1234	1198.667
12	428	440	438	435.333
13	351	382	381	371.333
14	403	407	378	396.000
15	1283	1241	1225	1249.667
16	1243	1224	1268	1245.000
17	394	364	377	378.333
18	378	360	380	372.667
19	311	302	330	314.333
20	320	344	327	330.333
21	1163	1306	1289	1252.667
22	1354	1353	1374	1360.333
23	350	361	373	361.333
24	500	520	525	515.000
25	518	500	530	516.000
26	572	576	547	565.000
27	1332	1361	1361	1351.333
28	1370	1399	1388	1385.667
29	1190	1204	1219	1204.333
30	1570	1599	1593	1587.333
31	1622	1644	1649	1638.333
32	1444	1445	1450	1446.333
33	1357	1364	1384	1368.333
34	1539	1479	1494	1504.000
35	1458	1501	1523	1494.000
36	1584	1629	1528	1580.333
37	546	510	480	512.000
38	431	464	460	451.667
39	461	470	498	476.333
40	420	417	431	422.667
41	511	485	492	496.000
42	528	533	519	526.667
43	480	479	464	474.333

Table 18: Tile Probe R1C-R2B Transect June 2015

R1C to R2B	Total distance = 43.6 m			
	Depth (mm)			
Distance (m)	1	2	3	AVERAGE (mm)
0	425	435	395	418.333
2	365	380	410	385.000
4	395	425	480	433.333

6	380	380	380	380.000
8	380	390	395	388.333
10	415	490	415	440.000
12	490	495	525	503.333
14	510	490	595	531.667
16	490	490	450	476.667
18	410	420	385	405.000
20	390	395	390	391.667
22	280	310	325	305.000
24	>2000	>2000	>2000	>2000.000
26	360	375	341	358.667
28	348	330	313	330.333
30	398	264	295	319.000
32	385	368	345	366.000
34	410	436	457	434.333
36	316	310	305	310.333
38	360	360	362	360.667
40	297	280	277	284.667
42	465	415	433	437.667

Table 19: Tile Probe R2B-R1B Transect June 2015

R2B to R1B	Total distance = 45 m			
	Depth (mm)			
Distance (m)	1	2	3	AVERAGE (mm)
0	510	540	525	525.000
2	510	520	530	520.000
4	440	495	470	468.333
6	470	440	415	441.667
8	480	490	480	483.333
10	240	295	265	266.667
12	300	380	310	330.000
14	385	365	405	385.000
16	275	295	285	285.000
18	315	340	313	322.667
20	300	380	285	321.667
22	335	325	335	331.667
24	435	380	495	436.667
26	410	455	400	421.667
28	295	335	285	305.000
30	170	150	255	191.667
32	212	230	195	212.333

34	253	245	250	249.333
36	211	210	225	215.333
38	246	255	260	253.667
40	235	235	229	233.000
42	346	372	276	331.333
44	300	330	270	300.000

Table 20: Tile Probe R1B-R2A Transect June 2015

R1B to R2A	Total distance = 44.5 m			
	Depth (mm)			
Distance (m)	1	2	3	AVERAGE (mm)
0	290	290	325	301.667
2	230	255	235	240.000
4	240	240	250	243.333
6	265	320	290	291.667
8	295	325	325	315.000
10	280	255	330	288.333
12	205	215	255	225.000
14	240	235	230	235.000
16	315	360	340	338.333
18	350	390	380	373.333
20	305	340	325	323.333
22	285	275	310	290.000
24	325	320	335	326.667
26	290	295	270	285.000
28	285	265	240	263.333
30	173	240	206	206.333
32	286	270	310	288.667
34	220	260	212	230.667
36	220	230	235	228.333
38	257	236	230	241.000
40	220	267	235	240.667
42	260	240	260	253.333
44	251	295	320	288.667

Table 21: Tile Probe R2A-CE1 Transect June 2015

R2A to CE1	Total distance = 49.5 m			
	Depth (mm)			
Distance (m)	1	2	3	AVERAGE (mm)
0	320	232	340	297.333

4	320	305	280	301.667
8	325	345	310	326.667
12	265	280	265	270.000
16	325	320	340	328.333
20	275	275	295	281.667
24	335	370	350	351.667
28	175	275	330	260.000
32	260	260	250	256.667
36	304	310	305	306.333
40	395	404	381	393.333
44	315	280	297	297.333
48	280	280	295	285.000

Table 22: Tile Probe CE1-R1C Transect June 2015

CE1 to R1C	Total distance = 27.5 m			
	Depth (mm)			
Distance (m)	1	2	3	AVERAGE (mm)
4	272	290	274	278.667
8	435	469	465	456.333
12	456	495	494	481.667
16	410	453	460	441.000
20	495	465	450	470.000
24	375	395	392	387.333

APPENDIX B: REMI GEOPHONE LOCATIONS JULY 2014

Table 23: Geophone Locations for ReMi Survey I

Station ID	Manufacturer	Model	Type of Sensor	Latitude	Longitude
1	Geospace	GS-11D	Geophone	65.12580523	-147.4749979
2	Geospace	GS-11D	Geophone	65.1257985	-147.4750256
3	Geospace	GS-11D	Geophone	65.12579178	-147.4750533
4	Geospace	GS-11D	Geophone	65.12578505	-147.475081
5	Geospace	GS-11D	Geophone	65.12577832	-147.4751087
6	Geospace	GS-11D	Geophone	65.1257716	-147.4751364
7	Geospace	GS-11D	Geophone	65.12576487	-147.4751641
8	Geospace	GS-11D	Geophone	65.12575814	-147.4751918
9	Geospace	GS-11D	Geophone	65.12575142	-147.4752195
10	Geospace	GS-11D	Geophone	65.12574469	-147.4752472
11	Geospace	GS-11D	Geophone	65.12573796	-147.4752749
12	Geospace	GS-11D	Geophone	65.12573124	-147.4753026
13	Geospace	GS-11D	Geophone	65.12572451	-147.4753304
14	Geospace	GS-11D	Geophone	65.12571778	-147.4753581
15	Geospace	GS-11D	Geophone	65.12571105	-147.4753858
16	Geospace	GS-11D	Geophone	65.12570433	-147.4754135
17	Geospace	GS-11D	Geophone	65.1256976	-147.4754412
18	Geospace	GS-11D	Geophone	65.12569087	-147.4754689
19	Geospace	GS-11D	Geophone	65.12568415	-147.4754966
20	Geospace	GS-11D	Geophone	65.12567742	-147.4755243
21	Geospace	GS-11D	Geophone	65.12567069	-147.475552
22	Geospace	GS-11D	Geophone	65.12566397	-147.4755797
23	Geospace	GS-11D	Geophone	65.12565724	-147.4756074
24	Geospace	GS-11D	Geophone	65.12565051	-147.4756351
25	Geospace	GS-11D	Geophone	65.12564379	-147.4756628
26	Geospace	GS-11D	Geophone	65.12563706	-147.4756905
27	Geospace	GS-11D	Geophone	65.12563033	-147.4757182
28	Geospace	GS-11D	Geophone	65.12562361	-147.4757459
29	Geospace	GS-11D	Geophone	65.12561688	-147.4757736
30	Geospace	GS-11D	Geophone	65.12561015	-147.4758013
31	Geospace	GS-11D	Geophone	65.12560343	-147.475829
32	Geospace	GS-11D	Geophone	65.1255967	-147.4758567
33	Geospace	GS-11D	Geophone	65.12558997	-147.4758844
34	Geospace	GS-11D	Geophone	65.12558325	-147.4759121
35	Geospace	GS-11D	Geophone	65.12557652	-147.4759398
36	Geospace	GS-11D	Geophone	65.12556979	-147.4759675
37	Geospace	GS-11D	Geophone	65.12556307	-147.4759952

38	Geospace	GS-11D	Geophone	65.12555634	-147.476023
39	Geospace	GS-11D	Geophone	65.12554961	-147.4760507
40	Geospace	GS-11D	Geophone	65.12554288	-147.4760784
41	Geospace	GS-11D	Geophone	65.12553616	-147.4761061
42	Geospace	GS-11D	Geophone	65.12552943	-147.4761338
43	Geospace	GS-11D	Geophone	65.1255227	-147.4761615
44	Geospace	GS-11D	Geophone	65.12551598	-147.4761892
45	Geospace	GS-11D	Geophone	65.12550925	-147.4762169
46	Geospace	GS-11D	Geophone	65.12550252	-147.4762446
47	Geospace	GS-11D	Geophone	65.1254958	-147.4762723
48	Geospace	GS-11D	Geophone	65.12548907	-147.4763

Table 24: Geophone Locations for ReMi Survey II

Station ID	Manufacturer	Model	Type of Sensor	Latitude	Longitude
1	Geospace	GS-11D	Geophone	65.125795	-147.47504
2	Geospace	GS-11D	Geophone	65.125793	-147.475046
3	Geospace	GS-11D	Geophone	65.125792	-147.475052
4	Geospace	GS-11D	Geophone	65.12579	-147.475059
5	Geospace	GS-11D	Geophone	65.125789	-147.475065
6	Geospace	GS-11D	Geophone	65.125787	-147.475071
7	Geospace	GS-11D	Geophone	65.125786	-147.475077
8	Geospace	GS-11D	Geophone	65.125784	-147.475083
9	Geospace	GS-11D	Geophone	65.125783	-147.475089
10	Geospace	GS-11D	Geophone	65.125781	-147.475096
11	Geospace	GS-11D	Geophone	65.12578	-147.475102
12	Geospace	GS-11D	Geophone	65.125778	-147.475108
13	Geospace	GS-11D	Geophone	65.125777	-147.475114
14	Geospace	GS-11D	Geophone	65.125775	-147.47512
15	Geospace	GS-11D	Geophone	65.125774	-147.475126
16	Geospace	GS-11D	Geophone	65.125772	-147.475133
17	Geospace	GS-11D	Geophone	65.125771	-147.475139
18	Geospace	GS-11D	Geophone	65.12577	-147.475145
19	Geospace	GS-11D	Geophone	65.125768	-147.475151
20	Geospace	GS-11D	Geophone	65.125767	-147.475157
21	Geospace	GS-11D	Geophone	65.125765	-147.475163
22	Geospace	GS-11D	Geophone	65.125764	-147.47517
23	Geospace	GS-11D	Geophone	65.125762	-147.475176
24	Geospace	GS-11D	Geophone	65.125761	-147.475182
25	Geospace	GS-11D	Geophone	65.125759	-147.475188
26	Geospace	GS-11D	Geophone	65.125758	-147.475194
27	Geospace	GS-11D	Geophone	65.125756	-147.4752

28	Geospace	GS-11D	Geophone	65.125755	-147.475207
29	Geospace	GS-11D	Geophone	65.125753	-147.475213
30	Geospace	GS-11D	Geophone	65.125752	-147.475219
31	Geospace	GS-11D	Geophone	65.12575	-147.475225
32	Geospace	GS-11D	Geophone	65.125749	-147.475231
33	Geospace	GS-11D	Geophone	65.125747	-147.475237
34	Geospace	GS-11D	Geophone	65.125746	-147.475244
35	Geospace	GS-11D	Geophone	65.125744	-147.47525
36	Geospace	GS-11D	Geophone	65.125743	-147.475256
37	Geospace	GS-11D	Geophone	65.125741	-147.475262
38	Geospace	GS-11D	Geophone	65.12574	-147.475268
39	Geospace	GS-11D	Geophone	65.125739	-147.475274
40	Geospace	GS-11D	Geophone	65.125737	-147.475281
41	Geospace	GS-11D	Geophone	65.125736	-147.475287
42	Geospace	GS-11D	Geophone	65.125734	-147.475293
43	Geospace	GS-11D	Geophone	65.125733	-147.475299
44	Geospace	GS-11D	Geophone	65.125731	-147.475305
45	Geospace	GS-11D	Geophone	65.12573	-147.475311
46	Geospace	GS-11D	Geophone	65.125728	-147.475318
47	Geospace	GS-11D	Geophone	65.125727	-147.475324
48	Geospace	GS-11D	Geophone	65.125725	-147.47533

Table 25: Geophone Locations for ReMi PIC-2 Survey

Station ID	Manufacturer	Model	Type of Sensor	Latitude	Longitude
1	Geospace	GS-11D	Geophone	65.11735288	-147.4336058
2	Geospace	GS-11D	Geophone	65.11735288	-147.4336128
3	Geospace	GS-11D	Geophone	65.11735288	-147.4336198
4	Geospace	GS-11D	Geophone	65.11735288	-147.4336268
5	Geospace	GS-11D	Geophone	65.11735288	-147.4336339
6	Geospace	GS-11D	Geophone	65.11735288	-147.4336409
7	Geospace	GS-11D	Geophone	65.11735288	-147.4336479
8	Geospace	GS-11D	Geophone	65.11735288	-147.4336549
9	Geospace	GS-11D	Geophone	65.11735288	-147.433662
10	Geospace	GS-11D	Geophone	65.11735288	-147.433669
11	Geospace	GS-11D	Geophone	65.11735288	-147.433676
12	Geospace	GS-11D	Geophone	65.11735288	-147.4336831
13	Geospace	GS-11D	Geophone	65.11735288	-147.4336901
14	Geospace	GS-11D	Geophone	65.11735288	-147.4336971
15	Geospace	GS-11D	Geophone	65.11735288	-147.4337041
16	Geospace	GS-11D	Geophone	65.11735288	-147.4337112
17	Geospace	GS-11D	Geophone	65.11735288	-147.4337182

18	Geospace	GS-11D	Geophone	65.11735288	-147.4337252
19	Geospace	GS-11D	Geophone	65.11735288	-147.4337322
20	Geospace	GS-11D	Geophone	65.11735288	-147.4337393
21	Geospace	GS-11D	Geophone	65.11735288	-147.4337463
22	Geospace	GS-11D	Geophone	65.11735288	-147.4337533
23	Geospace	GS-11D	Geophone	65.11735288	-147.4337603
24	Geospace	GS-11D	Geophone	65.11735288	-147.4337674
25	Geospace	GS-11D	Geophone	65.11735288	-147.4337744
26	Geospace	GS-11D	Geophone	65.11735288	-147.4337814
27	Geospace	GS-11D	Geophone	65.11735288	-147.4337884
28	Geospace	GS-11D	Geophone	65.11735288	-147.4337955
29	Geospace	GS-11D	Geophone	65.11735288	-147.4338025
30	Geospace	GS-11D	Geophone	65.11735288	-147.4338095
31	Geospace	GS-11D	Geophone	65.11735288	-147.4338165
32	Geospace	GS-11D	Geophone	65.11735288	-147.4338236
33	Geospace	GS-11D	Geophone	65.11735288	-147.4338306
34	Geospace	GS-11D	Geophone	65.11735288	-147.4338376
35	Geospace	GS-11D	Geophone	65.11735288	-147.4338446
36	Geospace	GS-11D	Geophone	65.11735288	-147.4338517
37	Geospace	GS-11D	Geophone	65.11735288	-147.4338587
38	Geospace	GS-11D	Geophone	65.11735288	-147.4338657
39	Geospace	GS-11D	Geophone	65.11735288	-147.4338728
40	Geospace	GS-11D	Geophone	65.11735288	-147.4338798
41	Geospace	GS-11D	Geophone	65.11735288	-147.4338868
42	Geospace	GS-11D	Geophone	65.11735288	-147.4338938
43	Geospace	GS-11D	Geophone	65.11735288	-147.4339009
44	Geospace	GS-11D	Geophone	65.11735288	-147.4339079
45	Geospace	GS-11D	Geophone	65.11735288	-147.4339149
46	Geospace	GS-11D	Geophone	65.11735288	-147.4339219
47	Geospace	GS-11D	Geophone	65.11735288	-147.433929
48	Geospace	GS-11D	Geophone	65.11735288	-147.433936

APPENDIX C: WAVEFORMS ACQUIRED AT POKER FLAT

CS Records and Wave Arrival Picks

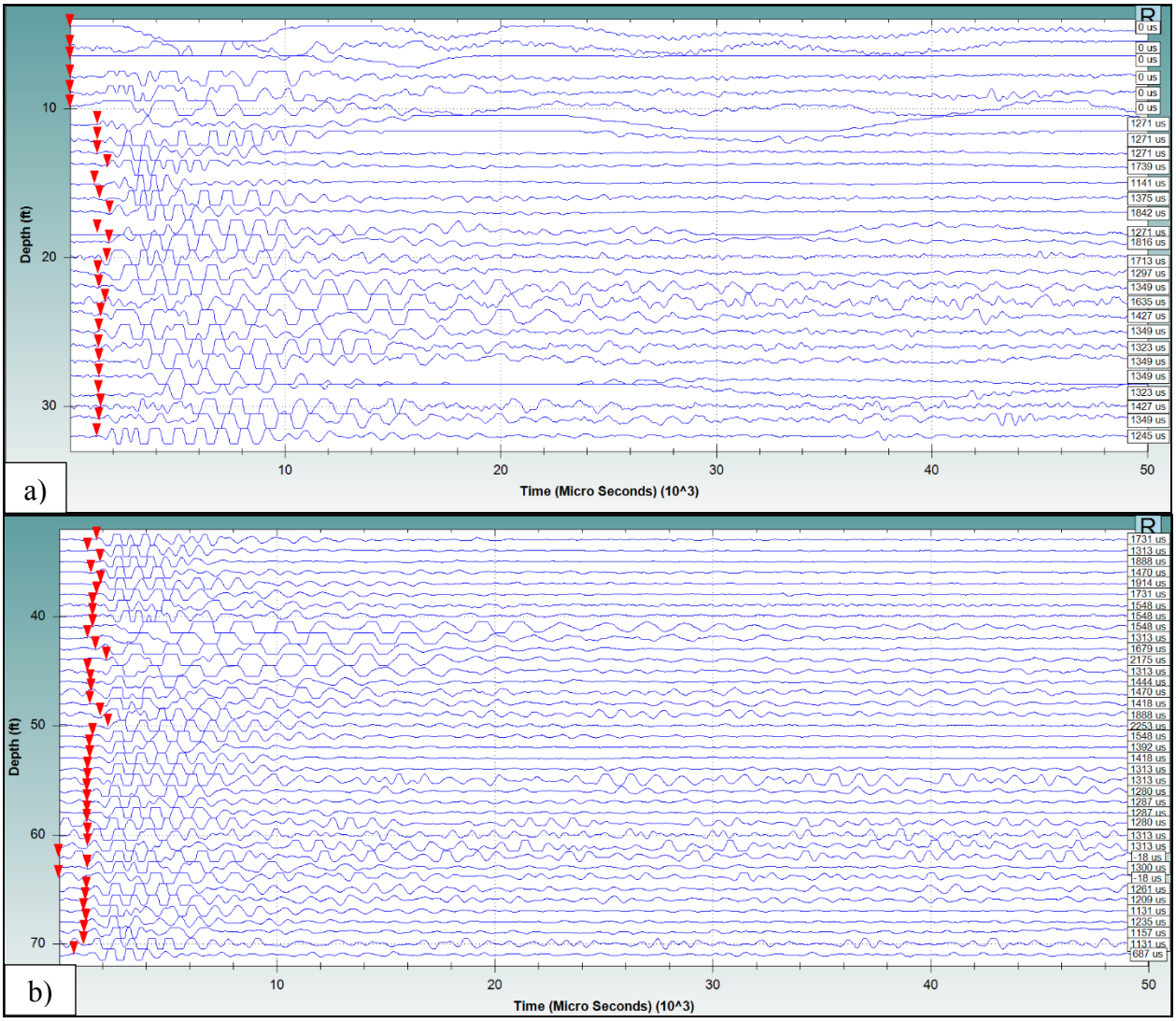

Figure C1: Radial component CS data from this investigation at depths of a) 5 to 32 feet (1.52 to 9.75 meters); and, b) 33 to 71 feet (10.06 to 21.64 meters) below TOC. All traces (blue) are in response to compressional (horizontal) impacts. Red upside-down triangles denote picked S-wave arrival times; the exact times are listed on the right, in microseconds (us).

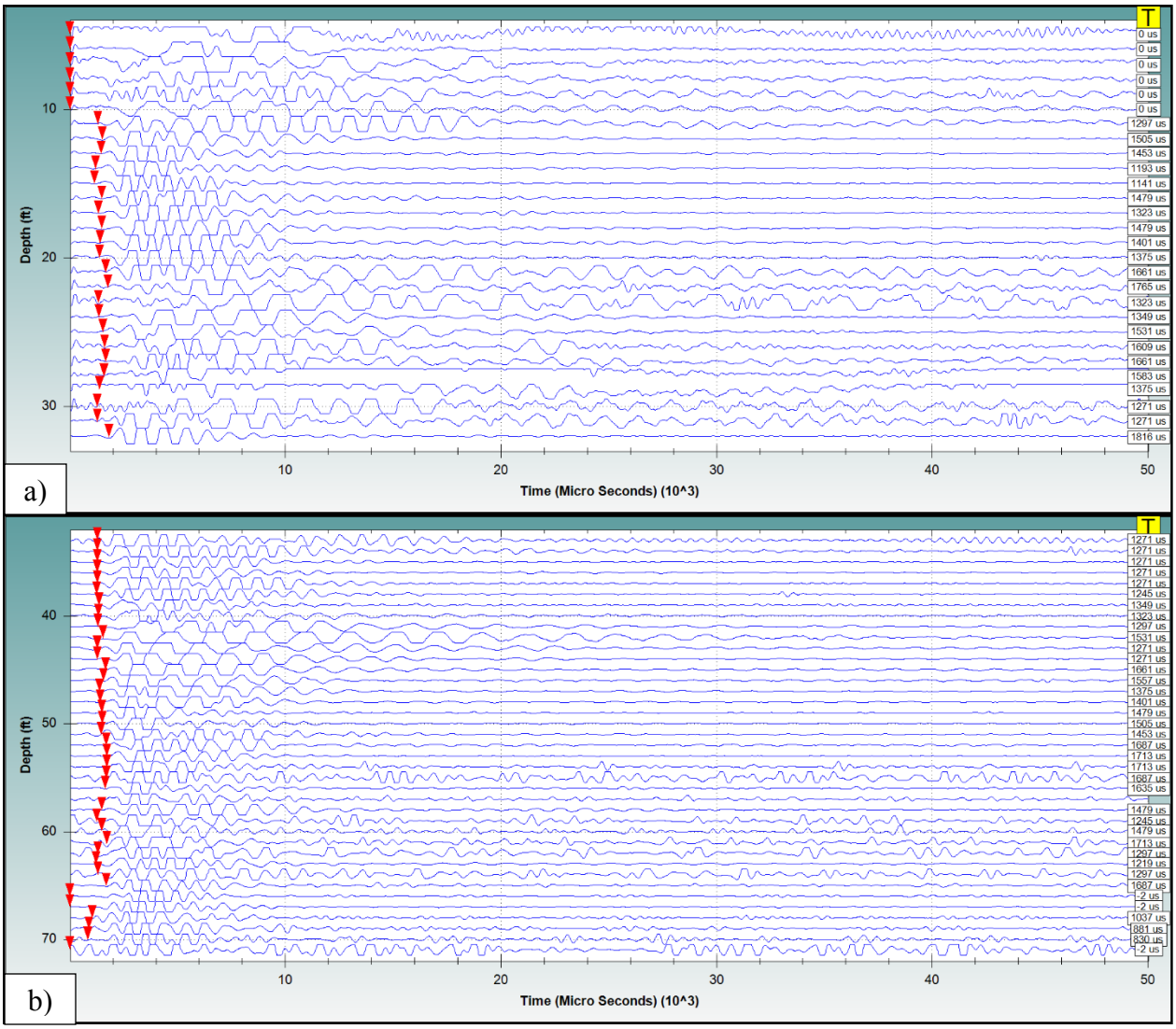

Figure C2: Transverse component CS data from this investigation at depths of a) 5 to 32 feet (1.52 to 9.75 meters) and b) 33 to 71 feet (10.06 to 21.64 meters) below TOC. All traces (blue) are in response to compressional (horizontal) impacts. Red upside-down triangles denote picked S-wave arrival times; the exact times are listed on the right, in microseconds (us).

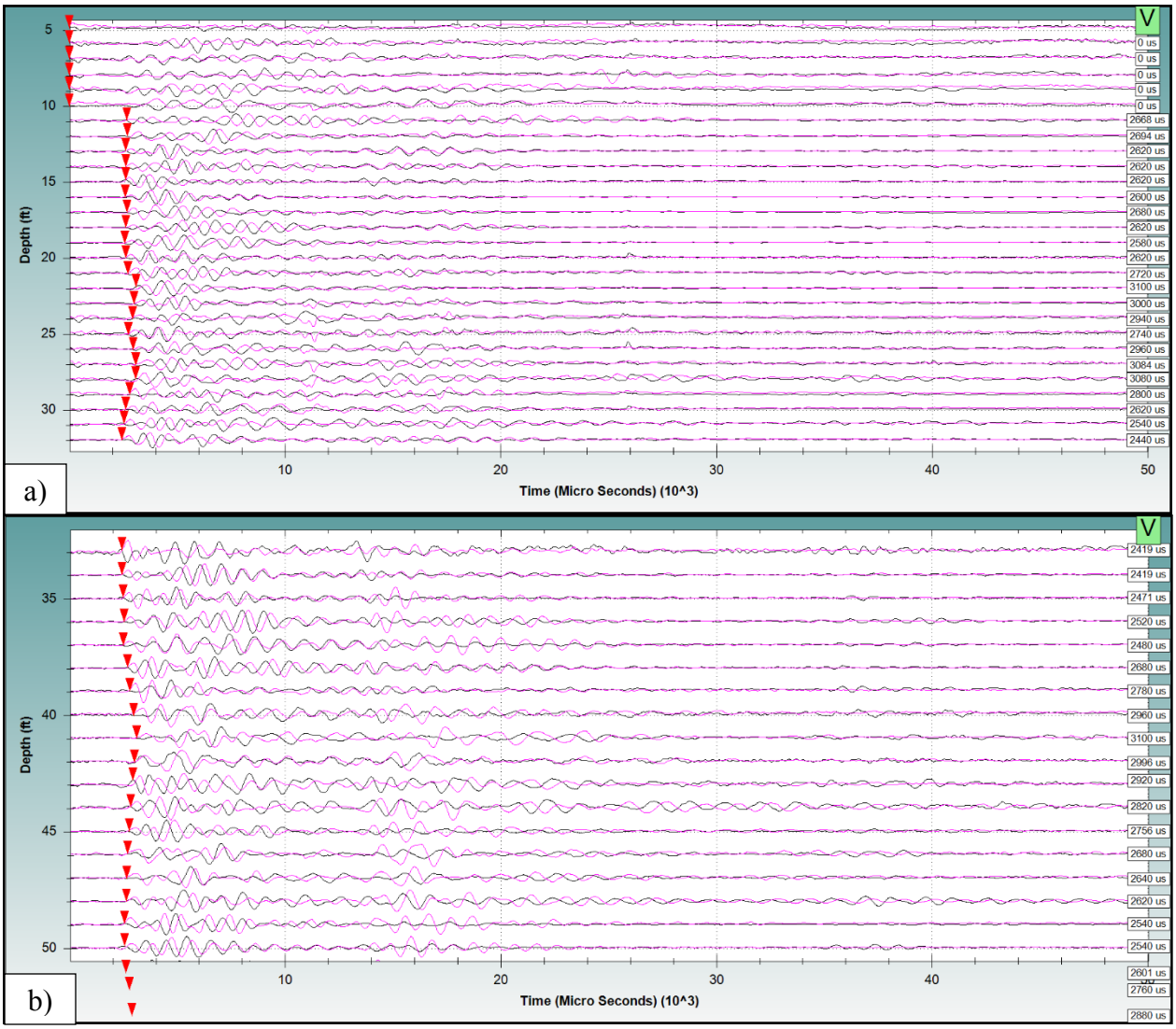

Figure C3: Vertical component CS data from this investigation at depths of a) 5 to 32 feet (1.52 to 9.75 meters) and b) 33 to 50 feet (10.06 to 15.24 meters) below TOC. Pink/black traces indicate shear impacts in opposite directions (up/down impacts, respectively). Red upside-down triangles denote picked S-wave arrival times; the exact times are listed on the right, in microseconds (us).

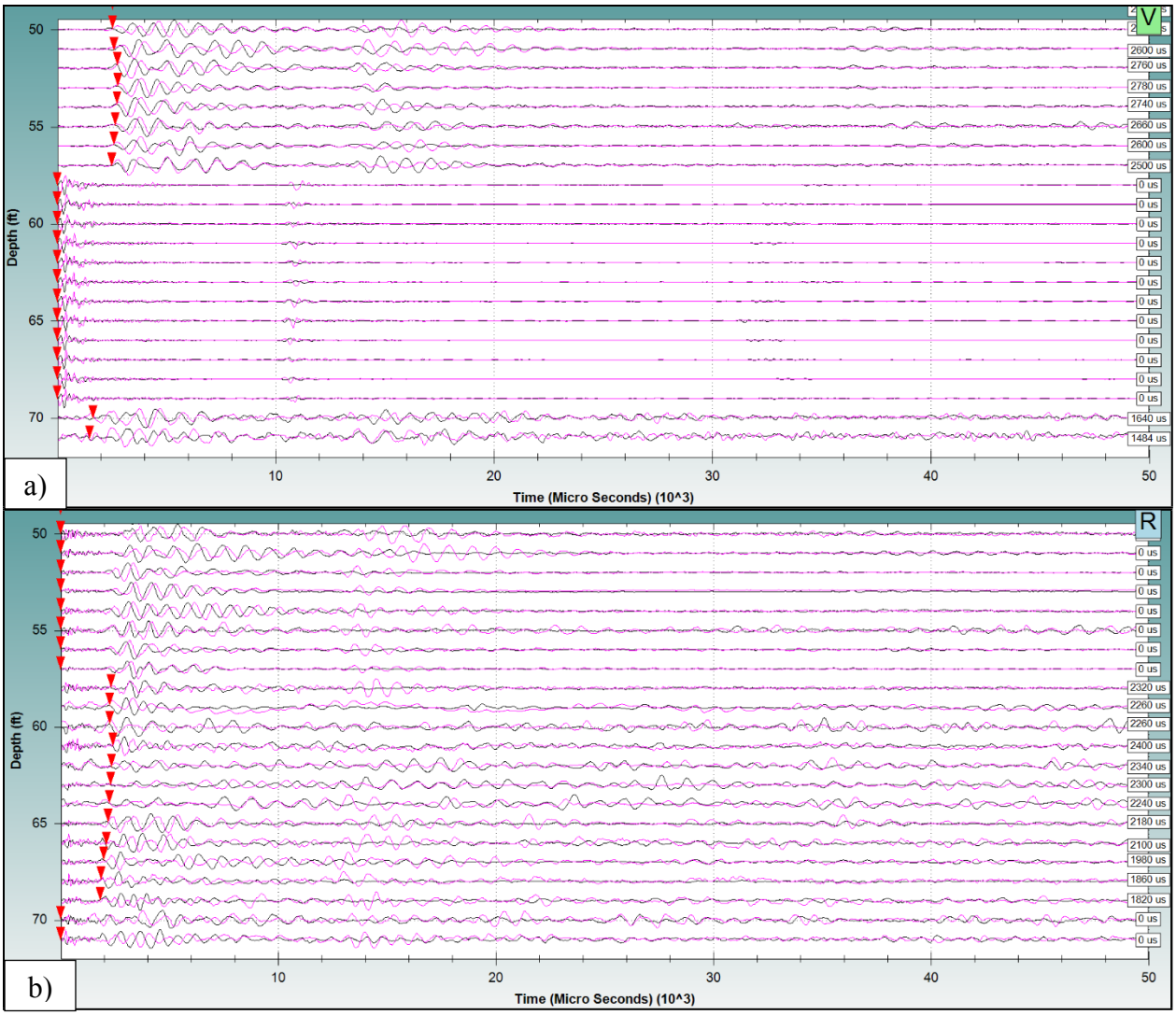

Figure C4: a) Vertical component, and b) radial component, CS data from this investigation at depths of 50 to 71 feet (15.24 to 21.64 meters) below TOC. Pink/black traces indicate shear impacts in opposite directions (up/down impacts, respectively). Red upside-down triangles denote picked S-wave arrival times; the exact times are listed on the right, in microseconds (us). There are no vertical component picks from 58 to 69 feet below TOC due to source/receiver cross-coupling. The picks for these depths were made on the radial component.

APPENDIX D: BOREHOLE DEVIATION PLOTS

Appendix D – Borehole Deviation Surveys

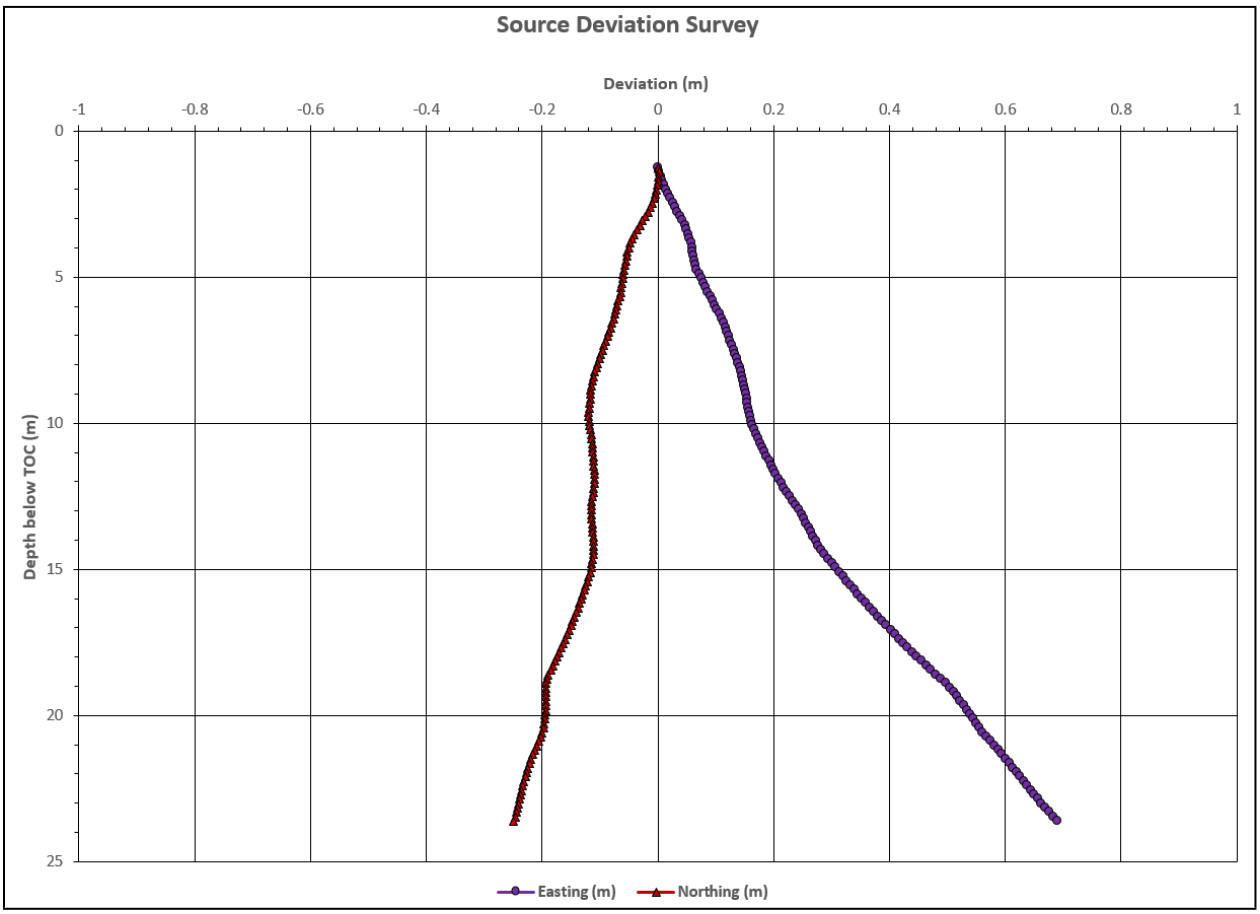

Figure D1: Deviation survey results from the source borehole. Note that deviations are shown with respect to magnetic, not geographic, north.

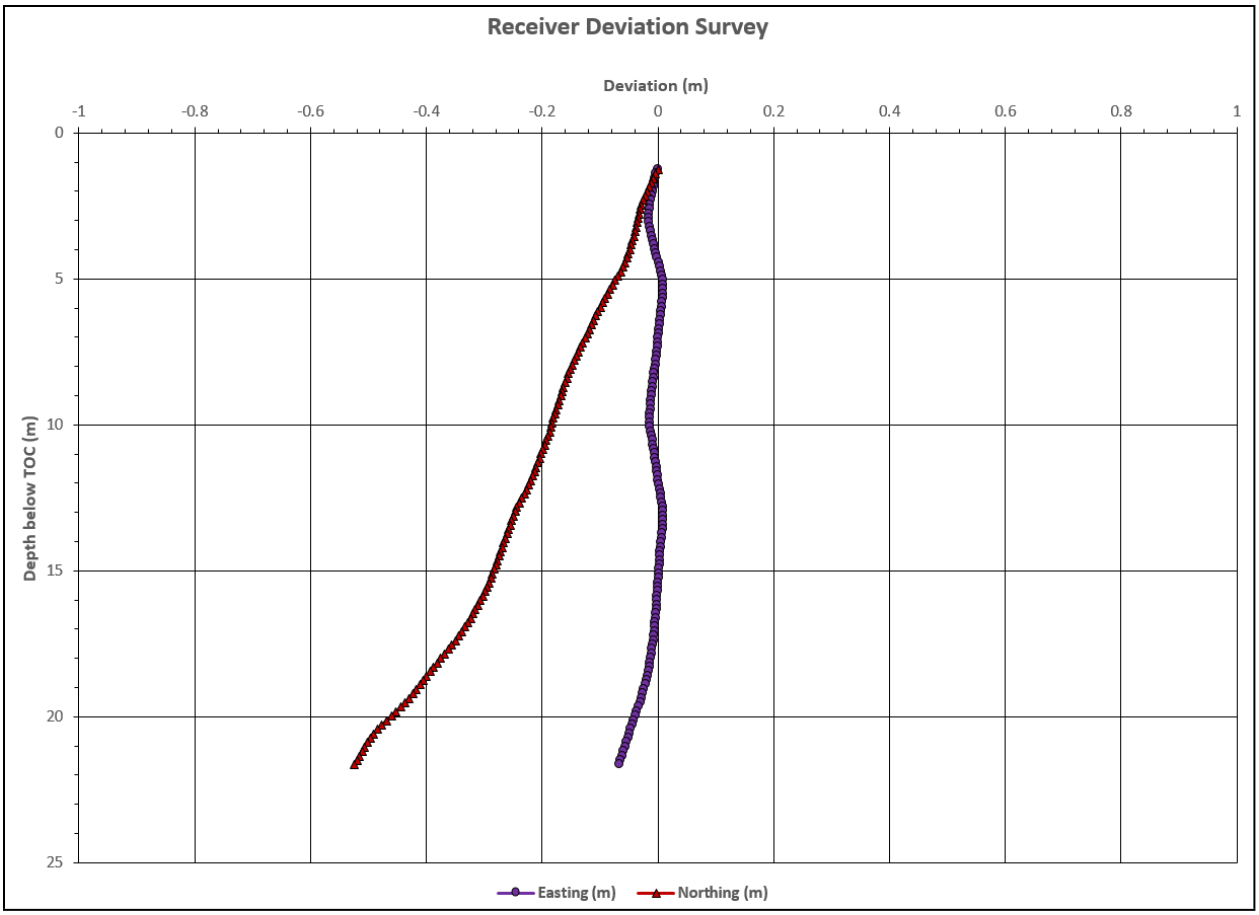

Figure D2: Deviation survey results from the receiver borehole. Note that deviations are shown with respect to magnetic, not geographic, north.

APPENDIX E: SEISMIC VELOCITY & ELASTIC MODULUS TABLE

Table E1: CS velocity and elastic moduli results. Red velocity values indicate low confidence.

Depth below TOC (m)	P-Wave Velocity (m/s)	S-Wave Velocity (m/s)	Poisson's Ratio	Soil/Rock Unit Weight (kg/m^3)	Constrained Modulus M (GPa)	Shear Modulus G (GPa)	Young's Modulus E (GPa)
3.35	3050	1453	0.35	7.5	69.7	15.8	42.8
3.66	3053	1440	0.36	7.5	70.0	15.6	42.3
3.96	3053	1481	0.35	7.5	70.1	16.5	44.4
4.27	3252	1481	0.37	7.5	79.7	16.5	45.3
4.57	3401	1481	0.38	7.6	87.4	16.6	45.8
4.88	2817	1490	0.31	7.6	60.1	16.8	43.9
5.18	2921	1442	0.34	7.6	64.7	15.8	42.2
5.49	3034	1472	0.35	7.6	69.9	16.5	44.3
5.79	2743	1490	0.29	7.6	57.3	16.9	43.6
6.10	2789	1464	0.31	7.6	59.3	16.3	42.8
6.40	2949	1406	0.35	7.6	66.5	15.1	40.9
6.71	2829	1231	0.38	7.7	61.3	11.6	32.1
7.01	2880	1270	0.38	7.7	63.7	12.4	34.2
7.32	2820	1294	0.37	7.7	61.2	12.9	35.2
7.62	2813	1385	0.34	7.7	61.0	14.8	39.6
7.92	2864	1280	0.38	7.7	63.4	12.7	34.8
8.23	2804	1227	0.38	7.7	60.9	11.6	32.2
8.53	2799	1226	0.38	7.8	60.8	11.7	32.2
8.84	2850	1347	0.36	7.8	63.1	14.1	38.2
9.14	2964	1438	0.35	7.8	68.4	16.1	43.4
9.45	2959	1481	0.33	7.8	68.3	17.1	45.6
9.75	3016	1539	0.32	7.8	71.1	18.5	49.0
10.06	2950	1550	0.31	7.8	68.2	18.8	49.3
10.36	2945	1547	0.31	7.9	68.1	18.8	49.2
10.67	2938	1511	0.32	7.9	67.9	18.0	47.4
10.97	2930	1478	0.33	7.9	67.7	17.2	45.8
11.28	2923	1498	0.32	7.9	67.5	17.7	46.9
11.58	2977	1383	0.36	7.9	70.1	15.1	41.2
11.89	2741	1330	0.35	7.9	59.6	14.0	37.8
12.19	2788	1246	0.38	7.9	61.7	12.3	33.9
12.50	2836	1187	0.39	8.0	64.0	11.2	31.3
12.80	2795	1225	0.38	8.0	62.3	12.0	33.1
13.11	2878	1253	0.38	8.0	66.2	12.5	34.7
13.41	2871	1294	0.37	8.0	66.0	13.4	36.8
13.72	2769	1319	0.35	8.0	61.5	14.0	37.8
14.02	2510	1352	0.30	8.0	50.6	14.7	38.1
14.33	2627	1368	0.31	8.1	55.6	15.1	39.6
14.63	2569	1374	0.30	8.1	53.3	15.2	39.6
14.94	2426	1412	0.24	8.1	47.6	16.1	40.1
15.24	2374	1406	0.23	8.1	45.6	16.0	39.4

Table E1 (continued): CS velocity and elastic moduli results.

Depth below TOC (m)	P-Wave Velocity (m/s)	S-Wave Velocity (m/s)	Poisson's Ratio	Soil/Rock Unit Weight (kg/m^3)	Constrained Modulus M (GPa)	Shear Modulus G (GPa)	Young's Modulus E (GPa)
15.54	2452	1370	0.27	8.1	48.8	15.2	38.8
15.85	2551	1287	0.33	8.1	52.9	13.5	35.8
16.15	2493	1272	0.32	8.1	50.7	13.2	34.9
16.46	2684	1286	0.35	8.2	58.8	13.5	36.5
16.76	2672	1319	0.34	8.2	58.4	14.2	38.1
17.07	2729	1343	0.34	8.2	61.0	14.8	39.6
17.37	2702	1391	0.32	8.2	59.9	15.9	41.9
17.68	2688	1491	0.28	8.2	59.4	18.3	46.7
17.98	2688	1523	0.26	8.2	59.6	19.1	48.3
18.29	2607	1515	0.25	8.3	56.1	18.9	47.2
18.59	2593	1419	0.29	8.3	55.6	16.6	42.8
18.90	2609	1446	0.28	8.3	56.4	17.3	44.3
19.20	2592	1462	0.27	8.3	55.8	17.7	44.9
19.51	2576	1491	0.25	8.3	55.2	18.5	46.2
19.81	2632	1523	0.25	8.3	57.7	19.3	48.2
20.12	2728	1570	0.25	8.3	62.1	20.6	51.6
20.42	2897	1655	0.26	8.4	70.2	22.9	57.6
20.73	3142	1752	0.27	8.4	82.7	25.7	65.6
21.03	3678	1780	0.35	8.4	113.6	26.6	71.7
21.34	3885	1966	0.33	8.4	127.0	32.5	86.4
21.64	4672	2163	0.36	8.4	183.9	39.4	107.5

APPENDIX F: GEOPSY PARAMETERS

SIGNAL FILE NAME = CE1.PA.00.HHZ.2013.311
WINDOW MIN LENGTH (s) = 25
WINDOW MAX LENGTH (s) = 50
WINDOW LENGTH TYPE (at least/exactly/freq. dep.) = exactly
DO BAD SAMPLE TOLERANCE (y/n) = n
BAD SAMPLE TOLERANCE (s) = 0
DO WINDOW OVERLAP (y/n) = n
WINDOW OVERLAP (%) = 5
DO BAD SAMPLE THRESHOLD (y/n) = n
BAD SAMPLE THRESHOLD (%) = 99
ANTI-TRIGGERING ON RAW SIGNAL (y/n) = n
USED RAW COMPONENTS = y, y, y, n, y
RAW STA (s) = 1
RAW LTA (s) = 30
RAW MIN SLTA = 0.2
RAW MAX SLTA = 2.5
ANTI-TRIGGERING ON FILTERED SIGNAL (y/n) = y
FILTER TYPE (low pass/high pass/band pass/band reject) = high pass
FILTER METHOD (butterworth/taper) = taper
FILTER MIN FREQUENCY (Hz) = 1
FILTER MAX FREQUENCY (Hz) = 10
FILTER CAUSAL (y/n) = n
FILTER ORDER = 1
FILTER WIDTH = 0.1
USED FILTERED COMPONENTS = y, y, y, n, y
FILTERED STA (s) = 2
FILTERED LTA (s) = 40
FILTERED MIN SLTA = 0.7
FILTERED MAX SLTA = 2.5
SMOOTHING TYPE (konno & ohmachi/constant band/proportional/no smoothing) = konno & ohmachi
SMOOTHING CONSTANT = 40.00
DO COSINE TAPER = true
TAPER WIDTH = 5
DO HIGH PASS = false
HIGH PASS FREQUENCY = 1
MINIMUM FREQUENCY = 2
MAXIMUM FREQUENCY = 60
INVERSED FREQUENCY = n
SAMPLES NUMBER FREQUENCY = 200
SAMPLING TYPE FREQUENCY (0=log, 1=linear)= 0
HORIZONTAL COMPONENTS = Squared
HORIZONTAL AZIMUTH = 0

DISTRIBUTION

1	MS0899	Technical Library	9536 (electronic copy)
1	MS0359	D. Chavez, LDRD Office	1911


Sandia National Laboratories